Winter 12-11-2014

FERROELECTRIC POLARIZATION DEPENDENT INTERFACE EFFECTS

Xiaohui Liu

University of Nebraska-Lincoln, phyliuxiaohui@gmail.com

Follow this and additional works at: http://digitalcommons.unl.edu/physicsdiss

Part of the Condensed Matter Physics Commons

FERROELECTRIC POLARIZATION DEPENDENT INTERFACE EFFECTS

By

Xiaohui Liu

A DISSERTATION

Presented to the Faculty of

The Graduate College at University of Nebraska

In Partial Fulfillment of Requirements

For the Degree of Doctor of Philosophy

Major: Physics and Astronomy

Under the Supervision of Professor Evgeny Y. Tsymbal

Lincoln, Nebraska

December, 2014

FERROELECTRIC POLARIZATION DEPENDENT INTERFACE EFFECTS

Xiaohui Liu, PhD

University of Nebraska, 2014

Adviser: Evgeny Y. Tsymbal

Utilization of the switchable spontaneous polarization of nanometer scale ferroelectric materials offers a promising avenue for future nanoelectronic devices. In this dissertation, we use density-functional calculations and phenomenological modeling to explore the effects of interface termination on thin-film heterostructures, the effects of electron doping in bulk ferroelectric materials on ferroelectric stability, and the effects of ferroelectric polarization switching on the electronic and transport properties of interfaces.

For $SrRuO_3$/$BaTiO_3$/$SrRuO_3$ epitaxial heterostructures grown on $SrTiO_3$, we find that the built-in dipole at the BaO/RuO_2 terminated interface leads to a strong preference for one polarization. We predict that this unfavorable interface dipole effect can be alleviated by deposition of a thin layer of $SrTiO_3$ at the BaO/RuO_2 interface. Our theoretical prediction is confirmed by the results of experimental studies performed by our colleagues at University of Nebraska.

While ferroelectric materials are normally considered as insulators, ferroelectricity and conductivity can coexist in electron-doped $BaTiO_3$ (n-$BaTiO_3$). We demonstrate that ferroelectric displacements persist up to the critical concentration of 0.11 electron per unit-cell volume consistent with experiment. Our investigations show that the ferroelectric instability requires only a short-range portion of the Coulomb force

with an interaction range of the order of the lattice constant, thus providing a new insight into the origin of ferroelectricity in displacive ferroelectrics.

The effects of ferroelectric polarization on the electronic and transport properties are explored for the $SrRuO_3/n\text{-}BaTiO_3(001)$ heterojunction. Ferroelectric polarization controls the accumulation or depletion of electron charge at the interface and thus determines the electron and spin transport regime. First, we find that the interface exhibits a Schottky tunnel barrier for one polarization orientation, whereas an Ohmic contact is present for the opposite polarization orientation. This leads to a five orders of magnitude change in the interface resistance with polarization reversal. Second, by taking into account the fact that $SrRuO_3$ is a ferromagnetic metal below 160 K, we find that the interface transmission is negatively spin-polarized. In the high doping regime, we predict that the ferroelectric polarization reversal alters the transport spin-polarization from -65% to -98%, whereas in the low doping regime, the spin-polarization of transmission across the $SrRuO_3/n\text{-}BaTiO_3(001)$ interface changes sign.

Acknowledgements

My first and foremost gratitude goes to my supervisor, Prof. Evgeny Tsymbal. It has been a great honor to work with him on my physics research. He has been guiding and supporting me on my pursuit of this doctoral degree with great patience, encouragement and knowledge. His rigorous and open thinking on physics influenced my understanding of this field and enhanced my problem-solving abilities when researching. My research experience in his group is invaluable.

This research group is like a family and I have got support from every member during my graduate program. Dr. J. D. Burton, a young brilliant physicist, is a second supervisor to me. He taught me the calculation code in my research and gave me instructive suggestion when I face problem. He provided me help for all my research. Dr. Yong Wang and Dr. Pavel Lukashev also gave me great help. They contributed great effort on calculations and data analysis on my first publication. The main parts of Chapter 3 are contributed by Dr. Yong Wang and I just contribute some calculations on this work. I thank him for including this work in this dissertation. I would like to thank Professor Sitaram Jaswal for his help on improving my writing skills. I thank Dr. Tula Paudel for his help on technique of calculation. I thank former group member Dr. Yang Sun for his kind help when I came here five years ago. I thank Dr. Xiaoqian Dang. We worked in the same office room and have helpful talk on questions about physics.

I would like to thank Prof. Mikhail Zhuravlev. The collaborating work with him helps me a lot to improve my understanding on the work in Chapter 5.

Contents

List of Figures

Chapter 1 *Introduction*

1.1   Ferroelectric materials

Ferroelectrics represent a large sub group of dielectric materials, which have two major

characteristics. The first one is the existence of spontaneous electric polarization. The

second one is the response of polarization to electric field: polarization must be reversible

when a sufficiently large electric field is applied in the opposite direction. The research

on ferroelectrics normally deals with the mechanism of the formation of spontaneous

polarization, the relationship of polarization to the atomic and electronic structure, the

control of ferroelectric polarization, and the use of ferroelectric materials in electronic

devices.
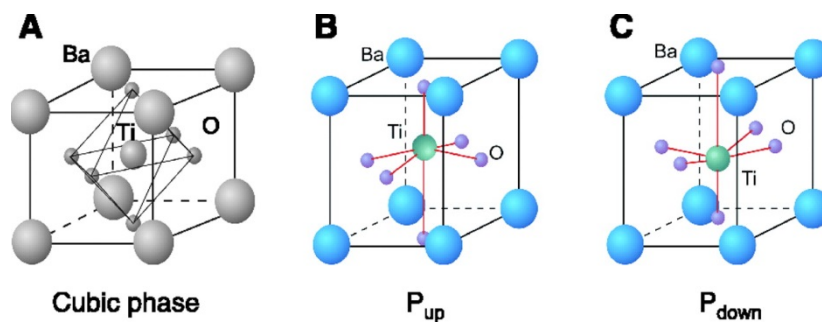
Figure 1.1 Crystal structure of the perovskite ferroelectric $BaTiO_3$. (A) High temperature,

paraelectric, cubic phase. (B and C) Room temperature, ferroelectric, tetragonal phases,

showing up and down polarization variants. From ref. [1]

The history of ferroelectrics goes back to the discovery of Rochelle salt in 1920s.

However, it was not until the 1940s when the discovery of ferroelectric $BaTiO_3$

stimulated studies on ferroelectricity as a phenomenon because of its simple atomic structure. In succession, theories of ferroelectricity have been established including the Landau's phenomenological theory and the soft-mode theory. Even today, $BaTiO_3$ is one of the most studied ferroelectric materials. $BaTiO_3$ belongs to the perovskite family and its ferroelectric response stems from the displacements of the cation atoms (Ti) with respect to the anion atoms (O) [1], as is shown in Figure 1.1. In this thesis, all the systems studied are based on the perovskite structure.
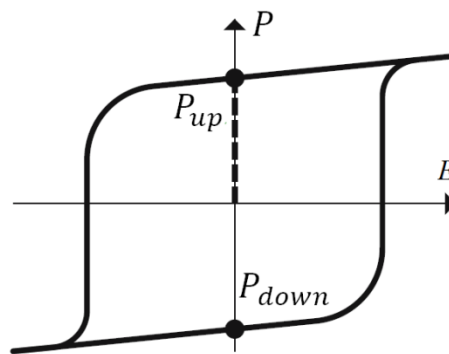
Figure 1.2 A typical ferroelectric hysteresis loop. The magnitude of the remanent polarization is shown (vertical dashed segment). From ref. [2]

In ferroelectric materials, the polarization directions can be switched by the external electric field due to the coupling of the electric field $\overline{E}$ and the polarization $\overline{P}$. This coupling reflects the change of relative energy $-\overline{E} \cdot \overline{P}$. The response of the polarization to the applied electric field produces a hysteresis loop which could be measured experimentally, as shown in Figure 1.2 [2]. Two values measured from

experiment $\vec{P}_{up}$ and $\vec{P}_{down}$ correspond to the two opposite remanent polarizations. Their values are given when the applied electric field is zero.

Perovskites are a large family of materials which exhibit a broad range of physical properties including ferroelectricity, ferromagnetism, magnetoelectric coupling, and superconductivity [3, 4, 5, 6]. The atomic structure of a perovskite can be represented by a chemical formula ABO_3. An ideal perovskite has a cubic unit cell shown in Fig. 1.1(a). By symmetry this cubic structure does not have a polarization and thus is not a ferroelectric. From the large family of perovskites, only few of them are ferroelectric [7]. As early as 1926, Goldschmidt recognized the relationship between the stability of the perovskite structure and the oxygen octahedra containing B atoms [8]. The size of A and B atoms determines the structure. In this empirical theory a tolerance factor t is defined by

$$t = (R_A + R_O)/\sqrt{2}(R_B + R_O),\qquad(1)$$

where R_A, R_B and R_O are radii of A, B and O atoms respectively. For $t > 1$, the structure prefers a ferroelectric state with a polar distortion of B atom (for example, $BaTiO_3$). For $t < 1$ rotation distortion suppresses ferroelectricity (for example, $SrTiO_3$ and $CaTiO_3$). Ferroelectricity is sensitive to strain due to its strong effect on the atomic structure. The in-plane strain influences the phase diagram of a ferroelectric thin film, and this effect is widely used nowadays for the growth of ferroelectric heterostructures with modified ferroelectric properties. Even in a paraelectric material, such as $SrTiO_3$, epitaxial strain may induce a ferroelectric phase [9].

Ferroelectric materials are also sensitive to temperature and strain. The former property is called pyroelectricity and the latter piezoelectricity. These properties have been used for long time. For example, pyroelectricity is used for infrared detection and piezoelectricity is used for sound detection, voltage source and as an actuator [10, 11].
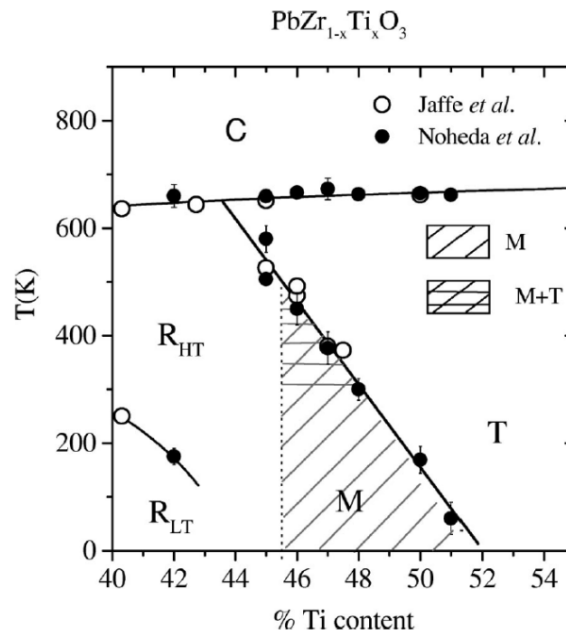
Figure 1.3 Phase diagram of PZT solid solution. From ref. [12]

In addition to the pure perovskites, perovskite oxide solid solutions have also been well studied. With isoelectronic substitutions, the phase diagram shows transition from one ferroelectric phase to another. A morphotropic phase boundary (MPB) is the transition region in the phase diagram. Figure 1.3 shows a phase diagram of PZT – a solid solution between PbZrO3 and PbTiO3 [12]. In the vicinity of MPB, an external applied electric

field can easily induce phase transition from one phase to another and lead to strong

piezoelectric effects. This kind of solid solution ferroelectric is used in actuators.

How to define an electric polarization? The traditional macroscopic view

(Clausius-Mossotti model) defines polarization as the electric dipole moment per unit

volume which is similar to the definition of ferromagnetic polarization. In this picture,

each electric dipole is isolated from each other. An electric dipole moment results from

the offset of the net electrical center of positive charge and negative charge within a unit

cell of the material. However, this picture is contrary to the real distribution of charge in

a real crystal, because it is hard or even impossible to identify an individual electric

dipole since the distribution of electron is delocalized in crystal. The electronic charges

are not localized but continually dispersed in the crystal lattice, which implies that

polarization of a crystal cannot be defined solely from the charge density distribution [13].

This is intuitively obvious if we realize that electron charge transfer happens not only

within a unit cell but among unit cells when polarization changes under external forces.

The modern understanding of electric polarization does not take polarization as an

absolute intensive quantity. The observable polarization is defined by the accumulated

adiabatic flow of current in the crystal. This theory is known as Berry-phase theory,

where the polarization is expressed in the form of a quantum phase known as a Berry

phase [14]. In this picture, the spontaneous polarization is not the absolute value but a

difference of two different ferroelectric states. During phase transition from paraelectric

phase to ferroelectric, the spontaneous polarization is the change of polarization during

this process.

1.2   Ferroelectric phase transition

The lack of inversion symmetry is required for a system to be ferroelectric. The soft

mode theory based on the theory lattice vibrations, may help predict the ferroelectric

phase transition. For example, the softening of the transverse optical phonon shown in

Figure 1.4 is a good predictor of ferroelectric phase transition. The mechanism behind the

soft-mode theory is the temperature dependence of long-range and short-range forces on

ions. Below the critical temperature, the balance between long-range and short-range

forces is broken such that the frequency of transverse optical mode ω_{TO} goes to zero.

The softening of the transverse optical mode at the middle of Brillouion zone, with wave

length $\lambda = \infty$ results in ferroelectric order, while the softening of the transverse optical

mode at the edge of Brillouion zone, $\lambda = 2d$ results in antiferroelectric order.
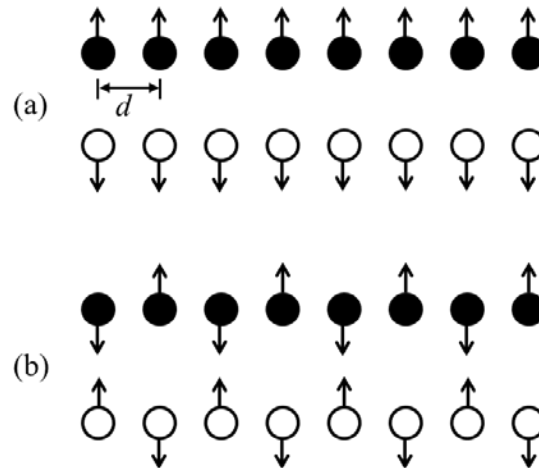
Figure 1.4 The transverse optical mode with $\lambda = \infty$ (a) and $\lambda = 2d$ (b). Here d is lattice

constant.

The macroscopic description of ferroelectric phase transition is Landau's

phenomenological theory based on symmetry considerations. Phase transitions from

higher symmetry phase to lower symmetry phases are characterized by the emerging of

the order parameters. The order parameter describing a paraelectric-ferroelectric phase

transition is ferroelectric polarization, which appears at low temperature. The free energy

can be expanded in a power series of the order parameter and only even-order terms are

retained by symmetry. A standard sixth-order free energy expansion is

$$f_P = \frac{1}{2}a_0(T-T_0)P^2 + \frac{1}{4}bP^4 + \frac{1}{6}cP^6 \ . \tag{2}$$

This equation is called the Landau-Devonshire equation. It is successfully used to

describe ferroelectric phase transition for example in $BaTiO_3$ and $PbTiO_3$ with

polarization restricted to an axis. To describe the monoclinic phase at MPB in the phase

diagram of PZT, eight-order expansion is necessary [15].

In a real system, due to the fluctuations of polarization or due to the existence of

boundary, polarization is not spatially uniform. The variations of the polarization

contribute to the free energy of a ferroelectric system. In this case, there is an additional

term in the free energy due to the variations of polarization proportional to $|\nabla P|^2$. This

equation is called the Landau-Ginzburg equation:

$$f_P = \frac{1}{2}a_0(T-T_0)P^2 + \frac{1}{4}bP^4 + \frac{1}{6}cP^6 + \gamma|\nabla P|^2 \tag{3}$$

The parameters in the Landau-Ginzburg equation are determined by experiments or

quantum mechanical calculations. The Landau theory plays important role in

understanding ferroelectricity and associated phenomena and can be extended to

ferroelectric thin films by taking into account the interface effects.

1.3   Nanoscale ferroelectric heterostructure
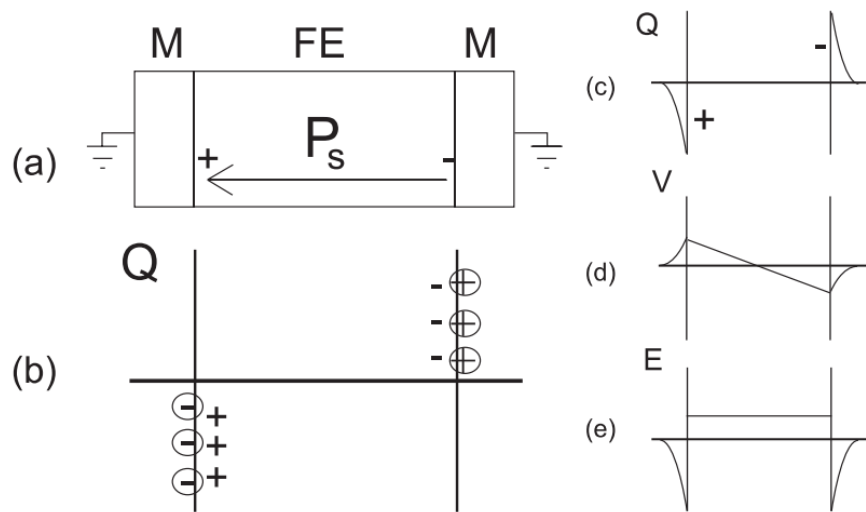
Figure 1.5 A schematic diagram of (a) a short-circuited electrode–ferroelectric structure

with the spontaneous polarization displayed; (b) its charge distribution in the presence of

perfect electrodes; its (c) charge distribution, (d) voltage and (e) field profiles in the

presence of realistic electrodes. Q is the charge near the interface which has a distribution

near the interface. Please note that here the film is taken to be a perfect insulator. From

ref. [16]

Since its discovery, ferroelectricity has been believed to exist just in bulk materials and

disappear when the dimensions of a ferroelectric material goes down to the nanoscale.

This is because the depolarizing field in ferroelectric increases as the dimension of the

materials is reduced. The depolarization effect on nanoscale ferroelectric can be understood from Figure 1.5 [16]. The depolarizing field is opposite to the direction of ferroelectric polarization in ferroelectric materials with boundaries. This depolarization effect is detrimental to ferroelectric polarization. With ferroelectric polarization being normal to the interface, the screening charges from the electrode compensate the ferroelectric polarization charge at each interface. For ideal metal, the polarization charges are perfectly compensated at both interfaces and therefore no depolarizing field emerges in the ferroelectric film. However, in real case, the effect of interface polarization charge is not fully compensated due to the incomplete screening by the electrode. The screening charges are distributed in a vicinity of the interface. The net charge distribution results in a voltage jump at each interface from the electrode. With both electrodes short-circuited, the voltage drop in the ferroelectric film from one interface to the other leads to the depolarizing field opposite to the polarization. This field depends inversely on the thickness of the ferroelectric film. Therefore, when the dimension of the ferroelectric film is down to a critical size, the depolarizing field will be strong enough to suppress the ferroelectricity.

With the development of experimental and theoretical techniques, the research on ferroelectric materials has increased significantly since 1990s. Experimentally, the techniques of growing complex oxide heterostructure have been well developed. The interface atomic structure can be well controlled to create sharp atomic interfaces. In theory, the development of first-principles methods has boosted the theoretical studies of ferroelectrics, especially ferroelectric nanostructures. Both experimental and theoretical

studies proved the existence of ferroelectricity at nanometer scale [17, 18, 19]. These studies opened the door to use ferroelectric thin films in nonvolatile electronic devices, including memory devices.

The properties of a ferroelectric thin film are determined by the whole system including the substrate and electrodes. The theoretical study of a ferroelectric $BaTiO_3$ thin film with $SrRuO_3$ electrodes revealed that ferroelectricity could be sustained down to six unit cells of $BaTiO_3$ (2.4 nanometers) [18]. Below this critical thickness, depolarization field due to the incomplete screening at the metal-ferroelectric interface suppresses ferroelectricity. Experimentally, ferroelectricity was found in perovskite $PbTiO_3$ thin layer of 1.2 nanometers (3 unit cells) at room temperature [19].

When the scale of system is reduced, the interfaces start to dominate the properties of the system. For nanoscale ferroelectrics, the atomic behaviors near the interface are quite different from the bulk, and this difference leads to rearrangement of atomic and electronic structures near the interface which leads to a crucial effect on ferroelectricity. Theoretical investigations have shown that, besides electron screening from electrode, ionic displacements in the metal electrode near the metal/ferroelectric interface have essential impact on the stabilization of ferroelectricity in ultra-thin $BaTiO_3$ [20, 21]. With soft lattice electrodes, the polarization continues into the metal and the bound polarization charges are then screened in the electrode. This screening mechanism results in the reduction of the critical thickness for ferroelectricity. In addition to screening, we will show in Chapter 2 that the different types of termination at the interface result in difference in the interface dipoles, affecting differently the ferroelectric

polarization. By engineering the interface, the detrimental interface termination could be eliminated and the ferroelectric stability could be enhanced.

Another aspect that is very important for ferroelectric stability at the nanoscale is the type of the substrate. The in-plane strain due to the misfit of the lattice constants between substrate and the ferroelectric results in the distortion of the lattice and therefore affect the ferroelectric stability of the system [22, 23].

If we analyze the mechanism of the formation of ferroelectric phase, in a $BaTiO_3$ as an example, three interactions control the ferroelectric displacements: (i) Ti-3d and O-2p orbitals hybridization, (ii) short-range repulsive force due to the electron cloud, and (iii) the long-range Coulomb interaction. The long-range Coulomb interaction plays a crucial role in the formation of soft mode and ferroelectric displacement in a perovskite ferroelectric. Our theoretical study, discussed in Chapter 3, found, however, that only the short-range part of the Coulomb interactions (with a length scale about 2 unit cells in $BaTiO_3$) determines the formation of ferroelectric phase. This implies that, for a $BaTiO_3$ thin layer, several unit cells thickness is enough to sustain the intrinsic balance between different interactions required for the formation and stability of ferroelectric displacement. We see therefore that the interface influences ferroelectric stability, and, on the other hand, the ferroelectric polarization affects the properties of the interface. This brings useful functionalities which may be employed in electronic devices. It has been shown that the switching of ferroelectric polarization in the thin-film heterostructures affects the electronic and/or atomic structures at the interface leading to interesting phenomena such

as the magnetoelectric coupling at ferroelectric/ferromagnetic interfaces [24, 25], the metal-insulator phase transitions [26, 27] and change of contact resistance [28].

1.4   Ferroelectric tunnel junction

One of the notable examples of the effect of ferroelectric polarization on functional properties is the tunneling electroresistance effect, which has been predicted and observed in ferroelectric tunnel junctions (FTJs) [29, 30].   A ferroelectric tunnel junction (FTJ) is a thin-film structure with an ultrathin ferroelectric layer sandwiched between two metal electrodes. In such a system, the ferroelectric insulator acts as a tunnel barrier and, if a bias voltage is applied across the FTJ, charge carriers can be transferred between the electrodes due to the phenomenon of quantum-mechanical tunneling.

The reversal of ferroelectric polarization in the barrier leads to a significant change in the tunneling resistance. The orientations of polarization in the barrier correspond to two states with high conductance G_R and low conductance G_L. A FTJ is characterized by tunneling electroresistance (TER), which is defined as

$$TER = \frac{(G_R - G_L)}{(G_R + G_L)}. \tag{4}$$

The studies on FTJs are focused on the mechanisms of the TER effect and how to enhance it.

Early experimental works found that the critical field to switch resistance is in line with the coercive field of ferroelectric thin films. This result proves that the origin of the switching of resistance is due to the ferroelectric polarization reversal in the
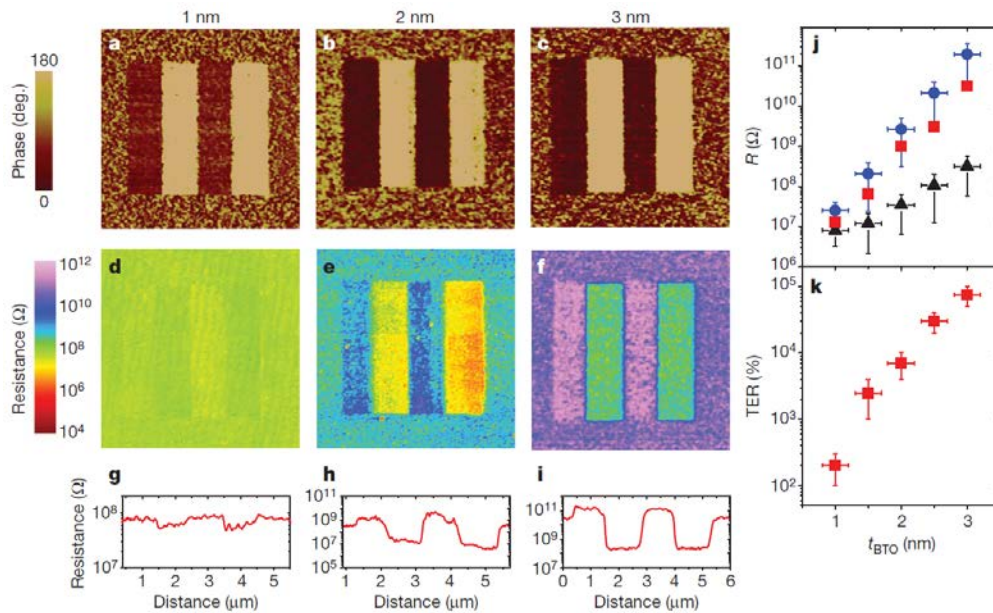
Figure 1.6 The giant tunneling electroresistance (TER) effect in ultrathin strained BaTiO$_3$ films. Piezoresponse force microscopy (PFM) phase image (a–c) and conducting atomic force microscopy resistance mapping (d–f) of four written ferroelectric stripes (1 × 4 μm 2) for BaTiO$_3$ films with a thickness of 1, 2, and 3 nm. (g–i) Corresponding resistance profiles of the poled area. (j) Thickness dependence of resistance (R) of unpoled (red squares), and positively (black triangles) and negatively (blue circles) poled regions. An exponential increase in R and TER (k) with BaTiO$_3$ thickness is seen, as expected for direct tunneling. From ref. [32]

ferroelectric barrier [31]. Experimentally, however, the I-V curve alone is not sufficient for the identification of the underlying resistive switching mechanism. Clear evidence of the link between ferroelectricity and transport was reported recently [32, 33]. Figure 1.6 shows the correlation between the ferroelectric polarization orientation and the transport

properties in $BaTiO_3$ films of different thickness. Figures 1.6(a-c) show the

piezoresponse force microscopy phase images and the corresponding tunneling

conductance across these films are shown in Figure 1.6(d-f) which are measured by

conducting atomic force microscopy (C-AFM). It is seen from Figure 1.6(j) that the

resistance grows exponentially with the film thickness, which is a clear evidence of a

tunneling transport regime in FTJ.

The electric potential height in the barrier due to incomplete screening of the

polarization charge could be modulated by the reversal of polarization, affecting the

tunneling resistance [34]. Since the resistance depends exponentially not only on

potential height but also on potential width, TER is expected to be greatly enhanced by

modulation of the potential width by ferroelectric polarization switching. Theory has

predicted such a mechanism in FTJs with two metal electrodes of different screening

lengths [34]. However, the TER in such a FTJ with metal electrodes is not big due to the

small screening length of the metal. Recently, a sizable (10^4) TER was found in a FTJ

($Pt/BaTiO_3/Nb:SrTiO_3$) with one electrode replaced by a Nb doped $SrTiO_3$

semiconductor [35]. This exciting result was qualitatively explained by the depletion of

the semiconductor surface due to the negative polarization charge when polarization is

pointing out of this interface.

Tsymbal and Kohlstedt summarize three mechanisms that affect the transport

properties due to the reversal of ferroelectric polarization in the tunneling barrier as

shown in Fig. 1.7. [29] (1) Due to incomplete screening of polarization charge at the

interface, depolarizing field is seen by the transport electrons across the barrier. The

reversal of ferroelectric polarization changes the potential profile and induces the change of transport properties. (2) The ionic displacements in electrodes near the interface affect the screening effect at the interface. The reversal of ferroelectric polarization influences the positions of ions near the interfaces. The chemical bonding between atoms is affected by the reversal of polarization and leads to the change of electronic transport. (3) All ferroelectrics have piezoelectric properties. The applied voltage produces strain on the ferroelectric barrier and therefore changes transport characteristics of the barrier, for example the width and the attenuation constant.
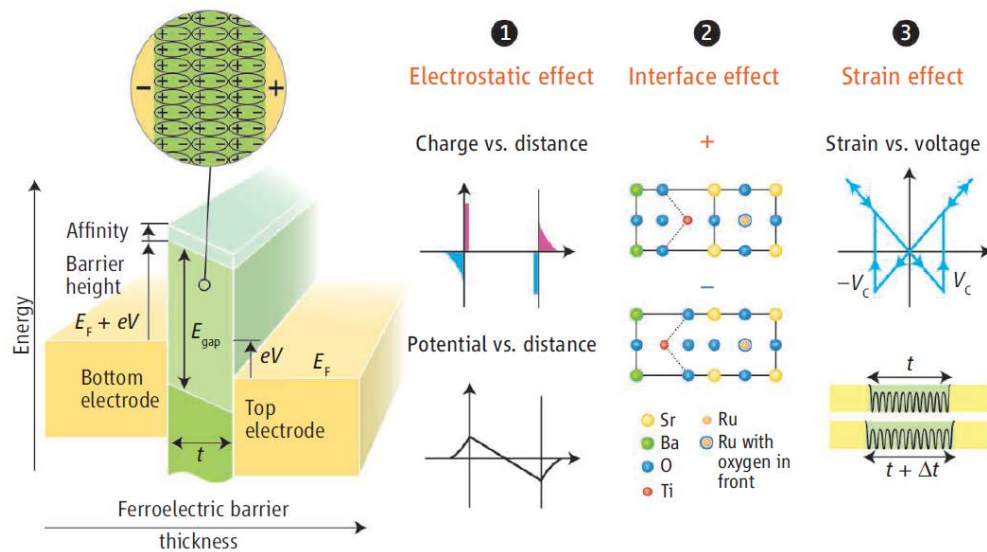
Figure 1.7 Schematic diagram of a ferroelectric tunnel junction, which consists of two electrodes separated by a nanometer-thick ferroelectric barrier layer. (E_{gap} is the energy gap. E_F is the Fermi energy, V is the applied voltage, V_c is the coercive voltage, t is the barrier thickness, and Δt is the thickness variation under an applied field. From ref. [29]

Moreover, the combination of ferroelectric and ferromagnetic nanostructures in FTJs may make the junction multiferroic. In such extended FTJs, spin-dependent tunneling is controlled by electric polarization and the functionalities of such FTJs could be enhanced [36, 37].

For practical applications it is important to increase the ON/OFF resistance ratio (the TER effect). Recently, experiment and theory found that with electron doping, $BaTiO_3$ could be made conducting [38]. These studies open the way to use a conducting ferroelectric in novel ferroelectric devices. Switching ferroelectric polarization in electron doped ferroelectrics results in a promising phenomenon. In Chapter 4, we present a study on a metal/n-ferroelectric heterojunction, where we predict that reversal of ferroelectric polarization leads to a change of the conductance regime at the interface from Ohmic to Schottky, leading to a huge resistance ratio of 10^5. In Chapter 5, we show ferroelectric controlled spin polarization across the interface ferroelectric/n-ferroelectric heterojunction.

Besides tunneling, another interesting and important ferroelectric polarization dependent transport phenomenon is the photovoltaic effect. Ferroelectrics are usually insulators. However, some narrow gap ferroelectrics, for example $BiFeO_3$ (BFO), show semiconducting behavior. Under visible light illumination, photovoltaic effect has been seen in BFO [39, 40, 41]. The direction of the photocurrent created in ferroelectric semiconductor depends on the direction of ferroelectric polarization.

Chapter 2 *Interface effect on ferroelectric stability of nanoscale ferroelectric films*

Utilization of the switchable spontaneous polarization of ferroelectric materials offers a promising avenue for the future of nanoelectronic memories and logic devices provided that nanoscale metal-ferroelectric-metal heterostructures can be engineered to maintain a bi-stable polarization switchable by an applied electric field. The most challenging aspect of this approach is to overcome the deleterious interface effects which tend to render ferroelectric polarization either unstable or unswitchable and which become ever more important as ferroelectric materials are produced thinner and thinner. In this chapter, we show results of our theoretical studies, which has been published in ref. [42]. We use first-principles density functional calculations and phenomenological modeling to demonstrate that the BaO/RuO_2 interface termination sequence in $SrRuO_3/BaTiO_3/SrRuO_3$ epitaxial heterostructures grown on $SrTiO_3$ can lead to a non-switchable polarization state for thin $BaTiO_3$ films due to a fixed interface dipole. The unfavorable interface dipole at the BaO/RuO_2 interface leads to a strong preference for one polarization state and, in thin-film structures, leads to instability of the other state below a certain critical thickness, thereby making the polarization unswitchable. We analyzed the contribution of this interface dipole to the energetic stability of these heterostructures. Furthermore, we propose and demonstrate that this unfavorable interface dipole effect can be alleviated by deposition of a thin layer of $SrTiO_3$ at the BaO/RuO_2 terminated interface. Our first-principles and phenomenological modeling predict that the associated change of the interface termination sequence to SrO/TiO_2 on

both sides of the heterostructure leads to a restoration of bi-stability with a smaller critical thickness, along with an enhancement of the barrier for polarization reversal. These results demonstrate that interface engineering is a viable approach to enhance ferroelectric properties at the nanoscale. Our theoretical predications have been confirmed by the experimental studies performed by our experimental collaborators which are published in ref. [43].

2.1 Ferroelectric stability of SrRuO$_3$/BaTiO$_3$/SrRuO$_3$ capacitor

We consider a ferroelectric capacitor with a thin ferroelectric layer inserted between two conducting electrodes. In such a thin film structure with perpendicular-to-the-plane ferroelectric polarization, three effects may influence ferroelectric stability: depolarization effect, built-in electric field and interface dipole. Addressing these detrimental effects is critical both for the fundamental understanding of the ferroelectric behavior at the nanoscale and related device performances.

As was discussed in Section 1.4, depolarizing field due to incomplete screening of the polarization charges accumulated on the two surfaces of the film is largely responsible for determining thin film ferroelectric stability. The depolarizing field can be reduced by formation of screening charges at the film electrode interfaces [18, 44, 45] and/or by the forming a non-uniform domain structure [19, 46, 47, 48, 49, 50, 51]. The depolarization effect is due to the intrinsic properties of electrode material because of the finite screening length of the electrode. It was found that high-quality ultrathin SrRuO$_3$/BaTiO$_3$/SrRuO$_3$ capacitors exhibit severe relaxation of BaTiO$_3$ polarization within a few microseconds [52]. This effect is a consequence of strong effective

depolarizing fields due to incomplete screening. The screening provided by conductive electrodes $SrRuO_3$ in metal-ferroelectric-metal structures appears to be insufficient, resulting in unstable ferroelectric polarization. These effects can smear out the ferroelectric phase transition and make ferroelectricity unstable at room temperature.

Theoretical studies found that degree of softness of the metal-oxide electrode lattice plays a crucial role in stabilizing the ferroelectric phase. For some electrodes, for example $SrRuO_3$, ferroelectric displacement in ferroelectric layer doesn't reduce sharply at the interface but penetrates into the metal electrode as is shown in Figure 2.1. In this case, the bound charges are screened within the electrodes due to the ionic screening effect. This effect provides an efficient mechanism to stabilize ferroelectricity of ferroelectric capacitor [20].
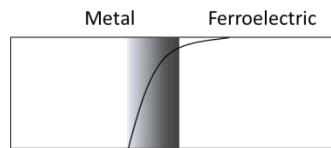
Figure 2.1 Penetration of the ionic polarization into the metal. The gradient in shading represents the concentration of free charge carriers, while the solid line represents the absolute value of polarization. From ref. [20]

Built-in electric field results from the different electronic and chemical environments of interfaces. The asymmetry could be due to different metal electrodes or different interface terminations. The strength of the built-in electric field E_{bi} in a capacitor is determined by the work functions of the two electrodes ϕ_1 , ϕ_2 and the thickness of the barrier L,

$$E_{bi} = \left(\phi_1 - \phi_2\right)/L. \tag{1}$$

Its direction is independent of polarization orientation and results in two non-equivalent

polarization states [53]. In fact such asymmetry may even destroy the stability of one of

the polarization states, making the system only monostable in zero applied field and

therefore nonferroelectric [54, 55].

Bonding of interface atoms at the interface becomes important when the

dimension of system is reduced. Recently, first-principles calculations have predicted that

interface atomic structure and chemical bonding at the interface may significantly impact

a thin film ferroelectric state [56]. The local chemical environment at the interfaces

affects the thin film ferroelectricity through the electrode-oxide bonds, which may

enhance or reduce ferroelectric displacements. If the interface bonding is sufficiently

strong and leads to the "freezing" of polar displacements in the interfacial region, a 'dead

layer' will be formed near the interface. The ferroelectric displacement at interface will

be pinned and affect the ferroelectric displacement of other atoms. Conversely, there is a

possibility that the interface performs a ferroelectric behavior due to the interface

bonding. In this case, the surface unit cell performs ferroelectrically. The dipole moments

at interface are switchable and the ferroelectric instability of the thin film is enhanced. In

particular, it was found that interfaces formed between AO-terminated perovskites and

simple metals may produce interfacial ferroelectricity, which enhances ferroelectricity of

the whole film [57]. These findings open an efficient way to stabilize and even enhance

ferroelectricity in nm-thick films through interface engineering.

2.2 Interface dipole effect on thin film ferroelectric stability

In this work, we exploit this approach to enhance ferroelectricity in thin $BaTiO_3$ films

sandwiched between two $SrRuO_3$ electrodes. Using first-principles calculations and

phenomenological modeling we demonstrate that introduction of a very thin layer of

$SrTiO_3$ at the $BaTiO_3$/$SrRuO_3$ interface eliminates an unfavorable built-in electrostatic

dipole at BaO/RuO_2 terminated interfaces, leading to a smaller critical thickness for a

stable and switchable ferroelectric polarization even at room temperature.

2.2.1 Structures and method
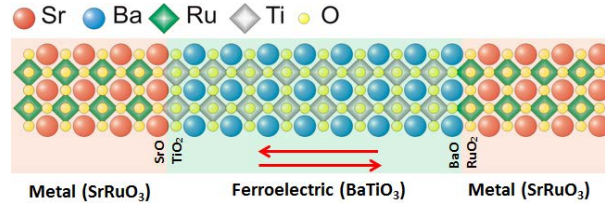
Figure 2.2 $SrRuO_3$/$BaTiO_3$/$SrRuO_3$: unit-cell by unit-cell growth leads to asymmetric

interfaces.

Density functional theory calculations of atomic and electronic structures were performed

using the plane-wave projector-augmented-wave (PAW) method implemented in the

Vienna Ab Initio Simulation Package (VASP) [58]. A plane wave cutoff energy of 500

eV and the local density approximation (LDA) for the exchange and correlation

functional were used in all calculations. Atomic relaxations were converged using an

8×8×1 Monkhorst-Pack k-point sampling of the Brillouin zone until forces were less than

20 meV/Å.

We study a series of several related heterostructure supercells of the form

$[SrRuO_3]_4/[BaTiO_3]_n/[SrRuO_3]_4$ or $[SrRuO_3]_4/[BaTiO_3]_n[SrTiO_3]_m/[SrRuO_3]_4$ with $n =$

8, 6, 5, 4 and $m = 1, 2$. In Figure 2.2, we show a $SrRuO_3/BaTiO_3/SrRuO_3$ heterostructure

with m=8. $SrTiO_3$, $BaTiO_3$ and $SrRuO_3$ belong to the same pseudocubic perovskite-

oxide family with formula unit ABO_3. To simulate coherent epitaxial growth on a (001)

oriented substrate of $SrTiO_3$ we constrain the in-plane structure of each bulk material

component of the heterostructure to a 1×1 cubic perovskite cell with lattice constant $a =$

3.871Å consistent with the calculated LDA lattice constant of cubic $SrTiO_3$ and perform

full relaxation of the internal z-coordinates and tetragonal out-of-plane lattice constant c.

For the metallic $SrRuO_3$ we find a centrosymmetric tetragonal structure with $c/a = 1.013$

and for ferroelectric $BaTiO_3$ we find a polar structure consistent with previous

calculations and a c/a ratio of 1.055. For $SrTiO_3$ the structure remains cubic with $c/a = 1$.

The supercells are then constructed by stacking these structural unit cells along the [001]

direction (which we consider the z-axis) and performing full internal relaxation of the

supercell subject to the same in-plane constraint. Figures 2.3(a) and 2.4(a) show

schematic side views of the $SrRuO_3/[BaTiO_3]_8/SrRuO_3$ and

$SrRuO_3/[BaTiO_3]_6[SrTiO_3]_2/SrRuO_3$ supercells, respectively. Due to computational

limitations, we ignored the antiferrodistortive tilts and rotations of the oxygen octahedra,

which are known to occur in some perovskite oxides [59], that would require a doubling

of the in-plane size of the cell, and therefore double the number of atoms in the system.

These octahedral distortions occur at low temperatures and suppressing them, as has been

done in other first-principles studies [60, 61], should not appreciably affect the stability of ferroelectricity in $BaTiO_3$.

2.2.2   Polarization Stability of $SrRuO_3/[BaTiO_3]_n/SrRuO_3$

The presence or absence of two different stable polarization states in each of the asymmetric $SrRuO_3/[BaTiO_3]_n/SrRuO_3$ heterostructures with $n = 8, 6, 5$ or 4 is tested by careful construction of the initial (pre-relaxation) supercell. During the first step of constructing each supercell the $BaTiO_3$ is assumed to have only a small deviation from its non-polar centrosymmetric state, i.e. with small relative displacement of Ti and Ba atoms with respect to their in-plane oxygen neighbors either along $+z$ or $–z$. The polarization state with polarization pointing away from the BaO/RuO_2 interface was easily established for all $BaTiO_3$ thicknesses tested. In this case, the polarization is pointing along $–z$, and we denote this state as the P_- state. For the opposite polarization state in these structures, however, this procedure did not always lead to a stable polarization. In this case, the polarization is pointing along $+z$, and we denote this state as the P_+ state. In the $n = 8$ structure both polarization states are stabilized, as can be seen from the layer-by-layer metal-oxygen relative z-displacements in Figure 2.3(b). The $n = 6$, 5 and 4 structures, however, always relaxed to the opposite, P_- state. In these cases exhaustive tests were performed with different starting polarization structures in an attempt to find a stable P_+ state, but to no avail. This indicates that the $n = 6$, 5 and 4 structures are only mono-stable, with polarization pointing away from the BaO/RuO_2 interface.
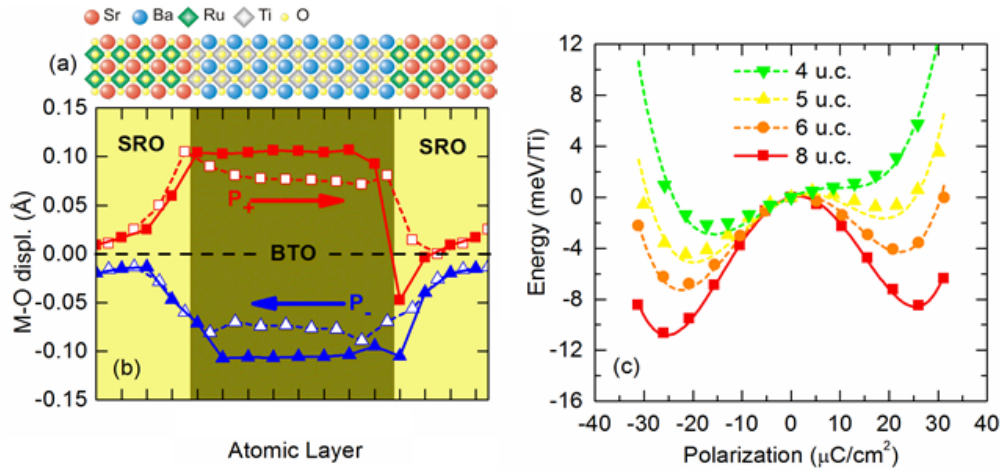
Figure 2.3 (a) The atomic structure of the $SrRuO_3/[BaTiO_3]_8/SrRuO_3$ supercell with the BaO-RuO_2 termination at the top (right) interface. (b) Layer-by-layer profile of the polar metal-oxygen (M-O) relative z-displacements for the two polarization states. Squares and triangles correspond to the P_+ and P_- states, respectively. Open symbols correspond to Ba-O and Sr-O displacements; closed and open symbols correspond to Ti-O_2 and Ru-O_2 displacements, respectively. (c) The total energy per Ti atom calculated form first-principles (symbols) and phenomenological modeling (curves) as a function of z-averaged polarization of $BaTiO_3$ for $SrRuO_3/[BaTiO_3]_n/SrRuO_3$ heterostructures with different number of $BaTiO_3$ unit cells: n=8, 6, 5 and 4 (squares, circles, up-triangles, down-triangles). The solid curve for $n = 8$ is a fit to the phenomenological model (see section III). The dashed curves for the thinner structures use the thickness-independent fitting parameters derived from $n = 8$ fit.

The origin of this preference for the P_- state can be discerned by examination of the metal-oxygen displacements of the $n = 8$ structure shown in Figure 2.3(b). The first

point to notice is that the Ba-O and Ti-O_2 relative displacements all maintain the same sign and roughly the same magnitude throughout the $BaTiO_3$ layer, indicating that the ferroelectric polarization is more-or-less uniform. Second, we note that there are also Sr-O and Ru-O_2 displacements whose magnitude decay away from the interfaces into the bulk of the $SrRuO_3$ metallic electrode. For the most part these polar displacements in the $SrRuO_3$ follow the ferroelectric polarization in the $BaTiO_3$. This follows from the fact that the electrodes possess a finite screening length and electric fields can penetrate them to cause an ionic polar response of the structure. This effect plays an integral role in the electrostatic properties of heterostructures containing metallic oxides and has been studied both theoretically [20, 62] and experimentally [63] in different materials systems. The exception in our case, however, appears to be at the BaO/RuO_2 terminated interface for the P_+ state where the polar displacements in the first two RuO_2 layers of the electrode are opposite to the ferroelectric polarization. The signature of this built-in distortion at the BaO/RuO_2 interface also appears in the P_- state as an enhanced negative polar displacement on the first interface RuO_2 layer in Figure 2.3(b).

The interface dipole arises due to a mismatch between ionic radii: the Sr-Ti interface can be viewed as one cell of $SrTiO_3$, whose cationic radii complement one another so that it has a preference to be centrosymmetric, and will therefore only develop off-centering in response to an electric field. At the Ba-Ru interface, however, Ba has a larger ionic radius than Sr and, just as it does in $BaTiO_3$, leads to off-centering of the B-site cation (Ru^{4+} in this case) with respect to the co-planar oxygen ions. The asymmetric environment of the interfacial Ru, however, strongly favors only one orientation

(negative in our case). In addition, $BaRuO_3$, which is essentially what we have at the Ba-Ru interface, only assumes the pseudo-cubic-perovskite structure similar to $SrRuO_3$ at high pressures due to the larger A-site cationic radius [64]. The presence of a built-in interface dipole at the $BaTiO_3/SrRuO_3$ interface with this termination has been noted in previous works [37, 60]. We note, however, that this dipole forms due to fixed interface displacements and hence has a different origin compared to the charge mismatch effect [63] or the effect of a polar interface [65].

The question remains as to what role, if any, this built-in dipole affects the polarization stability. First, we note that the two polarization states in the $n = 8$ structure differ in energy by $E_+ - E_- = 2.15$ meV/Ti, where $E_\pm$ is the energy of the $P_\pm$ state. In addition, the polar displacements in the $BaTiO_3$ are slightly larger for the P_- state than for the P_+ state. Both are consistent with the idea of a built-in electrostatic interface dipole pointing in the $-z$ direction.

To gain a more comprehensive, though only semi-quantitative, picture of the interface dipole effect on the polarization stability, we performed a series of calculations which interpolate between these two polarized states. The two polarization states differ only in the atomic z-positions, with atom m having z coordinate $z_m^\pm$ in the $P_\pm$ state. Using these positions we construct a series of structures parameterized by the dimensionless constant λ with z-coordinates

$$z_m(\lambda) \;=\; (1-\lambda)\, z_m^+ + \lambda z_m^-, \tag{2}$$

and perform fully self-consistent calculations to obtain the energy of each structure, $E(\lambda)$. To obtain the energy versus polarization we estimate the local polarization distribution

within $BaTiO_3$ using a model based on the Born effective charge [66] by computing the

local polarization $P(z)$ in the $BaTiO_3$ as follows:[*]

$$P(z) = \frac{e}{\Omega} \sum_{m=1}^{N} Z_m^* \delta z_m \ . \tag{3}$$

Here N is the number of atoms in the primitive unit cell, δz_m is the displacement of the

m^{th} atom away from its position in the centrosymmetric structure, and Ω is the volume of

the unit cell. The Born effective charges Z_m^* are 2.77 and 7.25 for Ba and Ti, respectively,

and -2.15 and -5.71 for O ions in the TiO_2 and BaO planes, respectively [2]. Using these

values the polarization of the strained bulk $BaTiO_3$ is calculated to be $27\mu C/cm^2$, which

is in excellent agreement with our calculated value of $26 \ \mu C/cm^2$ based on the first-

principles Berry phase method [14].

For the supercell heterostructure we then average this $P(z)$ over the $BaTiO_3$ layer

for each intermediate scaled structure to obtain $P(\lambda)$ and therefore $E(P)$, which is plotted

as squares for the $n = 8$ case in Figure 2.3(c). [The curves in Figure 2.3(c) correspond to

the zero-temperature phenomenological modeling discussed in Section 2.3 below.] It is

seen that this double well potential is asymmetric due to the presence of the built-in

interface dipole. The two minima correspond to the two stable polarization states, and the

well depth with respect to $P = 0$ for each minimum corresponds to an effective barrier for

polarization reversal. This barrier height, however, only corresponds to a very restricted

path through the dense structural phase space for polarization reversal defined by Eq. (2).

---

[*] We note that the method based on the Born effective charges calculated for bulk ferroelectrics cannot provide a quantitatively accurate description of the local polarization distribution in heterostructures due to the effects of interfaces and local fields which do not exist in the bulk. Nevertheless, we find this approach valuable for a semi-quantitative exploration of the polarization behavior.

Instead we can view these barrier heights as an upper bound on the minimum energy required for switching in real systems where reversal can occur through a myriad of other routes: e.g. here we only consider a path where polarization remains more-or-less uniform throughout the $BaTiO_3$ during reversal, whereas, in reality, developing a non-uniform polarization may significantly lower the barrier. Nevertheless, this energy profile provides clear insight into how the interface dipole affects polarization stability.

We use the same procedure to explore the energetics of the $n = 6$, 5 and 4 structures, which are also plotted in Figure 2.3(c). For these structures, however, a stable P_+ state does not exist and we use an artificial procedure to construct a state with which to compare the P_- state. This is done by taking the stable P_+ structure from the $n = 8$ heterojunction, removing 2, 3 and 4 $BaTiO_3$ unitcells from the center, and rigidly shifting the atomic positions to form a continuous structure corresponding to the average c/a ratio for $BaTiO_3$. With this artificial P_+ state for the thinner structures we then perform the procedure based upon Eqs. (2) and (3) for scaling between the two states and then construct the energy profiles shown in Figure 2.3(c).

Again we find an asymmetric energy vs. polarization profile for each heterojunction. The $n = 4$ structure shows no minima for a P_+ state. For the $n = 6$ and 5 systems, however, we find an apparent P_+ minimum along this parameterized reversal path. These minima should be viewed with caution: they do not correspond to true metastable energetic minima, but instead correspond to projections of unstable saddle-points in the phase space of possible structures. Nevertheless, it is clear that the asymmetry induced by the interface provides a significant contribution to the

destabilization of switchable ferroelectricity in these junctions as $BaTiO_3$ thickness decreases.

It is known that the depolarizing effects due to the incomplete screening of bound polarization charges at the interface between the ferroelectric and a metal electrode can lead to the suppression of a stable polarization [52]. This effect, however, is expected to destroy polarization *symmetrically* in ferroelectric capacitors with identical electrode materials, i.e. will decrease the well depth of both polarization states, and therefore lead to the absence of both polarization minima below a critical thickness. This effect is certainly present in our system, as can be seen by the systematic decrease in well depth as thickness decreases [see Figure 2.3(c)]. In our case, however, the presence of a stable P_- state indicates that the interface dipole effect suppresses the useful switchability of each structure at a higher critical thickness than the one associated with incompletely screened depolarization fields, which would destabilize the P_- state as well.

2.2.3   Polarization Stability of $SrRuO_3/[BaTiO_3]_{n-2}[SrTiO_3]_2/SrRuO_3$

The results reported above provide clear evidence of the detrimental effect of the RuO_2/BaO termination on the formation of switchable ferroelectric polarization in $SrRuO_3/[BaTiO_3]_n/SrRuO_3$ heterostructures. To alleviate this effect, a natural course of action is to eliminate the detrimental BaO/RuO_2 termination in favor of the apparently more stabilizing TiO_2/SrO interface. This may be achieved by depositing a thin $SrTiO_3$ interlayer at the BaO/RuO_2 terminated interface. Below we focus on a two unit-cell $SrTiO_3$ layer between the $BaTiO_3$ and $SrRuO_3$ electrodes, as shown in Figure 2.4(a).
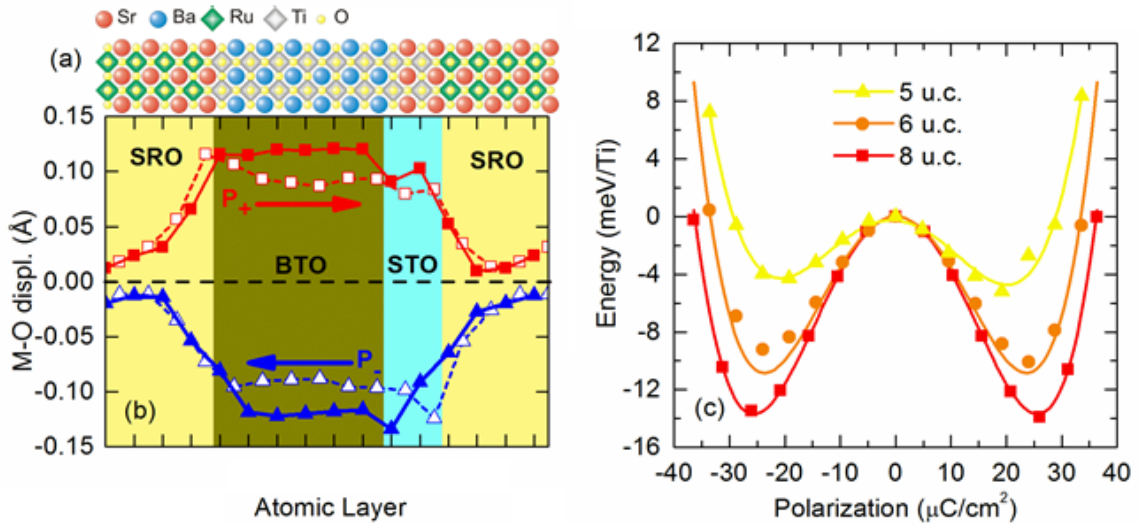
Figure 2.4 (a) Atomic structure of the $SrRuO_3$/$[BaTiO_3]_6[SrTiO_3]_2$/$SrRuO_3$ supercell with the $SrTiO_3$ additional layer at the top (right) interface. (b) Layer-by-layer profile of the polar metal-oxygen (M-O) relative z-displacements for the two polarization states. Squares and triangles correspond to the P_+ and P_- states, respectively. Open symbols correspond to Ba-O and Sr-O displacements; closed symbols correspond to Ti-O_2 and Ru-O_2 displacements. (c) Total energy per Ti atom calculated form first-principles (symbols) and phenomenological modeling (curves) as a function of z-averaged polarization of $BaTiO_3$ for $SrRuO_3$/$[BaTiO_3]_{n-2}[SrTiO_3]_2$/$SrRuO_3$ heterostructures with different number of $BaTiO_3$ unit cells: $n = 8$, 6 and 5 (squares, circles, up-triangles, down-triangles).

Calculations of the $SrRuO_3$/$[BaTiO_3]_{n-2}[SrTiO_3]_2$/$SrRuO_3$ structures confirm the stabilizing nature of the $SrTiO_3$ interlayer. In particular, we find that the $P_\pm$ states are nearly degenerate for the $n = 8$, 6, 5 "interface engineered" structures. The layer-by-layer

atomic metal-oxygen relative displacements for the $n = 8$ structure are plotted in Figure 2.4(b). In contrast to the pure $BaTiO_3$ system [Figure 2.3(b)], we find that the sign of the polar displacements in every layer (including in the $SrTiO_3$ and $SrRuO_3$) follows the ferroelectric polarization of the $BaTiO_3$ layer, indicating that there are no detrimental built-in interface dipoles which oppose polarization stability in either polarization state.

Following the same procedure as in Section 2.2.2 above, we calculated the energy profiles for each junction. As seen from Figure 2.4(c), all the energy profiles consist of a nearly symmetric double-well, with each corresponding to a stable polarization state. In addition to the recovered switchability of these junctions, we find surprisingly that the insertion of the $SrTiO_3$ layer has increased the energy well depth and the effective barrier height for each stable state, even for the P_- state. This may indicate that the screening of the depolarization field may actually be enhanced by the presence of the $SrTiO_3$.

We would like to emphasize the fact that the enhanced ferroelectric properties of the heterostructure are obtained by replacing two layers of a *ferroelectric* $BaTiO_3$ by a *paraelectric* $SrTiO_3$. Given the fact that $SrTiO_3$ is unstrained in the system considered, the ferroelectric polarization of the $SrTiO_3$ is not due to strain but induced by the adjacent $BaTiO_3$ layer. The overall enhancement of ferroelectric properties of the heterostructure results from elimination of the unfavorable interface termination. This behavior is different from the enhanced ferroelectricity found in layered ferroelectric/paraelectric heterostructures induced by strain [22, 23].

Our calculations for a thinner $SrTiO_3$ layer of one unit cell thickness predict similar behavior: changing the interface termination from BaO/RuO_2 to TiO_2/SrO results

in dramatic enhancement of ferroelectric properties and leads to switchable polarization

for thinner $BaTiO_3$ layers. We note that the system with one unit cell $SrTiO_3$ at the

BaO/RuO_2 interface is identical to a system where $BaTiO_3$ layer has the TiO_2

termination at the two interfaces. Finally, our calculations for a $SrTiO_3$ layer deposited at

the SrO/TiO_2 interface, i.e. the $SrRuO_3/[SrTiO_3]_2[BaTiO_3]_{n-2}/SrRuO_3$ heterostructure,

do not predict enhanced ferroelectric properties. This result is expected due to the

unfavorable BaO/RuO_2 termination remaining in this system.

2.3   Phenomenological model of polarization stability

To obtain further insight into the effect of interfaces on ferroelectric polarization stability

and explore this effect at finite temperatures we employ a phenomenological model

developed by Gerra *et al* [60]. This model is based on the Ginzburg-Landau theory of

ferroelectrics applied to thin films [67] that includes explicitly the term which depends on

the interface polarization [68, 69]. We consider a short-circuited ferroelectric film

sandwiched between two electrodes. The Landau free energy includes a bulk term

proportional to the film thickness and interface terms which are assumed to be different

for the two interfaces.

2.3.1   Stability of $SrRuO_3/[BaTiO_3]_n/SrRuO_3$ at finite temperatures

Specifically, for the $SrRuO_3/BaTiO_3/SrRuO_3$ heterostructure with asymmetric interfaces

SrO/TiO_2 and RuO_2/BaO, the free energy Φ per unit surface area of the ferroelectric for

two polarization states, P_+ and P_-, is given by equations

$$\Phi\left(P_{+}\right)=\left(A_{0}P_{+}^{2}+BP_{+}^{4}\right)h_{BTO}+X_{+}P_{+}^{2}+CP_{+}$$

$$\Phi\left(P_{-}\right)=\left(A_{0}P_{-}^{2}+BP_{-}^{4}\right)h_{BTO}+X_{-}P_{-}^{2}+CP_{-}.$$

(4)

Here A_0 and B are parameters determined by the bulk properties of BaTiO$_3$, and h_{BTO} is

the BaTiO$_3$ layer thickness corresponding to n unit cells of BaTiO$_3$. The parameters $X_{\pm}$

and C correspond to interface contributions to the free energy, so that $X_{\pm} = \eta_1 + \eta_2 + $

$\lambda_{\pm}/\varepsilon_0$ and $C = \Delta\varphi_2 - \Delta\varphi_1 + \zeta_1 - \zeta_2$. Here $\zeta_{1,2}$ and $\eta_{1,2}$ are first- and second-order

coefficients in the Taylor expansion of the free energy in terms of P near interfaces

(indices 1 and 2 denote left and right interfaces); $\lambda_{\pm} = (\lambda_1^{\pm} + \lambda_2^{\pm})/2$, where $\lambda_1^{\pm}$ and $\lambda_2^{\pm}$ are

the effective screening lengths of the two interfaces corresponding to $P_{\pm}$; $\Delta\varphi_1$ and $\Delta\varphi_2$

are work function steps at the two interfaces, as defined in Refs. 21 and 60. $\Delta\varphi_{1,2}$ and $\zeta_{1,2}$

are independent of the direction of P and therefore C is chosen the same for both

polarizations. By fitting the energy of bulk BaTiO$_3$ as a function of ferroelectric

displacements, we find $A_0 = -1.318 \cdot 10^9$ C^{-2}m^{2}N and $B = 6.071 \cdot 10^9$ C^{-4}m^{6}N. By fitting

the $n = 8$ energy data in Figure 2.3 (c) to Eq. (4) we find the surface parameters $C = $

0.11V, $X_+ = 1.437$ m^2/F, and $X_- = 1.966$ m^2/F consistent with the respective parameters

reported for the identical system in Ref. [60]. Using these parameters we find that the

phenomenological model is able to describe almost perfectly our first-principles results

not only for the $n = 8$ structure but also for the thinner $n = 6, 5$ and 4 structures, as is seen

from the dashed curves in Figure 2.3(c). Therefore, the phenomenological model,

combined with first-principles calculations, is effective to study ferroelectricity of the

heterostructures considered in our work.
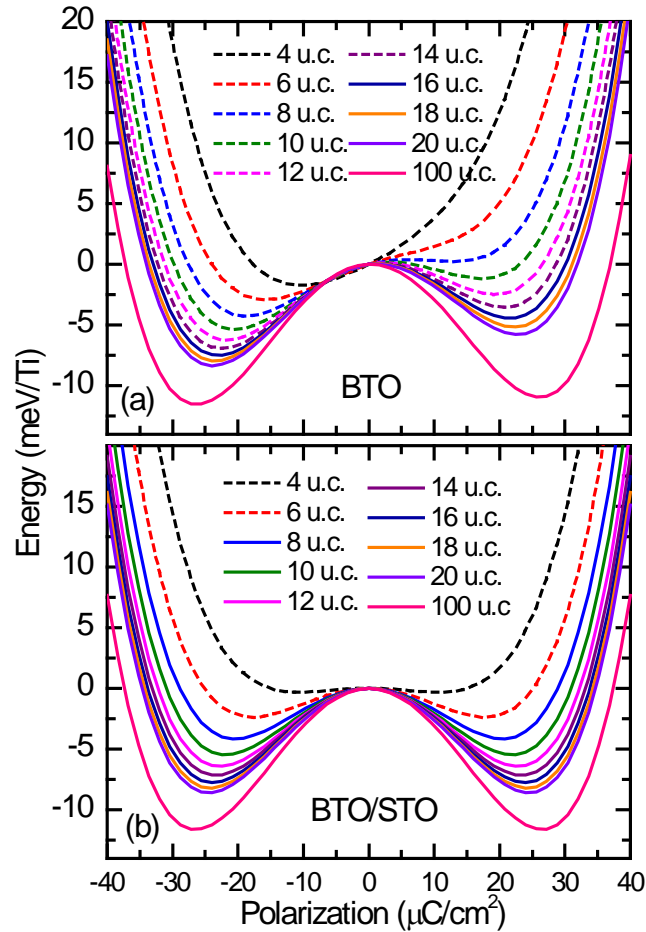
Figure 2.5 Free energy per Ti atom as a function of average polarization predicted by phenomenological modeling at finite temperature $T = 300$K for

$SrRuO_3/[BaTiO_3]_n/SrRuO_3$ (a) and $SrRuO_3/[BaTiO_3]_{n-1.5}[SrTiO_3]_{1.5}/SrRuO_3$ (b)

structure with different numbers of titanate unit cells (u.c.), n. Solid curves correspond to those structures with both energy wells deeper than 4 meV/Ti, indicating switchable bi-stability according to the criteria described in Sec. 2.3.1. The dashed curves correspond to those structures with at least one energy well less than 4 meV deep, indicating the absence of switchability.

The calculations presented so far have assumed zero temperature. In the spirit of the Ginzburg-Landau approach, however, finite temperatures can be taken into account by replacing the quadratic parameter A_0 of the bulk with $A = A_0(T_c - T)/T_c$, where $T_c = 900$ K is an approximate ferroelectric transition temperature of $BaTiO_3$ under ~2% compressive strain as on $SrTiO_3$ [70, 71]. Assuming room temperature, $T = 300$K, we can therefore predict the thickness dependence of ferroelectric stability of the $SrRuO_3/[BaTiO_3]_n/SrRuO_3$ heterostructures even for larger thicknesses as plotted in Fig. 2.5(a). The interface effect caused by the built-in dipole is still present as demonstrated by the fact that the double well potential is asymmetric, and that the P_+ state is less stable than the P_- state.

To estimate the critical thickness for the stability of the P_+ state, and therefore a switchable ferroelectric state, we employ the following criteria to these energy profiles: (i) An energy minimum with $P > 0$ must exist; (ii) If an energy minimum does exist for $P > 0$, such a minimum is only considered stable if the energy minimum is less than -4 meV/Ti, i.e only if the well depth is larger than 4 meV/Ti. This second criterion stems from the fact that the energy profiles in Figures 2.4 and 2.5 correspond to the restricted reversal path discussed in Section 2.2.2. Since we find in Figure 2.3(c) that the well depth of the $n = 6$ structure is apparently ~4 meV along this path, but is not in fact stable when taking into account the possibility of a non-uniform polarization (as is true in the first-principles relaxation) we estimate that the well depth for reversal along our restricted path is overestimated by the same amount, 4 meV. Applying these criteria to the energy profiles at $T = 300$ K in Figure 2.5(a), we find that when the $BaTiO_3$ thickness is below a

critical thickness of about 16 unit-cells (dashed curves in Figure 2.5(a)), the P_+

polarization state is no longer stable.

2.3.2   Stability of SrRuO$_3$/[BaTiO$_3$]$_{n\text{-}2}$[SrTiO$_3$]$_2$/SrRuO$_3$ at finite temperatures

The phenomenological modeling of the "interface engineered" structure with the SrTiO$_3$

layer inserted proceeds in a similar manner. The new termination on interface caused by

SrTiO$_3$, however, must be carefully considered. Geometrically, this structure can be

viewed as SrRuO$_3$/[BaTiO$_3$]$_{(n\text{-}1.5)}$[SrTiO$_3$]$_{1.5}$/SrRuO$_3$ with BaTiO$_3$ terminated by TiO$_2$

on both sides and one monolayer of SrO in SrTiO$_3$ can be viewed as part of SrRuO$_3$.

Because we now have the same termination on both sides, the parameter which describes

asymmetry can be considered negligible, i.e. $C \approx 0$. Based on our first-principles

calculations predicting induced ferroelectric polarization in SrTiO$_3$, we introduce an

additional term, $\left(A^* P_\pm^2 + B^* P_\pm^4 \right) h_{STO}$, to the free energy to describe the SrTiO$_3$ interlayer.

Taking all the above into account, we modify Eqs. (4) as follows:

$$
\begin{aligned}
\Phi\left(P_+\right) &= \left(A P_+^2 + B P_+^4\right) h_{BTO} + X_+^* P_+^2 + \left(A^* P_+^2 + B^* P_+^4\right) h_{STO} \\
\Phi\left(P_-\right) &= \left(A P_-^2 + B P_-^4\right) h_{BTO} + X_-^* P_-^2 + \left(A^* P_-^2 + B^* P_-^4\right) h_{STO}
\end{aligned}
\tag{5}
$$

where now h_{BTO} is the BaTiO$_3$ layer thickness corresponding to $(n-1.5)$ unit cells of

BaTiO$_3$, h_{STO} is the SrTiO$_3$ layer thickness corresponding to 1.5 unit cells of SrTiO$_3$, and

$X^*_\pm = \eta^*_1 + \eta^*_2 + \lambda^*_\pm / \varepsilon_0$ are the new interface parameters. Just as in the case of the pure

BaTiO$_3$ system, the additional parameters are obtained by fitting the energy data in Fig.

2.4(c) for the $n = 8$ SrRuO$_3$/[BaTiO$_3$]$_{n\text{-}1.5}$[SrTiO$_3$]$_{1.5}$/SrRuO$_3$ heterostructure. In this

process, however, due to the accuracy of the polarization calculation, we simply assume

that the spontaneous polarization $P_\pm$ of the system is the average polarization only within the 6 BaTiO$_3$ unit cells. Fitting reveals that $(A^* h_{STO} + X_+^*) = 1.156 \text{m}^2/\text{F}$, $(A^* h_{STO} + X_-^*) = 1.173 \text{m}^2/\text{F}$ and $B^* = 7.571 \cdot 10^9 \text{ C}^{-4} \text{m}^6 \text{N}$.

Calculations for other thicknesses of BaTiO$_3$ were performed using the above parameters fixed and only n being varied. We find that at zero temperature the phenomenological expression, Eq. (5), matches the first-principles calculations very well, as is evident from Figure 2.4(c). To consider the effect of finite temperatures we include temperature dependence in the quadratic bulk term for bulk BaTiO$_3$ as we did for the system without the SrTiO$_3$ interlayer. The results are shown in Figure 2.5(b) for room temperature and indicate the enhanced ferroelectric stability of the interface engineered system. With the substitution of 2 unit cells of BaTiO$_3$ by SrTiO$_3$, the critical thickness (determined by the same criteria described in Sec. 2.3.1 above) with stable and switchable ferroelectric polarization is reduced by a factor of 2 from the system without SrTiO$_3$, demonstrating clear bi-stability down to an $n = 8$ unit-cell structure. This is apparent from Figure 2.5(b) where solid and dashed lines distinguish stable and unstable polarization states.

2.4   Comments on stability against the formation of domains

In addition to the stability of a non-zero polarization in a uniformly polarized film, the stability of the monodomain state itself must be questioned. Below a certain critical thickness, which is generally larger than the critical thickness for the existence of a non-zero and switchable *local* polarization (as we have explored above), the polarization

profile of the film may break up into 180° domains with zero average polarization [19, 46, 47, 48, 49, 50, 51]. Such a polydomain state is unswitchable, and therefore deleterious for applications. The question arises as to how the asymmetry of interfaces affects the critical thickness for the formation of a polydomain state. While a first-principles approach has previously been applied to explore a polydomain state [50], finding the critical thickness for such a transition to occur is a daunting task due to the prohibitively large requirements on the size of the supercell. Instead, the problem is generally more tenable in terms of the phenomenological theory of ferroelectricity. Such a theoretical approach has been developed by Pertsev and Kohlstedt [49], where the possibility of asymmetric interfaces can be incorporated in a straightforward fashion. While a detailed analysis of the interface dipole effect on domain formation is beyond the scope of this work, a qualitative description is easy to formulate in terms of the structures we study here. A monodomain, uniform, polarization state has a propensity to lower its electrostatic energy due to the depolarizing field by forming domains. In the case of asymmetric interface, the parameter C, described in Section 2.3.1, will effectively contribute a term to the depolarizing field of the form $-C/t$, independent of the polarization direction. In the case of the P_+ state, this contribution will effectively increase the depolarizing field, thereby increasing the critical thickness required for a stable and switchable monodomain state. Preliminary phenomenological modeling based on the theory developed by Pertsev and Kohlstedt [49] does indeed agree with this qualitative prediction, and further analysis will remain as the subject of a future study.

2.5   Experimental evidence

Our results are supported by experiments performed by our colleagues [43]. Here we focus on the experimental data relevant to our discussion. To verify our theoretical predictions, several epitaxial $BaTiO_3$-based heterostructures with engineered interfaces have been grown (Fig. 2.4(a)) and their switching behavior are studied. Single-crystalline $BaTiO_3$ films (with a thickness of 24 unit cells) have been fabricated by pulsed laser deposition (PLD) using atomically-controlled layer-by-layer growth on atomically smooth (001) $SrTiO_3$ substrates with single-crystalline top and bottom $SrRuO_3$ electrodes [71, 72]. As has been proposed in the modeling approach, interface engineering has been realized by introducing a $SrTiO_3$ layer with the thickness of 2 unit cells between the $BaTiO_3$ and $SrRuO_3$ layers (Figure 2.6(a)). Before the measurements, the samples were poled by application of voltage pulses of +4 V, which is well above the threshold voltage. In piezoresponse force microscopy (PFM) testing, the parameter directly related to the remanent polarization value is the initial piezoresponse amplitude signal at 0 V. It can be seen (Figure 2.6(b)) that for the reference $SrRuO_3/BaTiO_3/SrRuO_3$ and for the engineered bottom (b-STO) samples as shown in Figure 2.6(a), the initial PFM amplitude and thus the local remanent polarization values are close to zero. On the other hand, the engineered top (t-STO) sample as shown in Figure 2.6(a) exhibits a much higher initial PFM amplitude signal illustrating an enhanced remanent polarization in the sample with the engineered top interface.

Further support for the proposed mechanism of polarization retention enhancement follows from Electrostatic Force Microscopy (EFM) studies of the $BaTiO_3$
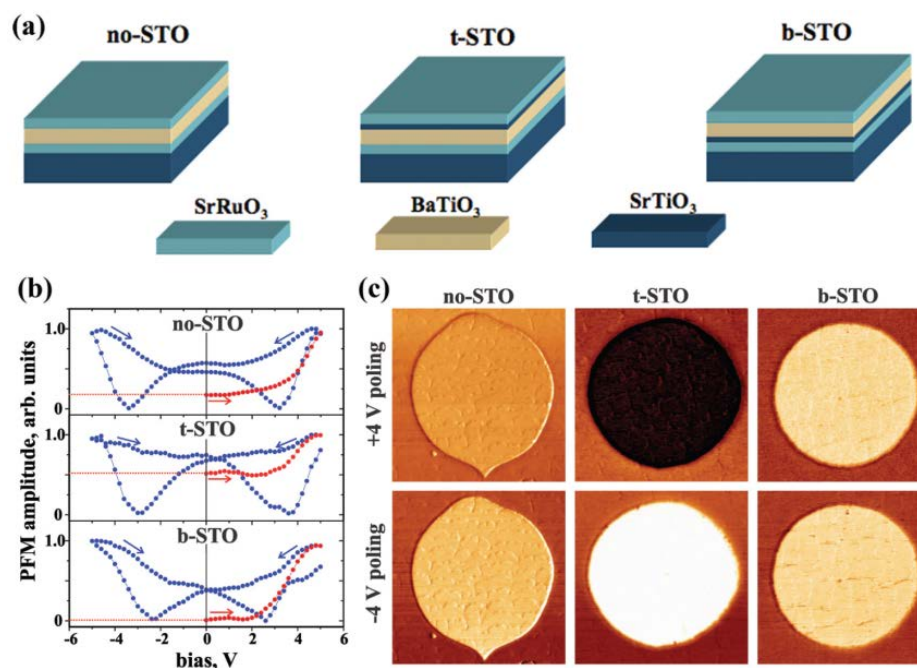
Figure 2.6 (a) Schematic diagrams of the reference $SrRuO_3/BaTiO_3/SrRuO_3$

heterostructure (no-STO) and heterostructures with engineered top (t-STO) and bottom

(b-STO) interfaces. Thickness of the $BaTiO_3$ and $SrTiO_3$ layers is 24 u.c. and 2 u.c.,

respectively. (b) PFM hysteresis loops for no-STO, t-STO and b-STO heterostructures

after application of +4 V poling pulses. The first quarters of the cycles are shown in red

with arrows indicating the direction of voltage change. A difference in the initial (at zero

bias) PFM amplitude illustrates a difference in remanent polarization values for different

heterostructures. (c) EFM images of the no-STO, t-STO and b-STO heterostructures after

poling by +/-4 V pulses. Contrast inversion upon the change of the pulse polarity is

attributed to the change of screening charge on the electrodes and indicates a presence of

a switchable polarization with two stable states. From ref. [43]

heterostructures subjected to poling by positive and negative voltage pulses. Note that EFM is sensitive to the presence of the surface charge and, as such, can address the issue of polarization stability by detecting the screening charge retained on the electrodes after poling. The EFM images of the reference sample and sample with engineered heterostructures after +/-4 V poling are shown in Figure 2.6(c). It is seen that while poling of the reference $SrRuO_3/BaTiO_3/SrRuO_3$ sample by negative or positive pulses does not lead to any contrast change, the same poling procedure performed on the t-STO sample results in the appearance of strong reversible EFM contrast suggesting induction of the screening charge in the electrode. For the experimental conditions used in these measurements, dark EFM contrast corresponds to the positive charge signal (bright contrast indicates negative charges). Based on this observation of the reversible EFM signal and its correlation with the sign of the poling voltage, there was confirmation that the resulting EFM contrast is indeed due to the screening charge on the electrodes and thus indicates a presence of stable polarization in the t-STO sample after poling. No sign of the EFM signal decay over the period of several hours was detected suggesting high stability of the polarization states. Therefore, the experimental results above show that it is engineering of the top interface only that brings about polarization retention enhancement.

2.6   Conclusion

In conclusion, based on the first-principles calculations and phenomenological modeling, we established the importance of interface termination effects on ferroelectric stability of

ultrathin $BaTiO_3$ films with $SrRuO_3$ electrodes. We showed that the presence of the BaO/RuO_2 termination sequence is detrimental to the switchable ferroelectric polarization due to an associated built-in interface dipole. This interface dipole points in the direction from the interface to the $BaTiO_3$ layer and, for thin $BaTiO_3$ layers, can completely suppress one polarization state, thereby making the system unswitchable and thus non-ferroelectric. As a mechanism to alleviate this effect we demonstrate that ferroelectricity can be stabilized by replacing one or two unit cells of $BaTiO_3$ with $SrTiO_3$ at this interface, which essentially removes the detrimental interface dipole due to the BaO/RuO_2 termination in favor of the more stabilizing TiO_2/SrO interface. This method of alleviating unfavorable interface structures should be an efficient route to realize stable and switchable polarization in ferroelectric thin film heterostructures.

Chapter 3 *Effect of electron screening on ferroelectric stability*

We explore the effect of charge carrier doping on ferroelectricity using density functional calculations and phenomenological modeling. How does the screening of the Coulomb interaction affect the ferroelectric displacements? What is the minimum effective range of the Coulomb force to preserve the ferroelectric instability? What happens with the soft mode with charge doping? The answers to these questions would not only provide a better understanding of the nature of ferroelectricity, but also open new possibilities for functional materials. In this chapter, we discuss this effect by considering a prototypical ferroelectric material, $BaTiO_3$. We demonstrate that ferroelectric displacements are sustained up to the critical concentration of 0.11 electron per unit cell volume. This result is consistent with experimental observations and reveals that the ferroelectric phase and conductivity can coexist. Our investigations show that the ferroelectric instability requires only a short-range portion of the Coulomb force with an interaction range of the order of the lattice constant. These results provide a new insight into the origin of ferroelectricity in displacive ferroelectrics and open opportunities for using doped ferroelectrics in novel electronic devices.

3.1   Is *n*-doped $BaTiO_3$ a ferroelectric metal?

The perovskite ABO_3 ferroelectric compounds, for example $BaTiO_3$, are an especially important group due to the relative simplicity of their atomic structure. The ferroelectric

phase transition in these materials is a displacive transition from a high symmetry

paraelectric phase to a polar ferroelectric phase below the critical temperature. This

transition is characterized by a decreasing frequency of a transverse optical phonon mode

(the soft mode) which drops to zero at the transition point and then becomes imaginary in

the ferroelectric phase, corresponding to a collective displacement of ions from their

centrosymmetric positions with no restoring force [73]. The ferroelectric instability can

be explained by the interplay between long-range Coulomb interactions favoring the

ferroelectric phase and short-range forces supporting the undistorted paraelectric

structure. $BaTiO_3$ is a band insulator. Its ferroelectric distortion is due to the

hybridization of the filled oxygen 2p states and the empty d states of Ti. Additional

hybridizations between O cation 2p and metal anion d orbitals are required to diminish

the short-range repulsion and thus to allow for the ferroelectric transition [74, 75]. This is

supported by first-principles calculations indicating that the large destabilizing Coulomb

interaction yielding the instability is linked to giant anomalous Born effective charges

arising due to the strong sensitivity of O–metal hybridizations to atomic displacements

[76].

While doping a ferroelectric material may enhance its range of functionalities,

charge carriers produced by doping screen the Coulomb interactions that favor the off-

center displacements and eventually quench ferroelectricity. This is why it is naturally

expected that a ferroelectric phase could not exist in conducting materials. However,

ferroelectric semiconductors have been known for a long time [77, 78]. More recently

ferroelectric displacements were observed in oxygen reduced conducting electron doped

BaTiO$_3$ [38, 79]. A phase diagram is shown in Figure 3.1. It was found that the ferroelectric instability is sustained up to a critical electron concentration $n \approx 1.9 \times 10^{21} cm^{-3}$, which corresponds to about 0.1 e per unit cell (u.c.) of BaTiO$_3$.
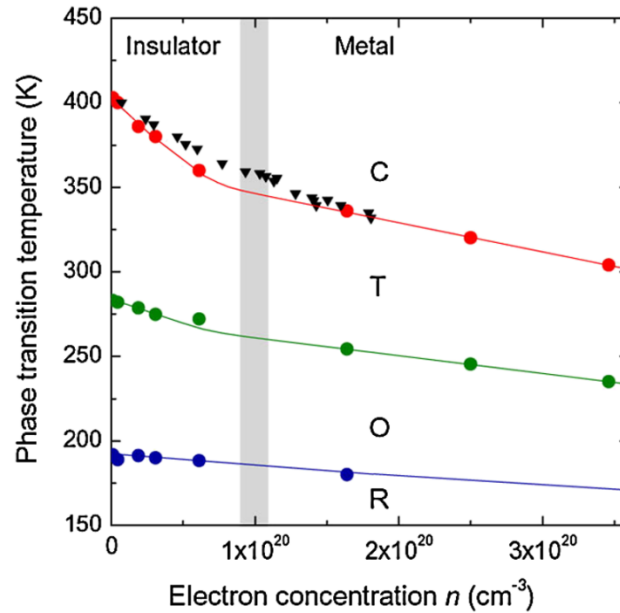
Figure 3.1 Temperature-electron-concentration phase diagram of BaTiO$_3$. The phase transition temperatures for different electron concentrations were compiled from the resistivity and DSC data for polycrystalline BaTiO$_3$. From ref. [38]

A recent neutron scattering data showed that the ferroelectric distortion and metallic phase occur in two distinct phases that do not coexist microscopically [80]. The local distortion of Ti-O bond is found to be stable when oxygen reduction is slight. However, when oxygen-deficient level is high, distorted and undistorted Ti-O bonds were found to coexist. The metallic ferroelectric phase is a mixed phase of tetragonal and cubic structure of BaTiO$_3$.

3.2   Ferroelectrics metal $LiOsO_3$

The long-range Coulomb interactions are responsible for ferroelectric distortion, whereas the itinerant electrons screen the internal electric field. Therefore, ferroelectricity and metallicity is expected to be incompatible. However, Anderson and Blount discussed the possibility of a ferroelectric metal based on Landau theory 60 years ago [81]. They proposed that 'second-order transition usually involve some change in internal symmetry other than mere strain' and 'metallic transitions may be ferroelectric in the sense of the appearance of polar axis.' The pyrochlore compound $Cd_2Re_2O_7$ was considered a ferroelectric metal due to its second-order phase transition and loss of inversion symmetry [82, 83]. However, the low temperature phase of $Cd_2Re_2O_7$ is not ferroelectric but piezoelectric. The internal atomic displacements were induced by external shear stress [84].

Recently, $LiOsO_3$ was found to be a ferroelectric metal as proposed by Anderson and Blount [85, 86]. Figure 3.2 shows the experimental results from ref. [85]. The centrosymmetric to non-centrosymmetric (R3c) transition in metallic $LiOsO_3$ is structurally equivalent to the ferroelectric transition of $LiNbO_3$-type ferroelectric materials, driven by an order-disorder process involving a shift in the mean positions of the Li atoms along the c axis below 140 K.

This experimental finding has led to a number of theoretical studies on this system [87, 88, 89, 90]. The first-principles density functional calculations show that the phase transition occurring in $LiOsO_3$ is quite similar to the phase transition of
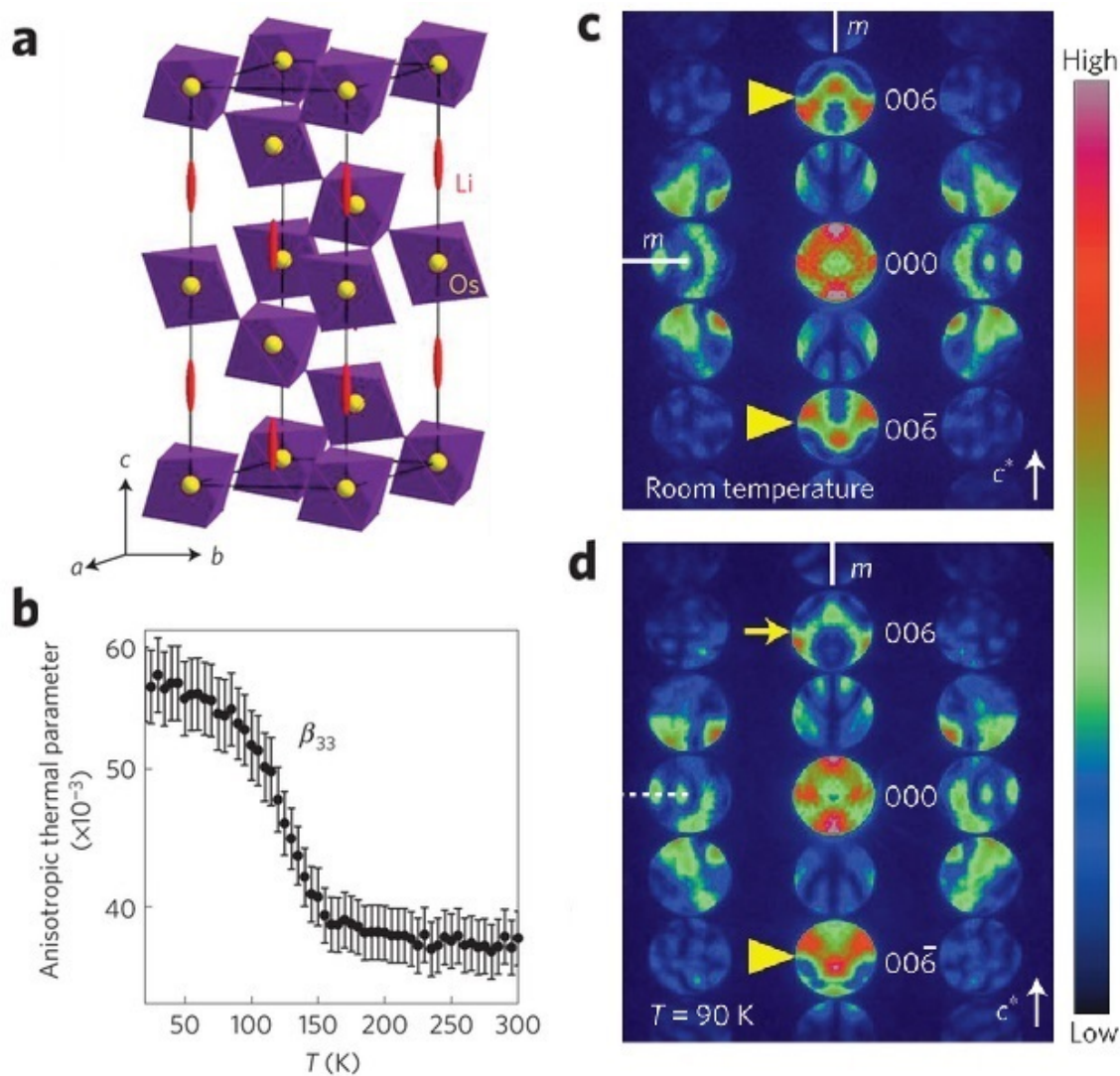
Figure 3.2 (a) High-temperature centrosymmetric crystal structure of $LiOsO_3$ (b)

Temperature dependence of the anisotropic thermal parameter β_{33}, which describes Li

displacements along the c axis. (c,d) Experimental convergent-beam electron diffraction

(CBED) patterns for $LiOsO_3$ taken along the [120] zone axis. Measurements made at

room temperature (c) and 90 K (d). An arrow or arrowhead indicates the absence or

presence of mirror symmetry perpendicular to the c* axis. From ref. [85]

ferroelectric $LiNbO_3$. The noncentrosymmetric phase of $LiOsO_3$ is associated with phonon mode softening and octahedral tilting [88]. Unlike $LiNbO_3$, where both A-site Li and B-site Nb contribute to the ferroelectric transition, in $LiNbO_3$, only Li atom tends to displace towards the neighboring out-of-plane O atoms to lower the electrostatic energy [87]. Another theoretical study points out that the lattice and electronic degrees of freedom are involved in the ferroelectric metal $LiNbO_3$ [89]. This study reveals that while Li-O distortion mode is responsible for ferroelectric-like instability, the Os-O distortions allow for the hybridization of Os-d states and O-p states as in common ferroelectric insulators. The nearly empty e_g orbitals hybridize with the oxygen p orbitals leading to the ferroelectric distortions, while the nearly half-filled t_{2g} orbitals are associated with the metallic response. The study in ref. [90] points out that, the spin-orbital interaction and electronic correlation are not important for the Os-5d electron in $LiOsO_3$ and the charge distribution is highly anisotropic. Therefore the dipole-dipole interaction in polarization direction is not screened.

3.3   Effect of electron doping on ferroelectric instability in $BaTiO_3$

We explore the charge carrier doping effect on ferroelectricity using density functional calculations along with phenomenological modeling based on screened long-range Coulomb interactions and the short-range bonding and repulsion effects. By considering a prototypical ferroelectric material, $BaTiO_3$, we demonstrate that ferroelectric displacements are sustained in electron doped $BaTiO_3$ up to a critical concentration of 0.11 electron per unit cell volume, thus revealing that the ferroelectric phase and

conductivity can coexist. Our investigations show that the ferroelectric instability requires only a short-range portion of the Coulomb force with an interaction range on the order of the lattice constant.

Our calculations employ density functional theory (DFT) implemented in the plane-wave pseudopotential code QUANTUM-ESPRESSO [91]. The exchange and correlation effects are treated within the local-density approximation (LDA). The electron wave functions are expanded in a plane-wave basis set limited by a cut-off energy of 600eV. 14×14×14 and 24×24×24 Monkhorst-Pack k-points meshes are used for structural relaxation and density of states (DOS) calculations respectively. The self-consistent calculations are converged to 10-5 eV/u.c. The atomic positions are obtained by fully relaxing the lattice and all the ions in the unit cell until the Hellmann-Feynman force on each atom became less than 5 meV/Å. The electron doping in $BaTiO_3$ is achieved by adding extra electrons to the systems with the same amount of uniform positive charges in the background. For the undoped tetragonal $BaTiO_3$, our calculation gives the lattice constant a = 3.933Å and c/a = 1.015, polarization P = 28.6 μC/cm2, and Ti-O and Ba-O relative displacements of 0.113Å and 0.091Å respectively, consistent with previous LDA calculations [2]. We note that effects of carrier doping on polarization of $BaTiO_3$, which includes both the ionic and electronic contributions, cannot be calculated using the Berry phase method [14]. Therefore, in this Letter we focus on analyzing the ionic ferroelectric-like displacements and the phonon frequency of the soft mode.
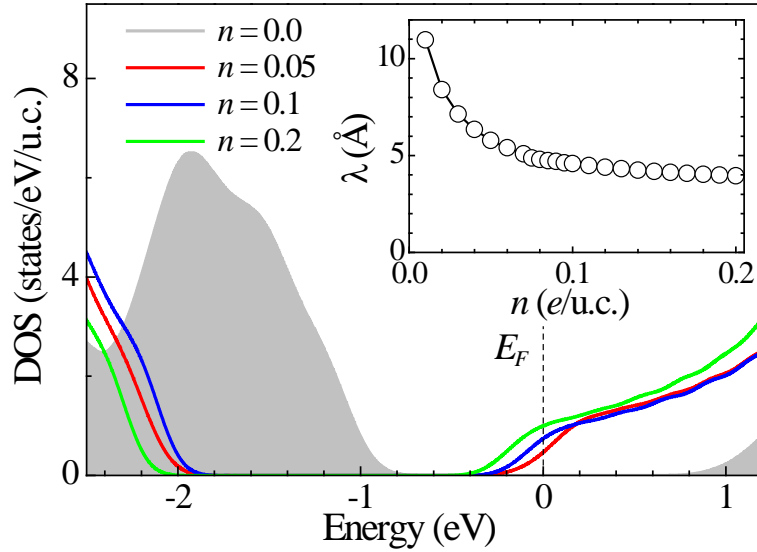
Figure 3.3 The density of states (DOS) of BaTiO$_3$ for electron doping concentration $n =$ 0.0, 0.05, 0.1 and 0.2 $e/u.c.$ The shaded plot is the DOS of undoped BaTiO$_3$. The vertical dashed line denotes the Fermi energy. The inset shows the Thomas-Fermi screening length λ as a function of n.

Doping BaTiO$_3$ with electrons pushes the Fermi energy, E_F, to the conduction band and screens the electric potential of an ionic charge. Figure 3.3 shows the DOS of BaTiO$_3$ for different electron doping concentrations n. A typical scale associated with screening is the screening length, λ, which depends on n. We estimate the screening length using the Thomas-Fermi model according to which $\lambda = \sqrt{\varepsilon / e^2 D(E_F)}$. Here $D(E_F)$ is the DOS at E_F and ε is the dielectric permittivity of undoped BaTiO$_3$ not associated with the spontaneous polarization which we assume to be $\varepsilon \approx 44\varepsilon_0$ [92]. Undoped BaTiO$_3$ ($n =$ 0) is an insulator so that $D(E_F) = 0$ and hence λ is infinite. As n becomes larger, more conduction band states are populated (Figure 3.3), thus increasing $D(E_F)$ and reducing the

screening length. As seen from the inset in Figure 3.3, when n is raised up to 0.2 e/u.c. λ decreases down to about 4 Å.
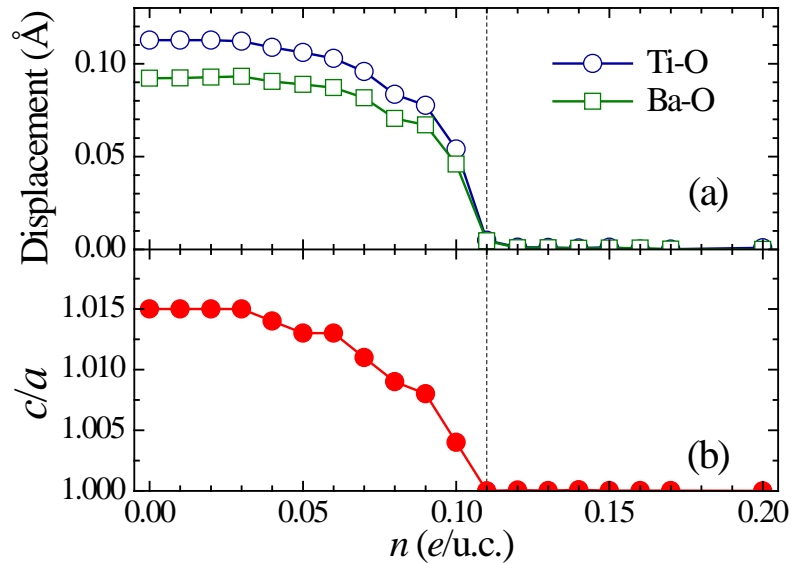
Figure 3.4 Ba-O and Ti-O relative displacements in BaTiO$_3$ (a) and the ratio of out-of-plane lattice constant c and in-plane lattice constant a (b) as a function of electron doping concentration n. The dashed line indicates the critical value n_c.

Next we study the effect of screening due to electron doping on the ferroelectric displacements in BaTiO$_3$. Figure 3.4(a) shows the calculated relative displacements between Ti and O, and Ba and O ions as a function of n. Surprisingly, we find that ferroelectric displacements hardly change with electron doping up to n as high as 0.05e/u.c., and then decay very fast and vanish above the critical electron concentration $n_c = 0.11e$/u.c. The c/a ratio of BaTiO$_3$ under the increasing n, as shown in Figure 3.4(b), also displays a similar critical behavior as that of polar displacements. BaTiO$_3$ transforms

from the tetragonal phase with $c/a = 1.015$ to the cubic phase with $c/a = 1.0$ at $n_c = 0.11e$/u.c. The critical doping concentration n_c found from first-principles is consistent with the experimental result [38]. According to the inset in Figure 3.3 the critical electron concentration $n_c = 0.11e$/u.c. corresponds to a screening length $\lambda_c \approx 5$ Å. Therefore, we conclude that only the short-range Coulomb forces with the interaction range comparable to the lattice constant are responsible for maintaining ferroelectric instability in BaTiO$_3$.
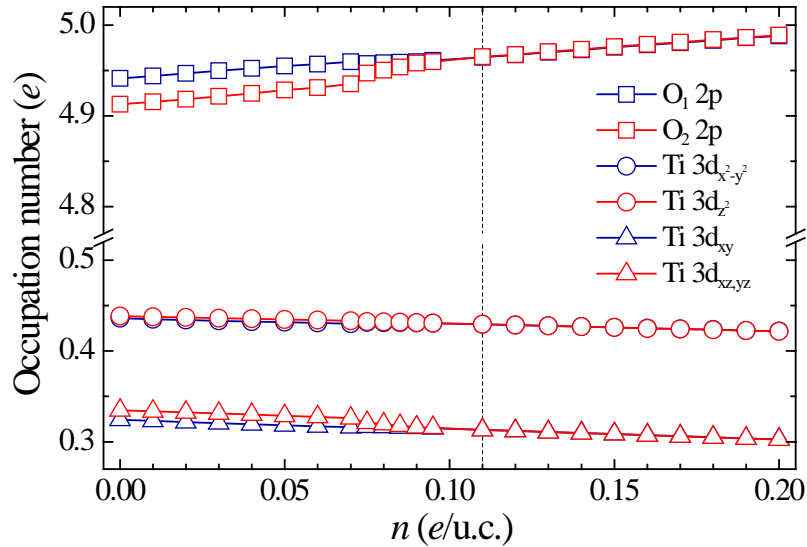
Figure 3.5 Occupation numbers for Ti-3d and O-2p orbitals as a function of electron concentration n. O$_1$ (O$_2$) correspond to O atoms lying in (off) the TiO$_2$ plane.

Since changes in hybridization with doping can also affect the ferroelectric displacements, we calculate the occupation numbers N_d for the Ti-3d orbitals ($3d_{z^2}$, $3d_{x^2-y^2}$, $3d_{xy}$, $3d_{xz,yz}$) and N_p for the O-2p orbitals of BaTiO$_3$ for different n. These occupations reflect the degree of hybridization between Ti-3d and O-2p orbitals. As seen

in Figure 3.5, N_d decreases and N_p increases very slowly with increasing n, so that their change is very small when n is altered from 0 to $n_c = 0.11e$/u.c. This suggests that the changes in hybridization with doping are negligible. Thus, the dominant mechanism contributing to the ferroelectric critical behavior in n-doped $BaTiO_3$ is the screening of Coulomb interactions.

This assertion is further confirmed through our calculations of p-doped $BaTiO_3$. Adding holes in $BaTiO_3$ places the Fermi energy in the valence band that is largely determined by the O-$2p$ orbitals. This is different from the n-doped $BaTiO_3$, where the E_F lies in the conduction band built up of the Ti-$3d$ bands. Despite this difference in the bands involved, we find that the p-doped $BaTiO_3$ demonstrates a similar critical behavior of ferroelectric displacements with a critical hole concentration $p_c \approx 0.12$ e/u.c. We note that previous theoretical studies of the hole doping of $BiFeO_3$ predicted a possibility of enhanced ionic off-centering in this material [93]. We did not find such a trend in our calculations of p-doped $BaTiO_3$.

The signature of the ferroelectric phase transition can also be seen from the softening of the phonon mode in the paraelectric phase when approaching the critical point with the frequency becoming imaginary in the ferroelectric phase [73]. To confirm the phase transition at the critical concentration we have performed phonon calculations within the density functional perturbation theory, as implemented in QUANTUM-ESPRESSO. In these calculations we consider cubic $BaTiO_3$ with the lattice constant fully relaxed. Figure 3.6 shows the lowest frequency of the triple degenerate phonon mode at the Γ point as a function of electron concentration n, along with the relative

cation-anion displacements. We see that the frequency remains imaginary up to an electron concentration as high as $0.11e$/u.c. and becomes real above this critical concentration. This critical behavior of the ferroelectric instability is echoed by the cation-anion displacements in cubic $BaTiO_3$ shown in this figure [Figure 3.6].
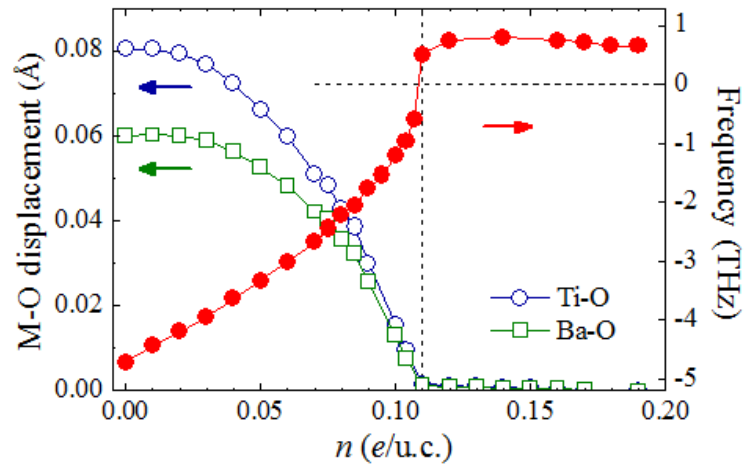
Figure 3.6 Cation-anion (M-O) displacements and phonon frequency of the soft mode at the Γ point in cubic $BaTiO_3$ as a function of electron concentration. Negative sign of frequency indicates an imaginary value of the frequency.

To further understand the critical behavior of ferroelectricity due to the screening of Coulomb interactions, we have developed a physically realistic model explicitly including the screening effect.[*] We consider a 3-dimensional lattice of ions in the cubic perovskite structure. In the Thomas-Fermi approximation each ion is shrouded by an exponentially decaying screening charge density with screening length λ. The analytical

---

[*] The details of our model will be given in Section 3.4.

form of the Coulomb interaction energy w_{ij} between two screened point charge q_i and q_j

at locations $\mathbf{r}_i$ and $\mathbf{r}_j$, respectively, is $w_{ij}(|r_i - r_j|) = q_i q_j w(d)$, where:

$$w(d) = \frac{1}{4\pi\varepsilon_0 d}\left(1 - \frac{d}{2\lambda}\right)e^{-d/\lambda} \tag{1}$$

and $d = |\mathbf{r}_i - \mathbf{r}_j|$ is the distance between the two ions. The factor $(1 - d/2\lambda)e^{-d/\lambda}$ in Eq. (1)

is the distance and screening length dependent coefficient, which reflects the effect of

screening and converges to 1 as $\lambda \to \infty$. The electrostatic energy per unit cell is given

by a lattice sum over all interaction terms of the form (1):

$$W = \frac{1}{2}\sum_{\mathbf{R}}\sum_{i,j=1}^{5}{}' q_i q_j w\left(\left|\mathbf{r}_i - \mathbf{r}_j + \mathbf{R}\right|\right) \tag{2}$$

where $\mathbf{R} = a\,(m_x, m_y, m_z)$ are lattice vectors with the m running over all integers. The

prime sign on the summation in Eq. (2) indicates that for the $\mathbf{R} = 0$ terms, $i = j$ should be

excluded to avoid self-interactions and the factor of ½ takes care of double counting. The

summation in Eq. (2) is performed in the spirit of an Ewald sum.

In addition to the the long-range electrostatic energy, short range Ba-O, O-O and

Ti-O interactions are also included. These short range interactions are described by

Lennard-Jones potentials $E_0[(R_0/r)^7 - 2(R_0/r)^6]$, along with a O-Ti-O three body

potentials described by $k_2(\theta - \theta_0)^2/2$, as parameterized in Ref. [94]. The potential

parameters are fitted to obtain the same Ba-O and Ti-O displacements in undoped

BaTiO$_3$ as those obtained from our DFT calculation. All the parameters of the model,

except λ, were then fixed throughout the calculation.
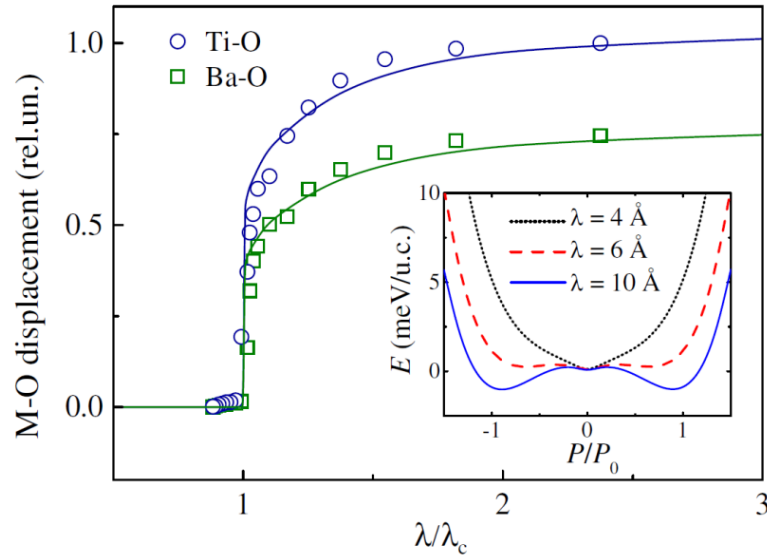
Figure 3.7 Cation-anion relative displacements (in relative units) in cubic $BaTiO_3$ as predicted by the phenomenological model (solid line) and DFT calculation (open symbols). The latter are the same as those in Figure 3.6 (open circles) but plotted versus λ/λ_c according to the Thomas-Fermi relationship between λ and n given in the inset of Figure 3.3. The inset shows the total energy versus polarization (in relative units) for different values of λ, as follows from the phenomenological model.

The total energy of undoped $BaTiO_3$ obtained by adding all the energies described above yields a typical potential [2] with minima at two non-zero polarizations, as seen from the inset in Figure 3.7. As the electron screening length λ begins to decrease with increasing doping, these minima drop in energy slowly in the beginning. When λ approaches the critical value of λ_c, the two wells become shallower quite rapidly. For $\lambda < \lambda_c$, the wells merge into a single well at $P = 0$ indicating a transition to the paraelectric phase. The critical value obtained from the model, $\lambda_c \approx 5.3\text{Å}$, is consistent with that

obtained from the Thomas-Fermi estimate based on our DFT calculations. Figure 3.7 shows M-O displacements versus the normalized screening length. It is seen that the critical behavior predicted by our model (solid line) is in agreement with the results of our DFT calculation (open circles). Thus, our phenomenological model confirms the fact that only a short range portion of the Coulomb interaction is needed to sustain ferroelectric displacements.

The coexistence of the ferroelectric phase and conductivity is very interesting for device applications because such a conducting bistable material has new functionalities. Although in such a material an external electric field induces a flow of electric current which makes switching of the ferroelectric displacements difficult, resistive materials may sustain the coercive voltage. For example, ferroelectric tunnel junctions are switchable despite the current flowing across them [95]. Furthermore, ferroelectric switching can be realized by the applied voltage which rises sufficiently fast in time. A recent prominent example is the resistive switching behavior of semiconducting ferroelectric $BiFeO_3$ [96]. Also, there exist means to switch ferroelectrics with no applied voltage [97]. Doped ferroelectrics may have implications in magnetoelectric devices where the interface magnetization is affected by the ferroelectric polarization charge [25, 98].

3.4   A phenomenological model

3.4.1   Interaction energy between two screened ions

In the Thomas-Fermi approximation each ion is shrouded by an exponentially decaying screening charge distribution with screening length λ. Therefore the potential at $\mathbf{r}$ generated by a point ion charge at $\mathbf{r}_i$ is

$$\phi_i(\mathbf{r}) = \frac{q}{4\pi\varepsilon_0 |\mathbf{r} - \mathbf{r}_i|} e^{-|\mathbf{r}-\mathbf{r}_i|/\lambda} . \tag{3}$$

We can rewrite this in terms of the Fourier transform of a screened point charge as

$$\phi_i(\mathbf{r}) = \frac{q_i}{(2\pi)^3} \int \tilde{\phi}(k) e^{i\mathbf{k}\cdot(\mathbf{r}-\mathbf{r}_i)} d^3\mathbf{k} . \tag{4}$$

The screened Fourier transform is $\tilde{\phi}(k) = \tilde{\phi}_0(k) / \varepsilon(k)$, where $\tilde{\phi}_0(k)$ is the Fourier transform of the potential of a bare ion with unit charge,

$$\tilde{\phi}_0(k) = \frac{1}{\varepsilon_0 k^2} , \tag{5}$$

and $\varepsilon(k)$ is the Thomas-Fermi dielectric function,

$$\varepsilon(k) = 1 + \frac{1}{\lambda^2 k^2} . \tag{6}$$

The total screened charge density of this ion is obtained from the Poisson equation as

$$\rho_i(\mathbf{r}) = -\varepsilon_0 \nabla^2 \phi_i(\mathbf{r}) = \varepsilon_0 \frac{q_i}{(2\pi)^3} \int k^2 \tilde{\phi}(k) e^{i\mathbf{k}\cdot(\mathbf{r}-\mathbf{r}_i)} d^3\mathbf{k} . \tag{7}$$

Given a screened point charge q_j at $\mathbf{r}_j$ the work required to bring in another screened point charge q_i from infinity to $\mathbf{r}_i$ is

$$w_{ij}\left(|\mathbf{r}_i - \mathbf{r}_j|\right) = \int \rho_i(\mathbf{r})\phi_j(\mathbf{r}) d^3\mathbf{r} . \tag{8}$$

Rewriting this integral in terms of the Fourier expressions we obtain

$$w_{ij}\left(\left|\mathbf{r}_i - \mathbf{r}_j\right|\right) = \varepsilon_0 \frac{q_i q_j}{(2\pi)^6} \iiint k^2 \tilde{\phi}(k) e^{i\mathbf{k}\cdot(\mathbf{r}-\mathbf{r}_i)} \tilde{\phi}(k') e^{i\mathbf{k}'\cdot(\mathbf{r}-\mathbf{r}_j)} d^3\mathbf{k} d^3\mathbf{k}' d^3\mathbf{r} \ . \tag{9}$$

Therefore, the interaction energy between screened ions i and j separated by distance

$d = \left|\mathbf{r}_i - \mathbf{r}_j\right|$ can be represented as $w_{ij}\left(\left|\mathbf{r}_i - \mathbf{r}_j\right|\right) = q_i q_j w(d)$, where

$$w(d) = \frac{1}{4\pi\varepsilon_0 d}\left(1 - \frac{d}{2\lambda}\right) e^{-d/\lambda} \tag{10}$$

which converges to the bare Coulomb potential as $\lambda \to \infty$.

3.4.2 Evaluation of total electrostatic energy

The electrostatic energy per unit-cell required to construct the crystal is given by a lattice

sum over all interaction terms of the form (10):

$$W = \tfrac{1}{2}\sum_{\mathbf{R}}\sum_{i,j=1}^{5}{}' q_i q_j w\left(\left|\mathbf{r}_i - \mathbf{r}_j + \mathbf{R}\right|\right) \tag{11}$$

Here $\mathbf{R} = a\,(m_x, m_y, m_z)$, are the lattice vectors with the m running over all integers. The $'$

on the summation over i, j in (11) indicates that for the $\mathbf{R} = 0$ terms, $i = j$ should be

excluded to avoid self-interactions and the factor of ½ takes care of double counting.

For large λ, evaluating (11) via "brute force" summation in real space by

truncating those terms with $|\mathbf{R}| > R_{max}$ is untenable. In the spirit of an Ewald sum, we

break up $w(d)$ into two terms: a long range term, $w_L(d)$, which is amenable to summation

over a reasonably small number of Fourier terms, and a short range term, $w_S(d)$, which

dies off quickly in real space and therefore is amenable to a reasonably small R_{max}, e.g.

encompassing only one or two unit-cells.

Explicitly, the Fourier transform of $w(d)$ in (10) is given by

$$\tilde{w}(k) = \varepsilon_0 k^2 \tilde{\phi}(k)^2 = \frac{\lambda^4 k^2}{\varepsilon_0 (\lambda^2 k^2 + 1)^2} .$$ (12)

The short range contribution to $w(d)$ comes from Fourier terms with large k. Indeed for

large k, (12) falls off only as $1/k^2$, which gives rise to the singularity in $w(d)$ at $d = 0$. To

attenuate these large k contributions out of the Fourier transform, and in order to find the

long range contribution $w_L(d)$ to $w(d)$, we multiply (12) by a Gaussian attenuation factor:

$$\tilde{w}_L(k) = \eta \tilde{w}(k) e^{-\sigma^2 k^2} = \frac{\eta \lambda^4 k^2}{\varepsilon_0 (\lambda^2 k^2 + 1)^2} e^{-\sigma^2 k^2} .$$ (13)

Here η is an as-yet-to-be-determined scaling factor which gives us another degree of

freedom to optimally localize the short-range term (more details below) and σ is a

Gaussian broadening factor roughly corresponding to an effective length of the short-

range interaction, which needs to be chosen judiciously to minimize the error between the

true expression for $w(d)$ and the approximate $w_S(d) + w_L(d)$. Fourier transforming (13)

we find

$$w_L(d) = \frac{1}{(2\pi)^3} \int \tilde{w}_L(k) e^{i\mathbf{k} \cdot \mathbf{d}} d^3\mathbf{k} = \frac{\eta \lambda^4}{2\pi^2 \varepsilon_0 d} \int_0^\infty \frac{e^{-\sigma^2 k^2} \sin(kd)}{(\lambda^2 k^2 + 1)^2} k^3 dk$$ (14)

The short-range contribution $w_S(d)$ is obtained straightforwardly:

$$w_S(d) = w(d) - w_L(d)$$ (15)

Using (14), the leading order terms of w_s as d tends toward infinity we obtain

$$w_S(d \to \infty) \approx \frac{(\eta e^{\sigma^2/\lambda^2} - 1)}{8\pi\lambda\varepsilon_0} e^{-d/\lambda} - \frac{(\sigma^2 \eta e^{\sigma^2/\lambda^2} + \lambda^2 \eta e^{\sigma^2/\lambda^2} - \lambda^2)}{4\lambda^2 \pi \varepsilon_0 d} e^{-d/\lambda} + \frac{\eta\sigma}{2\pi^{3/2}\varepsilon_0 d^2} e^{-d^2/4\sigma^2}$$ (16)

By choosing η so that the first term in (16) is zero, we obtain:

$$\eta = e^{-\sigma^2/\lambda^2} \tag{17}$$

Using (17), the full expressions for $w_S(d)$ and $\tilde{w}_L(k)$ are given by

$$
\begin{aligned}
w_S(d) = {} & \frac{\left(2\lambda^2 + 2\sigma^2 - d\lambda\right)}{16\pi\varepsilon_0\lambda^2 d}\,\mathrm{erfc}\left(\frac{d}{2\sigma} - \frac{\sigma}{\lambda}\right)e^{-d/\lambda} \\
& + \frac{\left(2\lambda^2 + 2\sigma^2 + d\lambda\right)}{16\pi\varepsilon_0\lambda^2 d}\,\mathrm{erfc}\left(\frac{d}{2\sigma} + \frac{\sigma}{\lambda}\right)e^{d/\lambda} - \frac{\sigma^2}{4\pi\varepsilon_0\lambda^2 d}e^{-d/\lambda}, \\
\tilde{w}_L(k) = {} & \frac{e^{-\sigma^2/\lambda^2}\lambda^4 k^2}{\varepsilon_0\left(\lambda^2 k^2 + 1\right)^2}e^{-\sigma^2 k^2}.
\end{aligned}
\tag{18}
$$

Now we return to (11) and approximate it in terms of the long and short range

Ewald contributions:

$$
\begin{aligned}
W' = W_L - W_{self} + W_S = {} & \tfrac{1}{2}\sum_{\mathbf{R}}\sum_{i,j=1}^{5} q_i q_j w_L\left(\left|\mathbf{r}_i - \mathbf{r}_j + \mathbf{R}\right|\right) - \tfrac{1}{2}\sum_{i=1}^{5} q_i^2 w_L(0) \\
& + \tfrac{1}{2}\sum_{\mathbf{R}}\sideset{}{'}\sum_{i,j=1}^{5} q_i q_j w_S\left(\left|\mathbf{r}_i - \mathbf{r}_j + \mathbf{R}\right|\right).
\end{aligned}
\tag{19}
$$

Since we have removed the singularity at $d = 0$ from $w_L(d)$, we can rewrite W_L without

the $'$ by subtracting away the terms for $i = j$ when $\mathbf{R} = 0$ which sum to give rise to the

self-interaction term

$$W_{self} = \tfrac{1}{2}\sum_{i=1}^{5} q_i^2 w_L(0) \tag{20}$$

where

$$w_L(0) = -\frac{\left(3\lambda^2 + 2\sigma^2\right)}{8\pi\varepsilon_0\lambda^3}\,\mathrm{erfc}\left(\frac{\sigma}{\lambda}\right) + \frac{\left(\lambda^2 + \sigma^2\right)}{4\pi^{3/2}\varepsilon_0\sigma}e^{-\sigma^2/\lambda^2} \tag{21}$$

Writing w_L in its Fourier transform, W_L expressed in reciprocal space can be derived as

$$
\begin{aligned}
W_L &= \tfrac{1}{2}\sum_{\mathbf{G}}\sum_{i,j=1}^{5} q_i q_j \frac{1}{(2\pi)^3}\int \tilde{w}_L(k)\, e^{i\mathbf{k}\cdot(\mathbf{r}_i-\mathbf{r}_j)}\delta(\mathbf{k}-\mathbf{G})\, d^3\mathbf{k} \\
&= \frac{1}{2a^3}\sum_{\mathbf{G}}\tilde{w}_L(G)\sum_{i,j=1}^{5} q_i q_j e^{i\mathbf{G}\cdot(\mathbf{r}_i-\mathbf{r}_j)} = \frac{1}{2a^3}\sum_{\mathbf{G}}\tilde{w}_L(G) S(\mathbf{G}),
\end{aligned}
\tag{22}
$$

where we have defined the structure factor

$$
S(\mathbf{G}) = \sum_{i,j=1}^{5} q_i q_j e^{i\mathbf{G}\cdot(\mathbf{r}_i-\mathbf{r}_j)}
\tag{23}
$$

and $\mathbf{G}$ are the reciprocal lattice vectors: $\mathbf{G} = (2\pi/a)(n_x, n_y, n_z)$, where the n runs over all integers up to a maximum cut-off of N_{max}.

By matching the approximate electrostatic energy W' to the true electrostatic energy W, which can be calculated via *brute force* for a few representative structures and screening lengths, we find a maximum error less than 0.1meV for $N_{max} = 7$ and $\sigma = 0.6$ Å.

3.5 Conclusions

In conclusion, using first-principles calculations and a phenomenological model we have demonstrated that ferroelectric displacements are well preserved in doped $BaTiO_3$ until the doping concentration exceeds a critical value of $n_c = 0.11e$/u.c. This critical behavior is due to the electron screening of the Coulomb interactions responsible for the ferroelectric instability. The critical screening length is found to be surprisingly small, about 5Å, demonstrating that the "short range" Coulomb interactions are sufficient to lead to collective ferroelectric displacements. This value may be considered as a

qualitative estimate for a lower limit for the critical size of ferroelectricity in $BaTiO_3$ of a few unit cells. Our results provide a new insight into the origin of ferroelectricity in displacive ferroelectrics and open opportunities for using doped ferroelectrics in novel electronic devices.

Chapter 4 *Ferroelectrically controlled interface resistance*

Ferroelectric polar displacements have recently been observed in conducting electron-doped $BaTiO_3$ (n-BTO). Even through the coexistence of ferroelectric and metallic phase at high doping level is still debatable, it is clear that at low doping level ferroelectric phase is stable and exist as a single phase as pointed out in the previous chapter. The coexistence of a ferroelectric phase and conductivity opens the door to new functionalities that may provide a unique route for novel device applications. Using first-principles methods and electrostatic modeling, we explore the effect that the switchable polarization of n-BTO has on the electronic properties of the $SrRuO_3$/n-BTO (001) interface. Ferroelectric polarization controls the accumulation or depletion of electron charge at the interface, and the associated bending of the n-BTO conduction band determines the transport regime across the interface. The interface exhibits a Schottky tunnel barrier for one polarization orientation, whereas an Ohmic contact is present for the opposite polarization orientation, leading to a large change in interface resistance associated with polarization reversal. Our calculations reveal a five orders of magnitude change in the interface resistance because of polarization switching.

4.1   Effect of ferroelectric on properties of interface

When two different materials are combined to form a heterostructure, atomic and electronic reconstruction at the interface makes properties of the heterostructure quite different from those of the constituting bulk materials. Novel properties such as 2DEG,

superconductivity, magnetism, etc. have been observed in heterostructures composed of oxide thin films. Adding a ferroelectric polarization in the system results in enhanced functionalities and novel properties. These properties are, in particular, driven by the ferroelectric field effect where the polarization charge at the interface causes a depletion or accumulation of charge carriers at the interface. Properties of oxide thin films are very sensitive to the electron (hole) doping, and therefore one should expect a notable changes in the electronic, magnetic and transport properties of such interfacial materials. Especially interesting is the effect of reversal of ferroelectric polarization, which could lead to switchable properties of the interface.

For example, when a ferroelectric is interfaced with a correlated electron oxide electrode material, the reversal of ferroelectric polarization modifies the electronic phase in the electrode and results in the TER effect in a ferroelectric tunneljunction [99, 100, 101]. The electronic and magnetic phases of a carrier-doped correlated-electron oxide are susceptible to the change of carrier density. The ferroelectric polarization tunes the charge density and therefore modifies the phase of the electrode near the interface. For a metal/ferroelectric/$La_{1-x}Sr_xMnO_3$ system, the interfacial phase transition induced TER was studied both theoretically and experimentally [99, 100, 101].

Another example, which is more relevant to the subject of this chapter, is the effect of ferroelectric polarization on a Schottky barrier. A Schottky barrier is formed at the metal-semiconductor interface due to the different work functions. When the interface is created, a charge transfer between the materials leads to a step in the electrostatic potential which is responsible for the Schottky barrier. In addition, the interface bonding

and the interface termination contribute to the electrochemical boundary conditions and thus affect the Schottky barrier height. If one of the two materials constituting the interface is ferroelectric the presence of the bound change at the interface inevitably affects the Schottky barrier height. A change in the bound change due to reversal of ferroelectric polarization modifies the Schottky barrier. Experimental evidence of the dependence of the Schottky barrier height on polarization has been provided by the electrically switchable diode and photovoltaic effects [102] and the TER effect in ferroelectric tunnel junctions [95]. Recently, an experimental method using photoelectron spectroscopy to measure the Schottky barrier height was reported [103].

4.2   Ferroelectrically switchable Schottky barrier

The presence of conductivity in a ferroelectric material provides another possibility to control the Schottky barrier. For example, in a 1994 experiment, Blom and collaborators found bistable conduction characteristic of a p-type semiconducting $PbTiO_3$ sandwiched between Au and $LaSrCoO_3$ layers, resulting in an on/off resistance ratio of about 100 [28]. Assuming that the Schottky barrier height is fixed, they explained this behavior by a change in the Schottky barrier width with reversal of ferroelectric polarization. This assumption of fixed Schottky barrier explains qualitatively the switchable resistance of metal/ferroelectric heterojunction but ignores the fact that the screening change is different for opposite ferroelectric polarization. The screening charge at the interface inevitably influences the height of the Schottky barrier. Recently, switchable rectification and ferroelectric photovoltaic effects were observed in a n-type ferroelectric

semiconductor $BiFeO_3$. This behavior was explained by ferroelectric polarization driving

a transition from Schottky to Ohmic contact at the interface [39, 41].

4.3   Polariztion-controlled Ohmic to Schottky transition at metal/ferroelectric interface
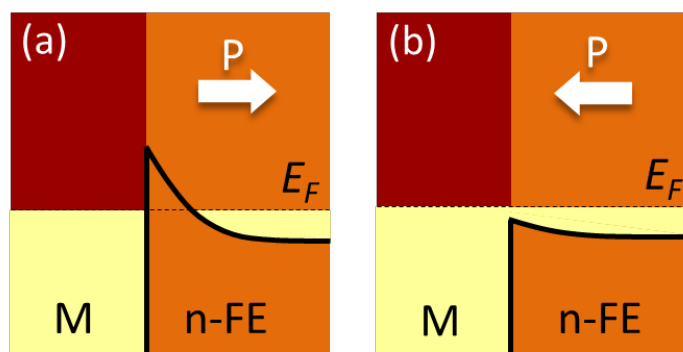
Figure 4.1 Polarization controlled band alignment at in the interface between a metal (M)

and electron-doped ferroelectric (*n*-FE). Arrows indicate the polarization direction. (a)

Polarization pointing away from the interface leads to electron depletion, pulling the *n*-

FE conduction band upward. (b) Polarization pointing into the interface leads to electron

accumulation, pushing the *n*-FE conduction band down. In the case shown here,

polarization reversal leads to a transition from a Schottky tunnel barrier (a) to an Ohmic

contact (b) between M and *n*-FE.

Driven by these developments we explore the effect of polarization on the transport

regime across the interface formed between an oxide metal and a doped ferroelectric,

using density-functional methods and electrostatic modeling. We predict, from first-

principles, a switchable potential barrier driven by the accumulation or depletion of screening charge at the interface in response to ferroelectric polarization reversal. We demonstrate a ferroelectrically-induced change from the Ohmic transport regime, where interface conductance is metallic, to the Schottky regime, where a tunneling barrier is formed at the interface, as depicted in Figure 4.1. This switching leads to a five orders of magnitude change in the interface resistance, and therefore demonstrates interesting potential for device applications.

4.3.1 Atomic and electronic structure

We explore the polarization controlled contact by considering an epitaxial interface between a metallic oxide, $SrRuO_3$, and electron doped $BaTiO_3$ (n-$BaTiO_3$). First-principles calculations are performed using the plane-wave pseudopotential code QUANTUM ESPRESSO [91], where the exchange and correlation effects are treated within the local-density approximation (LDA). We assume that the doping of n-$BaTiO_3$ is 0.06 e/formula unit (f.u.), which is realized by the virtual crystal approximation applied to the oxygen potentials in $BaTiO_3$ [104]. For this doping ($n \approx 1.9 \times 10^{21}$ cm^{-3}), the ferroelectric displacements remain sizable, being about 70% of those in the undoped $BaTiO_3$ as is shown in Chapter 3. The calculations are performed using periodic boundary conditions on a supercell constructed of 15.5 u.c. of $BaTiO_3$ and 10.5 u.c. $SrRuO_3$, as shown in Figure 4.2. We consider a SrO/TiO_2 interface termination at the
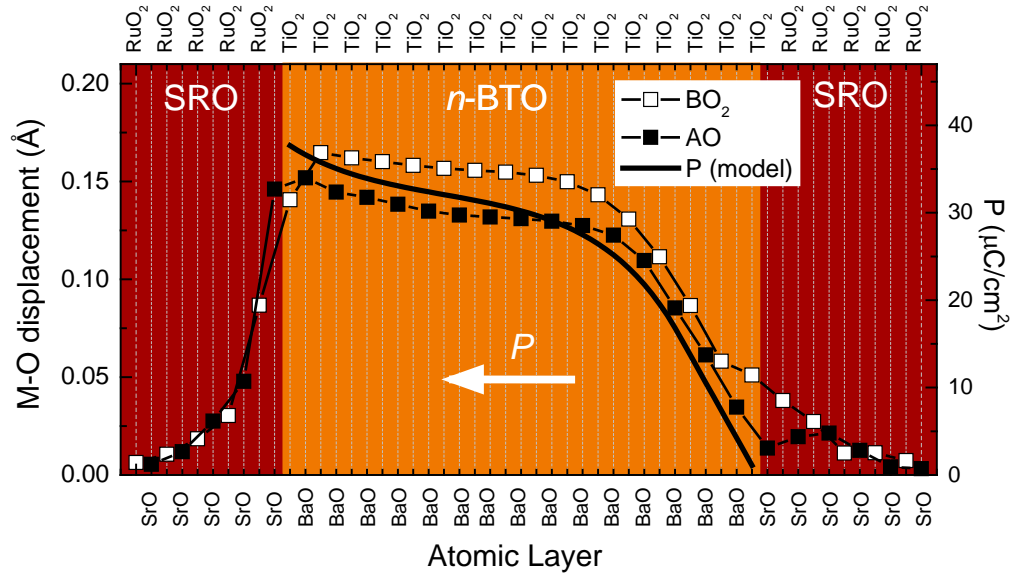
Figure 4.2 Relative z-displacement between cation (M) and anion (O) on each atomic layer of the SrRuO$_3$/n-BaTiO$_3$ supercell. Light squares are for BO$_2$ layers (B = Ti or Ru) and dark squares are for AO layers (A = Ba or Sr). A positive displacement indicates that polarization is pointing to left, as shown by the arrow. The left half of the supercell corresponds to the contact with polarization pointing into the metal, while the right half of the supercell corresponds to the contact with polarization pointing out of the metal, as in Figure 4.1. The solid curve shows the polarization profile obtained from the electrostatic model.

SrRuO$_3$/n-BaTiO$_3$ (001) interface, which is experimentally found to be more stable, as compared to the RuO$_2$/BaO interface [43]. We assume the same SrO/TiO$_2$ terminations at both interfaces in the supercell, which allows us to study the effect of polarization reversal at a given interface by comparing the properties of the two interfaces in the supercell for a single polarization orientation. To simulate coherent epitaxial growth on a

(001)-oriented $SrTiO_3$ substrate we constrain the in-plane lattice constant of the supercell

to be the calculated LDA lattice constant of cubic $SrTiO_3$, $a = 3.871$Å. Using the same

approach we used in Chapter 2, we perform full relaxation of the internal z-coordinates

and overall c/a ratio of the supercell.

Figure 4.2 shows the layer-resolved metal-oxygen (M-O) relative z-displacements

across the supercell, where positive displacements indicate polarization pointing to the

left. Thus, the left interface corresponds to the contact with n-BaTiO$_3$ polarization

pointing into the SrRuO$_3$ metal, while the right interface corresponds to n-BaTiO$_3$

polarization pointing away from the SrRuO$_3$. In the middle of the supercell, n-BaTiO$_3$

exhibits bulk-like polar displacements. At the right interface, however, the M-O

displacements drop sharply, while at the left interface they remain nearly constant (even

slightly enhanced). This behavior is consistent with electric field profile resulting from

the competition between screening, polarization charges and the built-in dipole layer at

the two interfaces, as described in the electrostatic modeling discussed later.

Figure 4.3 shows the calculated layer-resolved density of states (DOS) on the 3d-

Ti orbital across the n-BaTiO$_3$. It is seen that at the left interface the conduction band

minimum (CBM)[*] lies below the Fermi energy, implying that for polarization pointing

toward the SrRuO$_3$ metal the contact is metallic (Ohmic). On the other hand, for three

TiO$_2$ monolayers at the right interface the conduction band minimum lies above the

---

[*] The CBM is determined by first calculating the energy difference between the semi-core O 2s-states and the CBM of bulk n-BTO. This energy difference is then used to determine the layer dependent CBM of n-BTO in the heterostructure. The CBM positions determined in this way are in excellent agreement with the layer-resolved DOS (compare circles with the filled curves in Figure 4.3).

Fermi energy. This implies that for polarization pointing away from the SrRuO$_3$ metal

the contact exhibits a Schottky barrier. The height of this barrier is about 0.4eV and the

width is about 1nm.
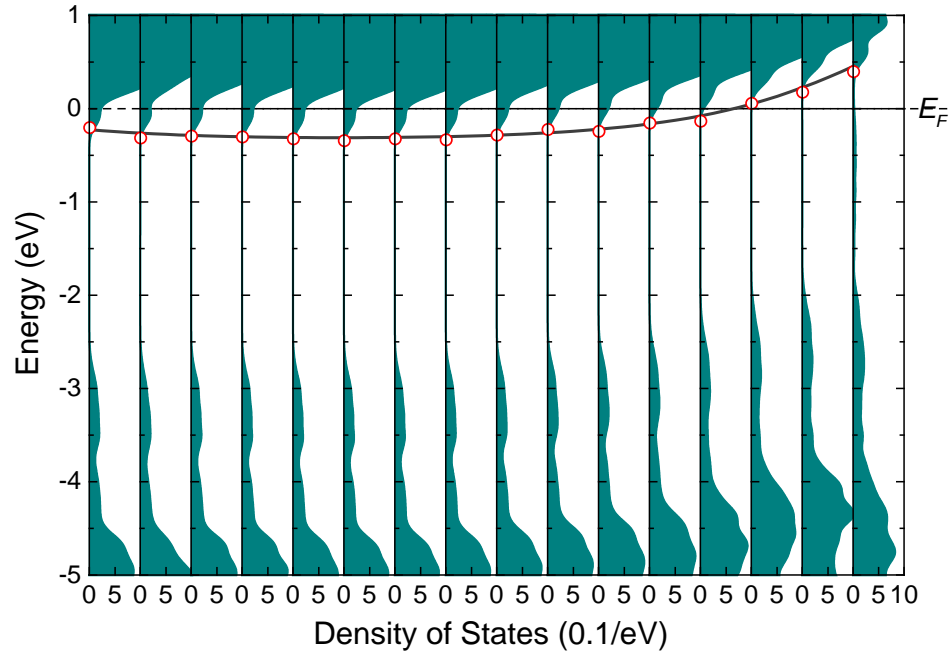
Figure 4.3 Layer-resolved density of states (DOS) on the 3d-Ti orbital across n-BaTiO$_3$

(filled curves). Open circles show the conduction band minimum (CBM) obtained as

described in the text. The solid curve shows the calculated CBM from the electrostatic

model.

The major features of the conduction band minimum (Figure 4.3) and polarization

(Figure 4.2) profiles of n-BTO can be captured by a continuum electrostatic model, as

described in the Section 4.4. The effects of the SrRuO$_3$ electrodes are incorporated by

interfacial boundary conditions on the n-BTO layer assuming (i) a linearized Thomas-

Fermi screening length λ and relative dielectric constant ε for $SrRuO_3$ and (*ii*) an electrostatic potential step going from *n*-BTO to $SrRuO_3$, ΔV, representing the built-in interface dipole, assumed to be the same at both interfaces. The polarization is modeled in the linear response regime, $P(x) = \chi \varepsilon_0 E(x) + P_0$, where P_0 is the polarization of bulk *n*-BTO in the absence of applied fields and χ is the linear dielectric susceptibility of the ferroelectric in response to the local electric field $E(x)$. The local electron density in *n*-BTO, $n(x)$, is determined self-consistently with the potential by incorporating the local density of states of the conduction band, which is taken from calculations of bulk *n*-BTO, only shifted by the local potential, $-e\varphi(x)$.

We solve the Poisson equation numerically and fit the results to the CBM profile in Figure 4.3 using λ, ε, ΔV, χ and P_0 as adjustable parameters. The resulting profile for the polarization and CBM are plotted alongside the first-principles results in Figures 4.2 and 4.3, respectively, with $\lambda/\varepsilon = 0.16$ Å, $\Delta V = 0.8$ V, $\chi = 55$ and $P_0 = 32$ $\mu C/cm^2$ providing the best fit.

Next, we explore the electronic structure of *n*-$BaTiO_3$ in the supercell as a function of transverse wave vector $\mathbf{k}_\parallel$. In Figure 4.4 we plot the $\mathbf{k}_\parallel$-resolved DOS at the Fermi energy for each TiO_2 atomic layer in *n*-$BaTiO_3$. Here we number the TiO_2 layers from 1 to 16 with layer 1 located at the left interface and layer 16 located at the right interface.

The Fermi surface of bulk *n*-$BaTiO_3$ is an open tube oriented along the *z* direction, with a *z*-dependent modulation of the radius (see Figure 4.5). The projection of the bulk Fermi surface on the *x*-*y* plane is a slightly distorted ring, as shown in Figure 4.5(b) and
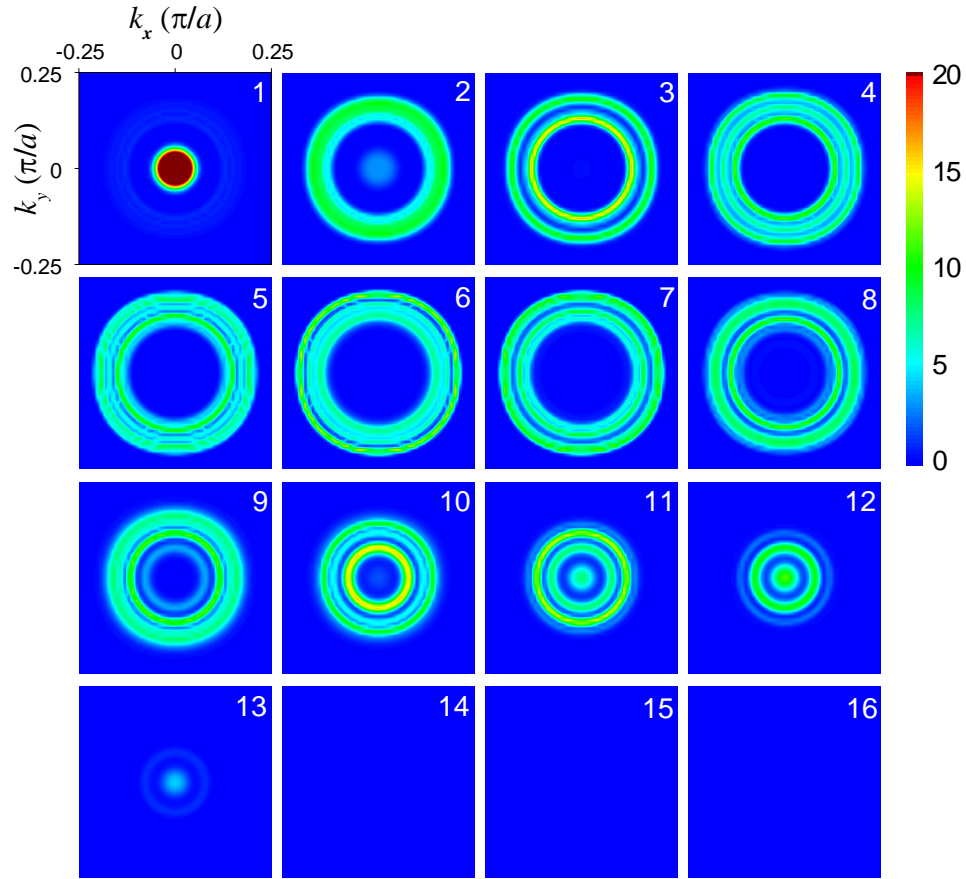
Figure 4.4 $k_\parallel$-resolved local density of states in the SrRuO$_3$/n-BaTiO$_3$ heterostructure, calculated at the Fermi energy for each atomic TiO$_2$ layer, numbered from the left to right interfaces corresponding to Figure 4.2.

4.6(a), whose inner and outer radii indicate the minimal and maximal radius of the tube. When n-BaTiO$_3$ is placed between SrRuO$_3$ layers its Fermi surface changes. Comparing Figure 4.4 to the $\mathbf{k}_\parallel$-resolved DOS for bulk n-BaTiO$_3$ [Figure 4.6(a)], we see that in the middle of the supercell, e.g. for layer 7 in Figure 4.4, the $\mathbf{k}_\parallel$-resolved DOS appears as a ring similar to that for bulk n-BaTiO$_3$. Closer to the left interface the ring is slightly

distorted, but qualitatively it remains similar to the bulk one. This is due to the layer-dependent CBM remaining nearly flat at the left interface, as is evident from Figure 4.3. Only for interfacial layer 1 in Figure 4.4 we see a significant change in the $\mathbf{k}_\parallel$-resolved DOS which appears a disk at the $\bar{\Gamma}$ point. This feature is due to the up bending of the n-BaTiO$_3$ band for this interface layer (see Figure 4.3) and electron density induced by the adjacent SrRuO$_3$. Thus, for polarization pointing to the SrRuO$_3$ metal layer, the contact is nearly-metallic (Ohmic) and we expect an efficient transmission across it.[*]
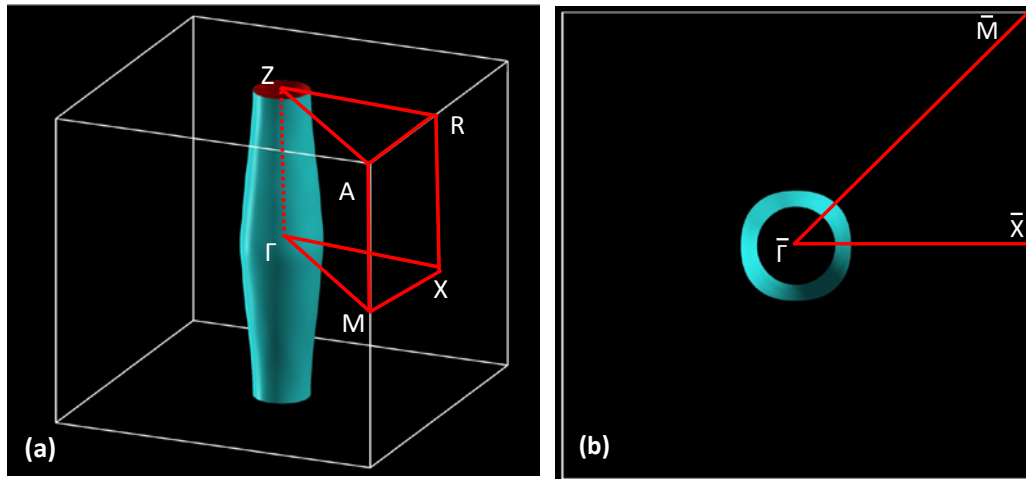
Figure 4.5 (a) The Fermi surface of bulk n-BaTiO$_3$ with $n = 0.06$ e/f.u. Polarization and transport is along z. (b) View of the Fermi surface along z showing the origin of the ring-like distribution seen in Figures 4.4 and 4.7.

This behavior changes dramatically for the right interface. The upward bending of the conduction bands seen in Figure 4.3 corresponds to a shrinking Fermi surface, as

[*] We note a mismatch of the $\mathbf{k}_\parallel$-resolved DOS between this interfacial layer and bulk n-BaTiO$_3$ which creates a barrier for ballistically transmitted electrons. In practice, however, diffuse scattering will likely make this contact Ohmic.

reflected in the reduced radius of the ring in the $\mathbf{k}_\parallel$-resolved DOS (layers 9-12 in Figure

4.4) and the transformation of Fermi surface from an open tube to a closed ellipsoid

(states appear at $\bar{\Gamma}$). The ring disappears at the third TiO_2 monolayer from the interface

and the $\mathbf{k}_\parallel$-resolved DOS shows nil for layers 14-16. This is due to the CBM bending

above the Fermi level. These three monolayers near the interface exhibit a gap for

electron transport. Thus, for polarization pointing away from the $SrRuO_3$ metal layer, the

contact is of Schottky type and we expect a reduced transmission across it.

4.3.2   Electronic transport

To confirm our expectations regarding the electronic transport, we study the transmission

across the $SrRuO_3$/n-$BaTiO_3$ (001) interface for two polarization orientations. The

transmission is calculated using a general scattering formalism implemented in the

QUANTUM ESPRESSO [91]. In the calculation we use the left interface and the right

interface in the supercell (Figure 4.2) as separate scattering regions, each of which is

ideally attached on one side to a semi-infinite $SrRuO_3$ electrode and on the other side to a

semi-infinite n-$BaTiO_3$ electrode. These geometries correspond to the same $SrRuO_3$/n-

$BaTiO_3$ junction with polarizations pointing in the opposite directions as shown in Figure

4.6. We assume perfect periodicity in the plane parallel to the interfaces so that the in-

plane component of the Bloch wave vector, $\mathbf{k}_\parallel$, is preserved for all single-electron states.

Figures 4.7(c) and 4.7(d) show the calculated $\mathbf{k}_\parallel$-resolved transmission for

polarization pointing to the $SrRuO_3$ and away from the $SrRuO_3$ respectively. The plots

are limited to the region near the $\bar{\Gamma}$ point where the transmission is non-zero. This region

is sampled using a uniform 51×51 $\mathbf{k}_{\parallel}$ mesh. The transmission distribution in the two-dimensional Brillouin zone has a similar shape for the two polarization orientations. It originates from the overlap of the Fermi surface projections of bulk n-BaTiO$_3$ and SrRuO$_3$ shown in Figures 4.7(a) and 4.7(b), respectively. The striking feature is a huge difference in the transmission magnitude for two polarization orientations. We find that polarization switching leads to a change of five orders in magnitude of transmission. The associated interface resistances are 5.5×10^2 $\Omega\mu m^2$ for the Ohmic contact and 3.78×10^7 $\Omega\mu m^2$ for the Schottky contact [105].
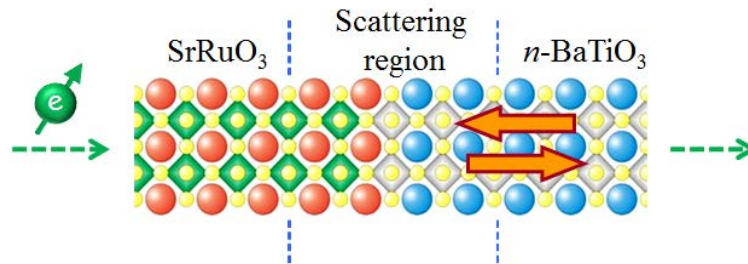
Figure 4.6 The schematic of scattering regions of transport calculations.

One of most important considerations in the study of transport phenomena across epitaxial interfaces is the matching of Fermi surfaces. The ferroelectric displacements in n-BaTiO$_3$ lead to an interesting Fermi surface due to the breaking of cubic symmetry. In cubic (i.e. non-polar) BaTiO$_3$, the conduction band consists mainly of Ti d-states which are split by the octahedral crystal field of the oxygen cage into an upper doublet of e_g
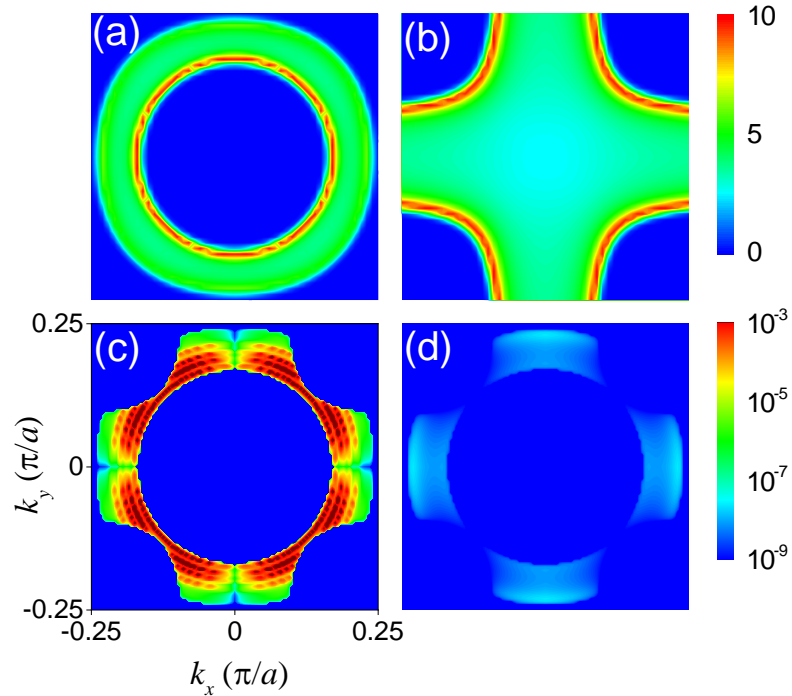
Figure 4.7 $k_\parallel$-resolved density of states at the Fermi energy in bulk n-BaTiO$_3$ (a) and

SrRuO$_3$ (b) and ballistic transmission across the SrRuO$_3$/n-BaTiO$_3$ junction with

polarization pointing to the SrRuO$_3$ – Ohmic contact (c), and polarization pointing away

from the SrRuO$_3$ – Schottky contact (d).

states and a lower triplet of t_{2g} states. The latter form the states around the conduction

band minimum. The onset of polarization (i.e., off-centering of the Ti ions) leads to a

splitting of the t_{2g} states into an upper doublet of d_{zx} and d_{zy} and a lower singlet of d_{xy}.

Therefore, when electron-doped, the free carries fill states of primarily d_{xy} character.

States with d_{xy} character are essentially two-dimensional, with stronger coupling in the x-

y plane than along the polarization axis, z. This gives rise to large band-dispersion in the

plane and weak dispersion out of the plane, leading to the tube-like Fermi surface, shown

in Figure 4.5, for $n = 0.06$ *e*/f.u and the ring-like distributions shown in Figures. 4.4 and 4.7.
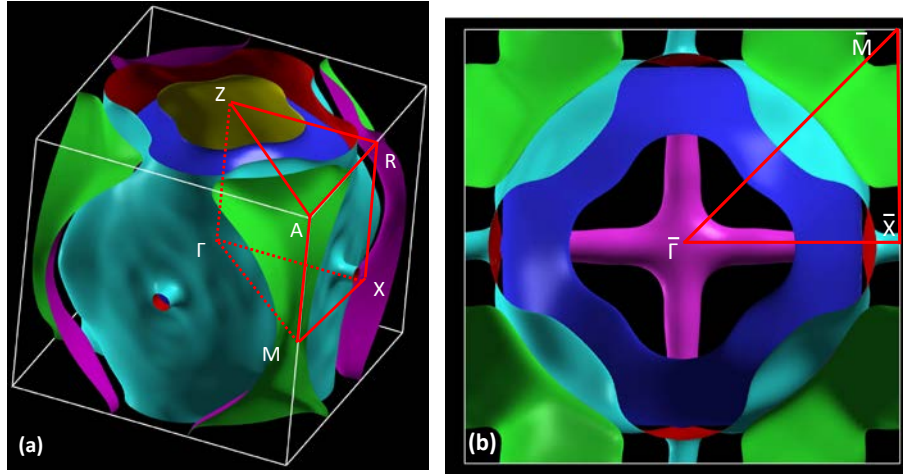
Figure 4.8 (a) The Fermi surface of bulk $SrRuO_3$ strained in the *x-y* plane with $c/a = 1.03$, corresponding to epitaxy with an $SrTiO_3$ substrate. (b) View of the Fermi surface along *z* showing the origin of the cross-like distribution seen in Figure 4.7(b).

The Fermi surface of bulk $SrRuO_3$, plotted in Figure 4.8, is significantly more complicated. Given the relatively limited span of the Fermi surface of *n*-$BaTiO_3$ (Figure 4.5(b)), however, the relevant features of the $SrRuO_3$ Fermi surface are limited to the cross-like region in the small range around the $\bar{\Gamma}$ point (see Figure 4.8(b)). The projection of these states onto the *x-y* plane give rise to the cross features shown in Figure 4.7(b), and their overlap with the Fermi surface of *n*-$BaTiO_3$ determine the shape of the transmission distributions in Figure 4.7(c-d). The tetragonal structure arising from the epitaxial strain gives rise to the opening of several Fermi sheets along the *z* direction.

4.4   Electrostatic model

We now consider a layer of n-BTO from $x = 0$ to L bounded on the left and right by

metallic SrRuO$_3$ electrodes held in short-circuit boundary conditions. The electrodes

were modeled by Thomas-Fermi screening length λ and relative dielectric constant ε, and

therefore the potential follows the typical form

$$\varphi_l\left(x\right) = A_l e^{x/\lambda}, \ \varphi_r\left(x\right) = A_r e^{-(x-L)/\lambda} \tag{1}$$

The potential inside the n-BTO, $\varphi(x)$, must satisfy the Poisson equation

$$\frac{\partial^2 \varphi}{\partial x^2} = -\frac{e\left(n_0 - n(x)\right)}{\left(\chi + 1\right)\varepsilon_0} \tag{2}$$

where the first term on the right hand side corresponds to the uniform background density

of n-type dopants, $n_0 = 0.06/ca^2$, and the second term corresponds to the occupied states

in the conduction band.

The local carrier density, $n(x)$, is assumed to depend on x only through the local

potential $\varphi(x)$ and the local density of states of the conduction band, $N(E + e\varphi(x))$, where

$$N\left(E\right) = \begin{cases} 0 & E < E_c^0 \\ N_0 & E > E_c^0 \end{cases} \tag{3}$$

N_0 is a constant which is determined by the nominal carrier concentration in the bulk, n_0,

and the position of the CBM with respect to the Fermi level, E_F, calculated in bulk n-

BTO from first-principles: $E_c^0 = -0.33$ eV. Therefore the average density of states is $N_0 =$

$n_0/|E_c^0|$ and the local carrier concentration is

$$n\left(x\right) = \left(E_F - E_c^0 + e\varphi\left(x\right)\right) \begin{cases} 0 & E_c^0 - e\varphi\left(x\right) > E_F \\ N_0 & E_c^0 - e\varphi\left(x\right) < E_F \end{cases} \tag{4}$$

Eq. (2) is subject to boundary conditions which connect $\varphi(x)$ to Eqs. (1) at $x = 0$ and L. A_l and A_r can be eliminated from these boundary conditions and the following conditions on $\varphi(x)$ emerge:

$$\varphi(0) + \Delta V + \frac{\lambda}{\varepsilon}\left[(\chi+1)E(0) + \frac{P_0}{\varepsilon_0} \right] = 0$$

$$\varphi(L) + \Delta V - \frac{\lambda}{\varepsilon}\left[(\chi+1)E(L) + \frac{P_0}{\varepsilon_0} \right] = 0,$$

(5)

where $E(x)$ is the electric field in the n-BTO. Note that the electrodes enter the boundary conditions only through the ratio λ/ε. Equation (2) is solved numerically subject to the boundary conditions in (5), and the CBM is related to the potential as $CBM = E_c^0 - e\varphi(x)$.
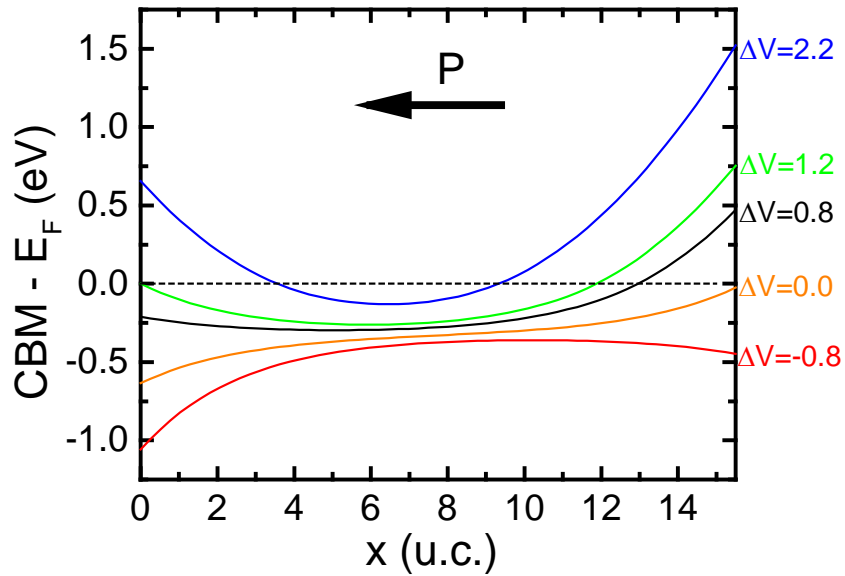
Figure 4.9 Profile of the CBM for various interface dipoles, ΔV (in eV), but using the same best fit values found for the other parameters of the model.

It is well known that the band gap calculated in density functional theory, especially in LDA, is underestimated (sometimes drastically) as compared to experiment. Therefore attempts to determine band offsets from first-principles calculations must be approached with care. In LDA we find a band gap of $E_g{}^{LDA}$ = 1.8 eV for BaTiO$_3$, whereas in experiment it is known that $E_g{}^{expt}$ = 3.2 eV. While little can be done for the LDA calculations to account for this issue, in our model we can make adjustments to correct for the band gap problem.

The simplest correction we can make is to assume that, all else being equal, the CBM must lie higher in energy than what is predicted by LDA by a fixed difference ΔE_g = $E_g{}^{expt}$ - $E_g{}^{LDA}$ = 1.4 eV. This correction enters our model in the interface dipole parameter, ΔV. In our best fit to the LDA results we found ΔV = 0.8 V, and therefore corrections for the band gap will increase this value possibly up to 0.8 V + 1.4 V = 2.2 V. In Figure 4.9 we plot the CBM profile across the junction for several values of ΔV, with all other parameters of the model held fixed at those of the best fit to the LDA data.

Comparing the left and right interfaces, we see that for ΔV > 1.2 V that there is a crossover from Ohmic to Schottky transition with polarization reversal to the interface always being of Schottky type, but with a significant difference between Schottky barrier height (SBH) and width (w) depending on the polarization orientation. These differences are further clarified in Figure 4.10 where we plot the dependence of the interface barrier on ΔV for both polarization orientations. It is clear that the change in SBH with polarization reversal is roughly constant over a broad range of ΔV, and even increases for larger ΔV. Therefore we expect that our prediction of a significant change in interface

resistance with polarization reversal is quite robust and independent of the deficiencies of LDA to properly predict band alignments.
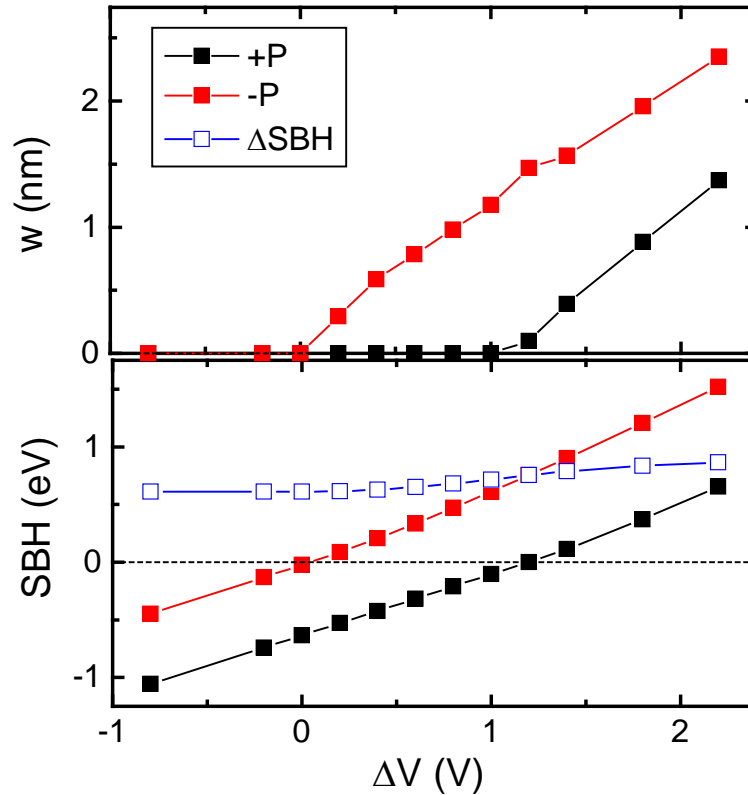
Figure 4.10 Dependence of the Schottky barrier width (*w*) and height (SBH) on the interface dipole, ΔV, for the two polarization orientations. We use the same values found for the best fit to the LDA results for the other parameters. Negative values of SBH correspond to an Ohmic contact, where $w = 0$.

4.5   Conclusions

We have shown that the polarization driven accumulation or depletion of free carriers at the $SrRuO_3/n$-$BaTiO_3$ (001) interface alters the transport regime across the interface from

metallic to tunneling. We find that polarization switching leads to a five orders of magnitude change in the interface resistance. We hope that the predicted polarization controlled Ohmic to Schottky transition at the metallic oxide/doped ferroelectric interface will stimulate experimental investigations.

Chapter 5 *Ferroelectrically controlled spin polarization*

Spin injection is one of the key phenomena exploiting the electron spin degree of freedom in electronic devices [106]. A critical parameter that determines the efficiency of spin-injection is the degree of spin polarization carried by the current. Efficient spin injection into metals has been commercially employed in today's magnetic read heads and magnetic random access memories through the tunneling magnetoresistance effect in magnetic tunnel junctions. There is considerable current interest in the area of spin injection into semiconductors [107, 108, 109, 110, 111, 112]. Recent developments in the field have demonstrated the possibility of efficient spin-injection and spin-detection in various electronic systems [113, 114]. All the above results rely however on a "passive" spin injection where the degree of transport spin polarization is determined by the spin polarization of the injector and the detector, and the electronic properties of the interface. Adjustable spin injection with a controllable degree of spin polarization would be appealing from the scientific point of view and useful for applications in future spintronic devices.

Electric-field control of spin-dependent properties has become one of the most attractive phenomena in modern materials research due to the promise of new device functionalities. One of the paradigms in this approach is to electrically toggle the spin polarization of carriers injected into a semiconductor using ferroelectric polarization as a control parameter. Using first-principles density functional calculations, we explore the effect of ferroelectric polarization of electron-doped $BaTiO_3$ (n-$BaTiO_3$) on the spin-polarized transmission across the $SrRuO_3$/n-$BaTiO_3$ (001) interface. Our study reveals

that, in this system, the interface transmission is negatively spin-polarized and that ferroelectric polarization reversal leads to a change in the transport spin polarization from -65% to -98%. We show that this effect stems from the large difference in Fermi wave vectors between up- and down-spins in ferromagnetic $SrRuO_3$ and a change in the transport regime driven by ferroelectric polarization switching in $n\text{-}BaTiO_3$. Analytical model calculations demonstrate that this is a general effect for ferromagnetic-metal/ferroelectric-semiconductor systems and, furthermore, that ferroelectric modulation can even reverse the sign of spin-polarization. The predicted sizeable change in the spin polarization provides a non-volatile mechanism to electrically control spin injection in semiconductor-based spintronics devices.

5.1   Spin dependent tunneling

The study of spin-dependent tunneling started with the experiment of Tedrow and Meservey [115, 116]. They studied a ferroemagnet/insulator/superconductor junction, where the superconductor performs as a detector. The tunneling spin polarization is defined as:

$$P = \frac{G_\uparrow - G_\downarrow}{G_\uparrow + G_\downarrow} \tag{1}$$

where, $G_\uparrow$ and $G_\downarrow$ are conductance of majority- and minority- spin respectively. In this experiment, P is determined by measuring the resistivity of majority- and minority-spin.

First, the tunneling spin polarization was interpreted in terms of the spin polarization of the density of state (DOS) of the ferromagnet at the Fermi energy based

on the assumption that spin conductance is proportional to DOS $\rho^\uparrow$ for the majority-spin

electrons and is proportional to DOS $\rho^\downarrow$ for the minority-spin electrons,

$$P_{FM} = \frac{\rho^\uparrow - \rho^\downarrow}{\rho^\uparrow + \rho^\downarrow} \ . \tag{2}$$

However, the predicted value of spin polarization P_{FM} based on Eq. 2 and

measured spin polarization P are not consistent with each other. Even in some cases, the

predicted P_{FM} is negative while the measured P is positive [117].

Later, Stearns noticed that the electronic structure of a ferromagnet plays an

important role in spin polarization [118]. A model given by Stearns took into account the

bands structure of the ferromagnet. This model assumes that only itinerant electrons of

dispersive bands dominate the tunneling. The DOS of the dispersive bands at the Fermi

level is proportional to their Fermi wavevectors as in the case of a free electron model.

Then the spin polarization is given by

$$P_{FM} = \frac{k^\uparrow - k^\downarrow}{k^\uparrow + k^\downarrow} \tag{3}$$

Where $k^\uparrow$ and $k^\downarrow$ are the Fermi wavevectors of the dispersive bands for the majority and

minority spins.

This model has also its inconsistency, since conductance not only depends on

DOS but also on tunneling probability. Based on tunneling effect in quantum mechanics,

the transmission is not a linear function of the wavevector. Therefore, the conductance is

not proportional to the wavevector or the density of states at the Fermi energy.

A more accurate theoretical description of the transport spin polarization is given by Slonczewski, where the effect of tunneling barrier is taken into account [119]. In a free-electron approximation, for a system with two ferromagnetic conductors separated by nonmagnetic tunneling barrier, he solved the Schrödinger equation and determined the spin polarization as:

$$P = \frac{k^{\uparrow} - k^{\downarrow}}{k^{\uparrow} + k^{\downarrow}} \frac{\kappa^2 - k^{\uparrow}k^{\downarrow}}{\kappa^2 + k^{\uparrow}k^{\downarrow}} \tag{4}$$

Where κ is the decay constant of the wave function into the barrier which is determined by the potential barrier height U, $\kappa = \sqrt{(2m/\hbar^2)(U - E_F)}$.
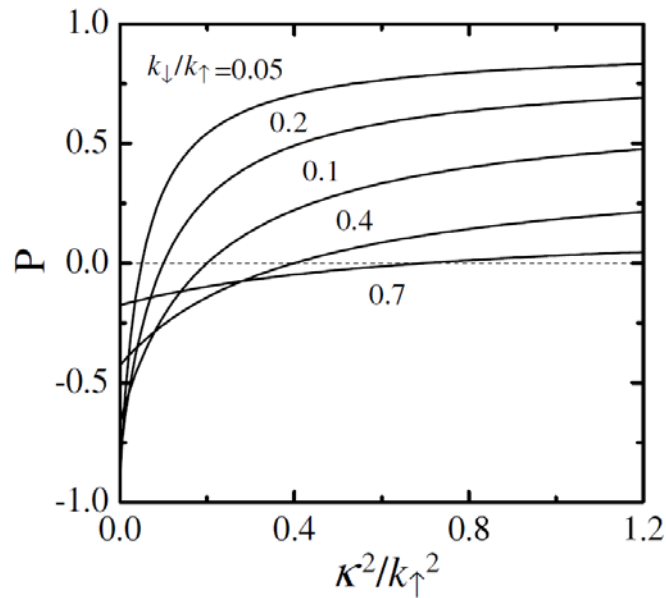
Figure 5.1 Spin polarization of the tunneling conductance as a function of the normalized potential barrier height for various values of $k\uparrow/k\downarrow$. From ref. [119]

Here, it is clear that the spin polarization is not an intrinsic property of

ferromagnet but is influenced by the whole system including the barrier. In the case of a

high barrier, κ is large, and the Slonczewski model reduces to Stearns' model. However,

when the barrier is not very high, the effect of the barrier must be taken into account spin.

From Figure 5.1 we can see the dependence of spin polarization on barrier height. The

magnitude of the spin polarization even changes sign for low barrier.

As we showed in chapter 4, reversal of ferroelectric polarization results in

dramatic change of the Schottky barrier of a ferromagnetic/n-ferroelectric heterojunction.

Based on Slonczewski model, we will show in this chapter that the reversal of

ferroelectric polarization dependent Schottky barrier leads to a dramatic change of spin

polarization and even changes the sign.

5.2   Spin injection into semiconductor

Spin injection is an important method to generate nonequilibrium spin polarization [120].

There are two basic methods used today for spin injection: optical spin injection and

electrical spin injection. Here we give brief introduction of the electrical method for spin

injection

The current through an interface of a heterojunction is a diffusive process and

could be described by a diffusion equation:

$$(\mu_\uparrow - \mu_\downarrow)/\tau_{sf} = D\partial^2(\mu_\uparrow - \mu_\downarrow)/\partial x^2 \qquad (5)$$

where τ_{sf} is the spin flip time constant and D is the diffusion constant determined by

Fermi velocity and electron mean free path. Near the interface, a splitting of the

electrochemical potentials is created for the two spin directions, and this splitting decays

exponentially away from the interface, as is shown in Figure 5.2 [121, 122].
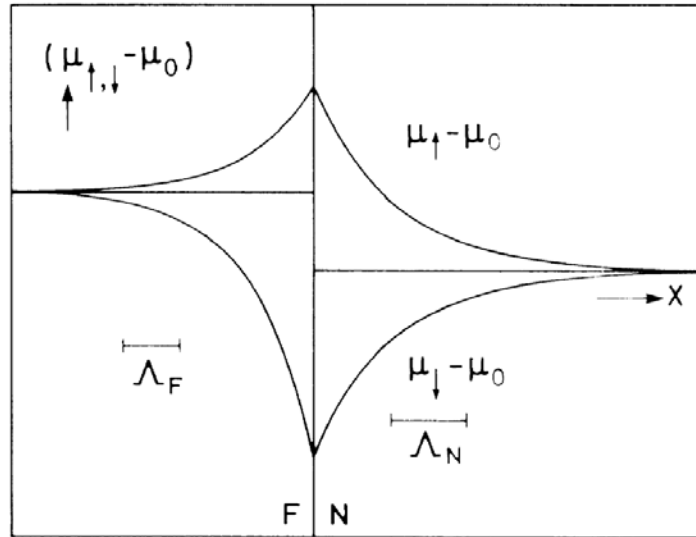
Figure 5.2 Position dependence of the potential differences $\mu_\uparrow - \mu_0$ and $\mu_\downarrow - \mu_0$ near an

F/N interface. $\Lambda_{F,N}$ is spin-flip diffusion length. From ref. [121]

When current flows from a ferromagnet into a normal metal, the spin-polarized

carriers in the ferromagnet (F) contribute to the net current of magnetization entering the

nonmagnetic (N) region and would lead to nonequilibrium magnetization δM which has

a linear correlation with the difference of chemical potential of spin-up and spin-down:

$$e(\mu_\uparrow - \mu_\downarrow) = \mu_B \delta M / \chi, \tag{6}$$

Here e is the electron charge, μ_B is the Bohr magneton and χ is magnetic susceptibility.

The detection of δM could be realized in a F1/N/F2 system. δM in N region results in a

spin-coupled voltage, ΔV, between N and F2, which is proportional to δM, and

therefore the nonequilibrium magnetization could be measured experimentally by measuring ΔV [123, 124, 125]. Due to the spin relaxation, δM decreases from the interface into the nonmagnetic region which is characterized by the spin diffusion length as show in Figure 5.3.
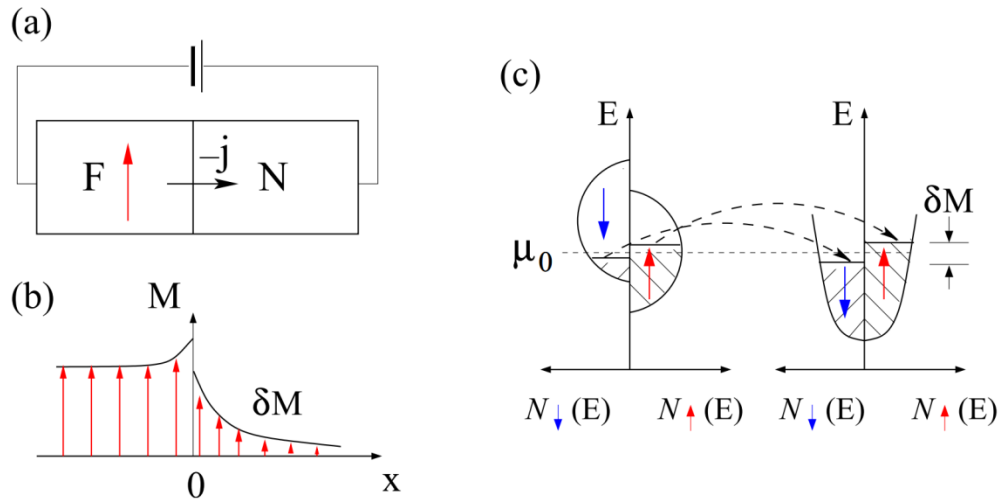
Figure 5.3 Schematic illustrations of the concept of electrical spin injection from a ferromagnet (F) into a normal metal (N). (a) schematic device geometry; (b) magnetization M as a function of position—nonequilibrium magnetization δM (spin accumulation) is injected into a normal metal; (c) contribution of different spin-resolved densities of states to both charge and spin transport across the F/N interface. The unequal filled levels in the density of states depict spin-resolved electrochemical potentials different from the equilibrium value μ_0. From ref. [120]

The efficiency of spin injection is affected strongly by the interface. The spin-polarization of the injected current is given by [126, 127]

$$P = \frac{R_C p_C + R_F p_F}{R_c + R_F + R_N} \tag{7}$$

where $p_C = \frac{\sigma_C^\uparrow - \sigma_C^\downarrow}{\sigma_C^\uparrow + \sigma_C^\downarrow}$, $p_F = \frac{\sigma_F^\uparrow - \sigma_F^\downarrow}{\sigma_F^\uparrow + \sigma_F^\downarrow}$. Here, $\sigma_C^\uparrow$ and $\sigma_C^\downarrow$ are the interface conductivity for

majority- and minority- spin respectively. $\sigma_F^\uparrow$ and $\sigma_F^\downarrow$ are the bulk conductivity of

ferromagnetic region for majority- and minority- spin respectively. R_c, R_F and R_N are

effective resistance of interface, ferromagnetic and non-ferromagnetic region respectively.

The resistance of semiconductor is quite a bit bigger than the resistance of metal

ferromagnet $R_N \gg R_F$. When the contact regime of interface is Ohmic, i.e. $R_c = 0$,

$P \approx \frac{R_F}{R_c} \ll 1$. Therefore Ohmic contact is an obstacle for spin injection into the

semiconductor due the conductance mismatch of ferromagnet and semiconductor. When

$R_c \gg R_F$, the injected spin polarization is dominated by the effect of the interface,

$P \approx p_C$ [122]. From the definition, we know that p_C is determined by wavevector and

transmission coefficients of majority- and minority-spin electrons. p_C in fact is given by

Slonczewski's model. The interface effect implies that introduction of tunneling barrier

or Schottky contact is an effective method for spin injection [128].

5.3   Electric control of spin injection into a ferroelectric semiconductor

Recently, experiment and theory have found that ferroelectric polarization can be used to

control magnetization at all-oxide ferroelectric/ferromagnetic interfaces [24, 25]. Studies

in such oxide systems reveal that proper engineering of the interface plays a crucial rule

in the manifestation of such novel phenomena [129]. Reversal of ferroelectric

polarization provides a bistable mechanism to electrically control electronic systems and

this characteristic can be used to design novel electronic devices. Efforts have been made

in this field, and an important route taken is where ferroelectric materials are introduced

as functional barriers in tunnel junctions [130], providing a possibility to strongly affect

the resistance of such a ferroelectric tunnel junction (FTJ) by ferroelectric polarization

switching. This functionality of FTJs is extended by employing ferromagnetic electrodes,

as follows from the theoretical predictions [99, 131, 132] and a number of experimental

demonstrations [133, 134, 135, 136] of tunable spin-polarized tunneling current.

While ferroelectric materials used in FTJs are normally considered as insulators,

previous studies have found that ferroelectricity persists even in moderately electron-

doped (i.e. metallic, or nearly so) $BaTiO_3$ [38, 79]. These results were corroborated by

theoretical studies showing that ferroelectric displacements in $BaTiO_3$ persist up to a

doping level of about $0.1e$ per unit cell ($\sim10^{21}/cm^3$) [137, 138]. The combination of

ferroelectricity and conductivity in one material introduces unique electronic properties,

opening the door to extended functionalities. In Chapter 4 we have shown that the

ferroelectric polarization can be used to alter the resistive nature of the interface between

n-$BaTiO_3$ and metallic $SrRuO_3$. Specifically, we found that polarization switching in n-

$BaTiO_3$ induces a transition between Ohmic and Schottky regimes, leading to a five-

orders-of-magnitude change in interface resistance.
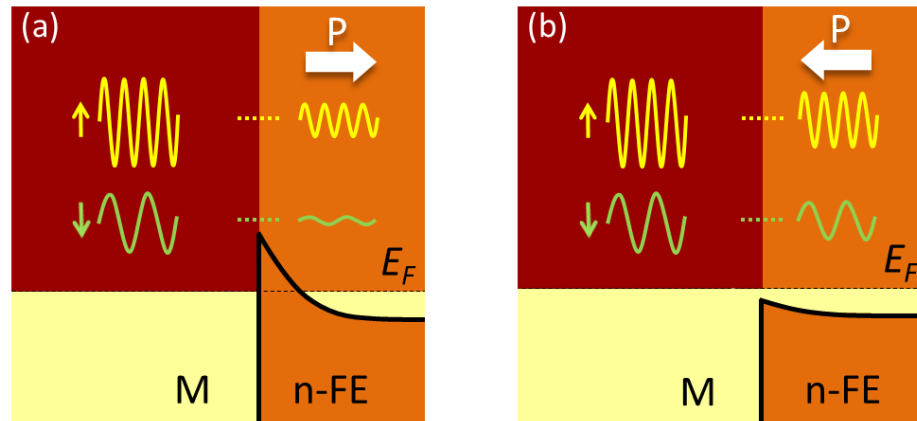
Figure 5.4 Polarization controlled band alignment and spin-polarization in the interface between a ferromagnetic metal (FM), e.g. $SrRuO_3$, and electron-doped ferroelectric (*n*-FE), e.g. *n*-$BaTiO_3$. Horizontal arrows indicate the ferroelectric polarization direction. Light shaded areas correspond to occupied states and dark shaded areas correspond to unoccupied states. Schottky (a) and Ohmic (b) contacts are created for polarization pointing away from and into the interface, respectively. Waves depict incident and transmitted Bloch states for spin-up and spin-down electrons.

In this chapter, we demonstrate that ferroelectric polarization can be used as a control parameter to tune the spin-polarization of injected carries from a ferromagnetic (FM) metal into an electron-doped ferroelectric (*n*-FE). As a model system we use a $SrRuO_3$/*n*-$BaTiO_3$ (001) junction, where we take into account the spin-polarized electronic band structure of $SrRuO_3$. Since $SrRuO_3$ is ferromagnetic below the Curie temperature of 160K [139], the transmission across such an interface is spin-polarized and the magnitude of this spin-polarization is expected to depend on the orientation of the ferroelectric polarization, as is indicated schematically in Figure 5.4. Our calculations

confirm this expectation, predicting a significant change in the transport spin-polarization,

which is the central result of this work. Such an effect provides a robust mechanism to

realize, for example, multistate magnetoelectric data operation on a single device

component.

5.3.1   Ferroelectric polarization dependent spin polarization

First-principles calculations are performed using the plane-wave pseudopotential code

QUANTUM ESPRESSO [91], where exchange and correlation effects are treated within

the local spin-density approximation. The electron wave functions are expanded in a

plane-wave basis set limited by a cut-off energy of 550eV. Periodic boundary conditions

are used on a supercell constructed of 15.5 unit cells (u.c.) of n-$BaTiO_3$ and 10.5 u.c. of

$SrRuO_3$. To simulate coherent epitaxial growth on a $SrTiO_3$ (001) substrate, we constrain

the in-plane lattice constant of the supercell to be the calculated LDA lattice constant of

cubic $SrTiO_3$, $a = 3.871$ Å. The supercell is constructed by stacking these structural unit

cells along the [001] direction (z direction) assuming the SrO/TiO_2 termination on both

interfaces. The electron doping of n-$BaTiO_3$ is assumed to be $0.06e$ per formula unit,

which is realized by the virtual crystal approximation [104] applied to the oxygen

potentials in $BaTiO_3$. Full internal relaxations of the atomic positions and the overall c/a

ratio of the supercell are carried out with no spin-polarization taken into account until the

Hellmann-Feynman force on each atom becomes less than 10 meV/Å. Then, self-

consistent spin-polarized calculations are performed to converge the electronic structure

to 10^{-5} eV/u.c. Monkhorst-Pack k-points meshes of 6×6×1 and 12×12×1 are used for structural relaxation and electronic structure calculations, respectively.

Transport properties, i.e. the spin-dependent interface transmission, are calculated using a general scattering formalism implemented in the QUANTUM ESPRESSO. Within the supercell the polarization direction of the n-BaTiO3 is uniform throughout, pointing away from the right interface toward the left interface. In the transport calculation, therefore, we treat the left and right interfaces in the supercell as separate scattering regions, each ideally attached on one side to a semi-infinite $SrRuO_3$ electrode and on the other side to a semi-infinite n-$BaTiO_3$ electrode. These transport geometries correspond to the same $SrRuO_3$/n-$BaTiO_3$ junction with polarizations pointing in the opposite directions. We assume perfect periodicity in the plane parallel to the interfaces so that the in-plane component of the Bloch wave vector, $\mathbf{k}_\parallel$, is preserved for all single-electron states. The transmission calculations are performed over the entire two-dimensional Brillouin zone (2DBZ), sampled using a uniform 100×100 $\mathbf{k}_\parallel$ mesh.

Consistent with the result shown in Chapter 4 for the non-spin polarization calculation, we find that reversal of ferroelectric polarization of n-$BaTiO_3$ results in a transition between two contact regimes: Schottky and Ohmic. We find, however, that taking into account the spin-polarized band structure of $SrRuO_3$ leads to a smaller change in the interface resistance with polarization reversal, as compared to the non-spin-polarized calculations. Specifically, we obtain a total resistance of 0.28×10^2 $\Omega\mu m^2$ for the Ohmic contact and 0.95×10^4 $\Omega\mu m^2$ for the Schottky contact, revealing about three-orders-of-magnitude change in the interface resistance. This difference between the non-

spin-polarized and spin-polarized results is due to the changes in the Fermi surface of

$SrRuO_3$. This is especially true for the spin-down transmission channel in $SrRuO_3$, which

has a larger wave vector than the non-spin-polarized Fermi surface and therefore higher

probability of tunneling across the Schottky barrier.
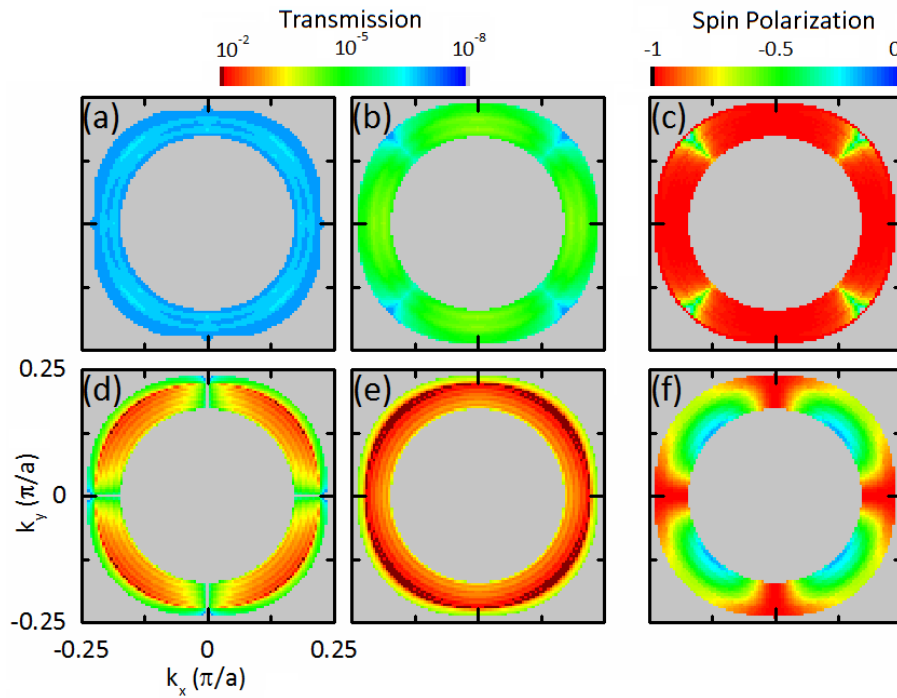
Figure 5.5 $k_{\parallel}$-resolved transmission through the Schottky interface for (a) spin-up and (b)

spin-down electrons. (c) $k_{\parallel}$-resolved spin-polarization for the Schottky interface. Note

that transmission is only plotted in a small region around $k_{\parallel} = 0$, all other points in the

2DBZ have zero transmission. (d-f) Same as in (a-c) for the Ohmic interface.

For each contact, we calculate transmission for spin-up and spin-down electrons

($T_{\uparrow}$ and $T_{\downarrow}$, respectively) over the 2DBZ. As seen in Figure 5.5, the transmission is

distributed in a ring-shaped area centered around the $\bar{\Gamma}$ point (i.e. $\mathbf{k}_\parallel = 0$). Regions of the 2DBZ with non-zero transmission occur only where the Fermi surface projections of $SrRuO_3$ and n-$BaTiO_3$ overlap, leading to the ring-like distribution. For both polarization orientations (i.e. for both interface contact regimes), the spin-down transmission is larger than that of the spin-up transmission. Figures 5.5(c) and (f) show the spin-polarization of the interface transmission, which is defined by SP = $(T_\uparrow - T_\downarrow)/(T_\uparrow + T_\downarrow)$ and calculated over the 2DBZ. It is evident that for both contact regimes, the net spin polarization is negative. When ferroelectric polarization is pointing toward the interface and the contact is Ohmic, the net spin polarization is -65%, Figure 5.5(f). When the ferroelectric polarization is switched to point away from the interface and the contact is Schottky the spin-polarization in this case is negatively enhanced to -98%, Figure 5.5(c).

To understand such a strong effect, we start from examining the Fermi surface of $SrRuO_3$ (Figure 5.6). Its projection covers nearly the entire 2DBZ, as seen from Figures 5.6(a, b) and 5.6(c, d) for spin-up and spin-down, respectively. The Fermi surface of n-$BaTiO_3$ consists of a single sheet forming a corrugated tube oriented along the electric polarization, as shown previously in Chapter 4. The overlap between the Fermi surfaces of $SrRuO_3$ and n-$BaTiO_3$, viewed along the transport direction, leads to the ring-like area approximately indicated by the concentric circles in Figure 5.6(b) and (d). Since we consider complete in-plane periodicity there is no mixing between different $\mathbf{k}_\parallel$ and, therefore, to study the spin-polarized transmission, we need only to take into account the properties of states located in this region of the Fermi surface of $SrRuO_3$. An orbital analysis of these states on the Fermi surface reveals that spin-up states are composed

mainly of the Ru d_{z^2} orbital (the yellow surface in Figures 5.6(a) and 5.6(b)), while the spin-down states are composed of Ru d_{zx} and d_{zy} orbitals (the magenta surface in Figures 5.6(c) and 5.6(d)).
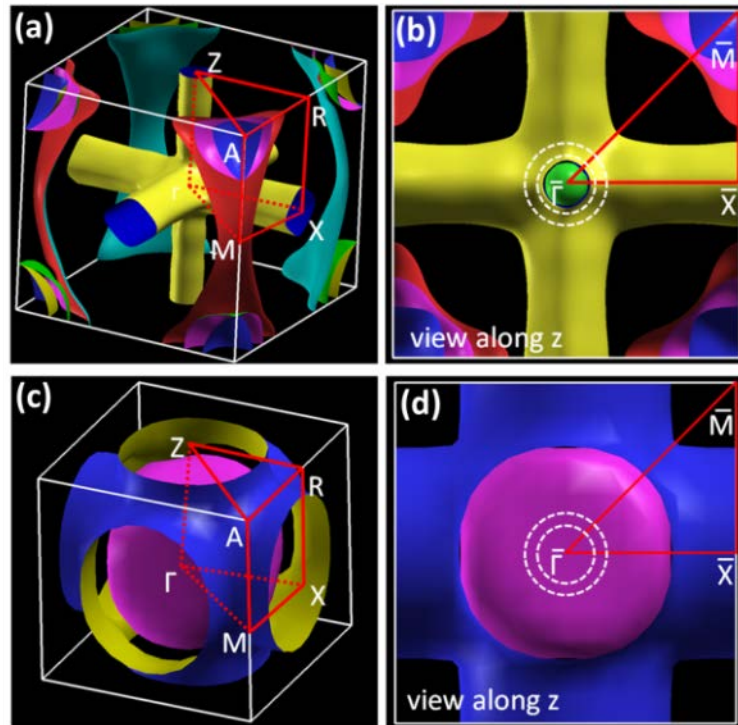
Figure 5.6 Fermi surfaces of $SrRuO_3$ for spin-up (a) and spin-down electrons (c) and their view along the z direction respectively (b) and (d). Colors are used to aid the eye in delineating different sheets, and different sides of the same sheet, of the Fermi surface. The concentric rings in (b) and (d) approximately demark the minimum and maximum radius of the Fermi surface of n-$BaTiO_3$.

The negative value of spin polarization, as found for both cases, as well as the change in spin-polarization magnitude can be understood using the arguments put forth

by Slonczewski [119]. According to the Slonczewski model, first, the spin-polarization of the transmission coefficient for a given $\mathbf{k}_\parallel$ is negative if $k_z^\downarrow / k_z^\uparrow > 1$. Second, the magnitude of the spin-polarization depends on the effective barrier height for each $\mathbf{k}_\parallel$: higher barriers lead to an enhanced spin-filtering.

The results of our calculations conform to both of these relationships. The spin-resolved Fermi surfaces of $SrRuO_3$ have quite different characteristics in the ring-like region of the 2DBZ, with $k_z^\downarrow / k_z^\uparrow \gg 1$, as seen by comparing the yellow surface for spin-up in Figure 5.6(a,b) with the magenta surface for spin-down in Figure 5.6(c,d). This behavior can be understood in terms of the orbital character of the spin-dependent states comprising the Fermi surface. The crystal field lowers the energy of the Ru t_{2g} orbitals with respect to the Ru e_g orbitals. This reduces the potential energy of the spin-down d_{zx} and d_{zy} states and, hence, enhances their kinetic energy on the Fermi surface, which is reflected in a nearly spherical Fermi surface and a larger Fermi wave vector for the spin-down states. On the contrary, the higher energy of the spin-up d_{z^2} states strongly affects the shape of the Fermi surface causing it to form a cross pattern of three corrugated tubes, leading to small values of the Fermi wave vector in the vicinity of the $\bar{\Gamma}$ point for the spin-up states.

When the ferroelectric polarization of the n-$BaTiO_3$ points into $SrRuO_3$, as shown in Figure 5.4(b), the Fermi level is located closer to the bottom of conduction bands of n-$BaTiO_3$ than it is in the bulk. This leads to the first layer of n-$BaTiO_3$ near the interface being, in fact, an effective tunneling barrier, despite the small occupation of the conduction band. When ferroelectric polarization is reversed to point away from $SrRuO_3$,

as shown in Figure 5.4(a), there is complete depletion of conduction band states near the interface (i.e. a Schottky barrier) and hence the tunneling barrier height is dramatically increased.
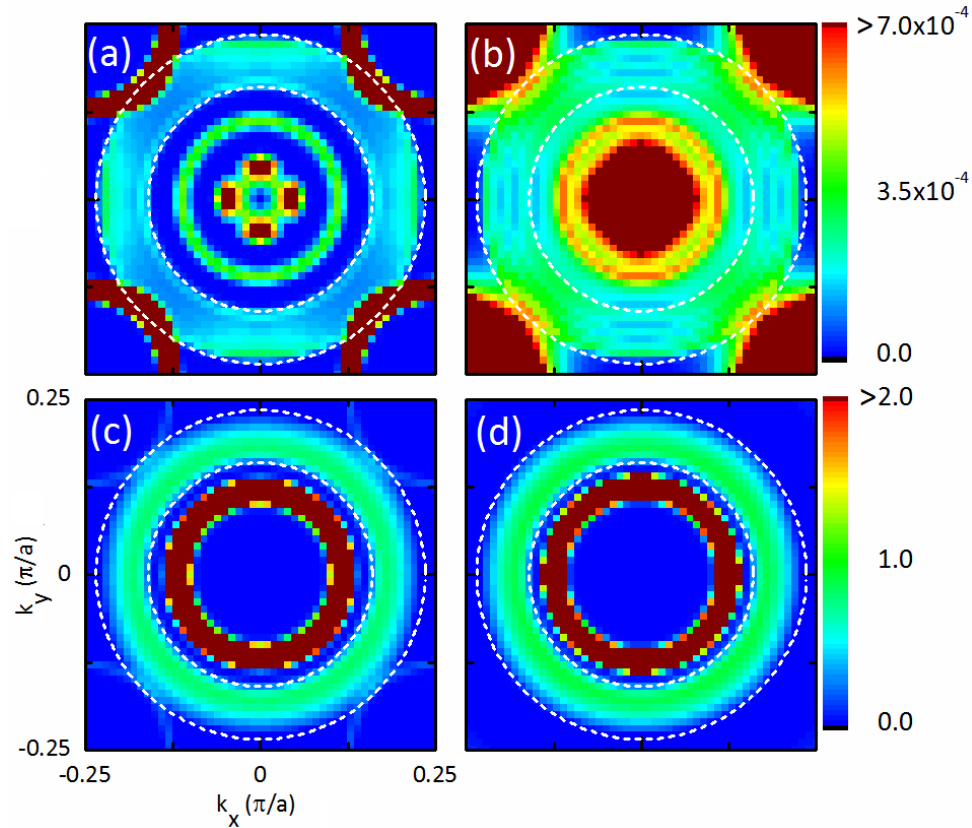
Figure 5.7 Spin-up (a, c) and spin-down (b, d) $k_\parallel$-resolved local density of states on the interfacial Ti atom for Schottky (a, b) and Ohmic (c, d) contacts.

We conclude therefore that the negative spin- polarization can be explained by the existence of a tunneling barrier at the $SrRuO_3/n\text{-}BaTiO_3$ interface and the spin-dependent Fermi surface of $SrRuO_3$ which is characterized by a larger wave vector for spin-down

electrons compared to spin-up electrons ($k_z^{\downarrow} / k_z^{\uparrow} > 1$). Furthermore, when the ferroelectric polarization is reversed from pointing into the interface to pointing away from the interface the dramatic increase in the barrier height leads to the substantial enhancement in the magnitude of the spin-polarization, consistent with the Slonczewski model.

The change in the transport spin-polarization with ferroelectric polarization reversal is also reflected by the induced local density of states within the n-BaTiO$_3$ barrier near the interface. Figure 5.7 shows the spin-polarized local density of states on the interfacial Ti atom for both contact regimes. It is seen that, within the transmission ring, the induced density of states is more negatively spin-polarized for the Schottky contact than for the Ohmic contact. This observation is consistent with our prediction of the enhanced negative spin-polarization in the Schottky contact regime.

This change in the transport spin polarization coexists with the magnetoelectric effect: a change in the interfacial magnetic moment with reversal of ferroelectric polarization. The magnetic moment on the Ru atom is 0.72 μ_B in the center of the SrRuO$_3$ layer which is reduced to 0.40 μ_B and 0.58 μ_B at the Schottky and Ohmic interfaces, respectively. Integrating the spin density across the interfaces we find that the net change in interfacial magnetic moment per unit area caused by the ferroelectric polarization reversal is $\Delta M \approx 0.35$ μ_B/a^2, which is nearly the same as that found for an undoped SrRuO$_3$/BaTiO$_3$ system [25].

The predicted ferroelectrically-tunable transport spin-polarization is not limited to the particular SrRuO$_3$/n-BaTiO$_3$ junction considered in this work. We expect the phenomenon to be a general feature of the FM/n-FE interface owing to the fact that the

effect stems from the electrostatic modulation of the barrier on the ferroelectric side of the interface and not on the properties of the ferromagnetic metal. In particular, this effect should be manifest for other ferromagnetic electrodes, e.g. those with higher Curie temperatures for operation at room temperature. Moreover, we anticipate the possibility of spin-polarization control over a broader range of values, including a change between positive and negative. This additional tunability can be achieved by changing the doping level on the ferroelectric, as well as using interface engineering to adjust the Schottky barrier at the interface [62,140] and/or enhance ferroelectric polarization stability [43]. The detection of spin polarization may be achieved using methods similar to those adopted in the studies of spin injection into semiconductors [107-112].

5.3.2   Ferroelectric polarization dependent sign of spin-polarization

In order to reveal the possibility to control the sign of the spin-polarization via ferroelectric polarization orientation we perform theoretical modeling based on a free electron approach, taking into account parameters extracted from the first-principles calculations. We assume a low doping limit, when the Fermi surface of n-BaTiO$_3$ has an ellipsoidal shape and the tunneling conductance is dominated by electrons at $k_\parallel = 0$.[*] We consider a Schottky barrier which has an exponential potential profile $V(z) = U e^{-\lambda z}$, as shown in inset in Figure 5.8. Details of the model are given in the Section 5.4. We find that the transport spin-polarization P_s is determined by the spin-dependent Fermi wave vectors in the ferromagnetic metal, $k_z^\uparrow$ and $k_z^\downarrow$, and the Schottky barrier height U so that

---

[*] Note that this limit is prohibitive to density-functional calculations due to a large screening length in n-BaTiO$_3$ which makes the required supercell too large.
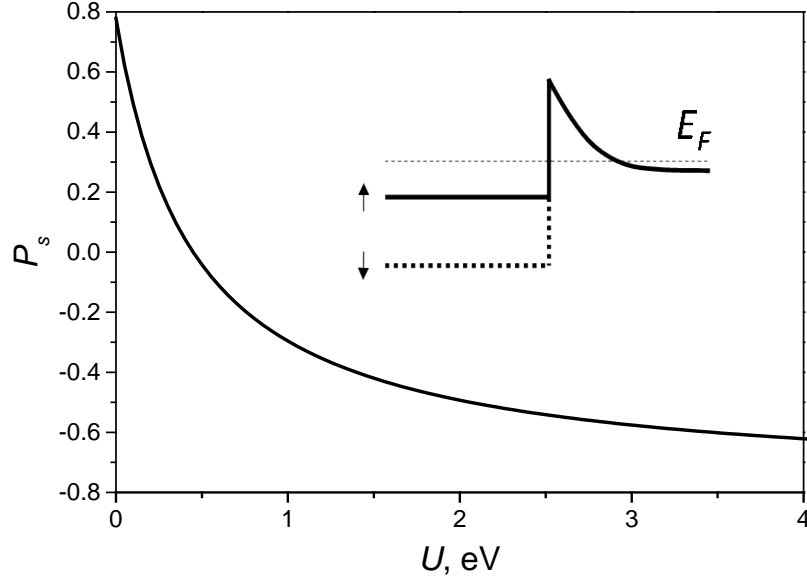
Figure 5.8 Spin polarization as a function of the Schottky barrier height U for

$k_z^{\uparrow} \approx 0.079$ Å, $k_z^{\downarrow} \approx 0.634$ Å and $\gamma = 5.55$. The inset shows schematically the potential

profiles for up- (solid line) and down- (dashed line) spin electrons.

$$P_s = \frac{k_z^{\uparrow} - k_z^{\downarrow}}{k_z^{\uparrow} + k_z^{\downarrow}} \frac{\kappa^2 - \gamma^2 k_z^{\uparrow} k_z^{\downarrow}}{\kappa^2 + \gamma^2 k_z^{\uparrow} k_z^{\downarrow}}, \tag{8}$$

where $\kappa^2 = 2m_z U / \hbar^2$, m_z is the effective mass in n-BaTiO$_3$ along the transport direction,

$\gamma = m_z / m$, and m is the free electron mass. Interestingly, formula (8) is similar to the

Slonczewski formula derived for a rectangular potential barrier [119]. It is evident that

the spin-polarization changes sign when $\kappa^2 = \gamma^2 k_z^{\uparrow} k_z^{\downarrow}$. Figure 5.8 shows the spin

polarization as a function of the Schottky barrier height U for the Fermi wave vectors of

SrRuO$_3$ and the effective mass in n-BaTiO$_3$ obtained from our first-principles calculation.

We see from the figure that the spin polarization changes sign at $U \approx 0.44$ eV. This value

lies between $U = 0.13$ eV and $U = 0.73$ eV predicted by our density-functional

calculation for two ferroelectric polarization orientations in the $SrRuO_3$/n-$BaTiO_3$ junction.[*] We therefore expect that at low electron doping the spin polarization of conductance in this junction should change its sign with reversal of ferroelectric polarization in n-$BaTiO_3$.

5.4   Free electron model
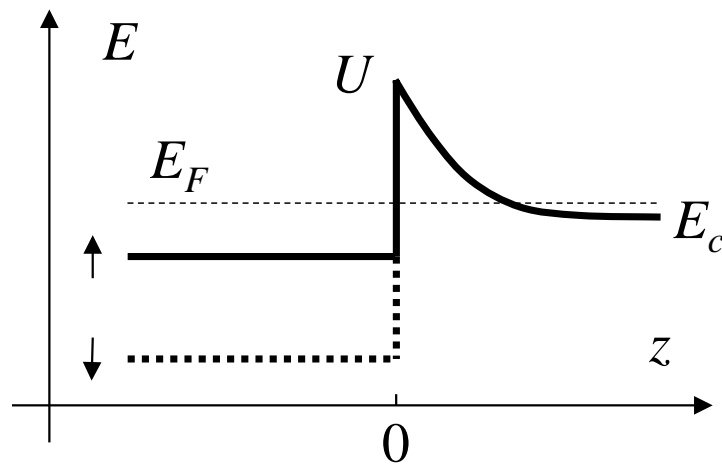
Figure 5.9 Schematic potential profiles for up- (solid line) and down- (dashed line) spin electrons across a FM/n-FE interface.

We employ a free-electron model to describe electron transmission from a semi-infinite ferromagnetic (FM) metal layer to a semi-infinite electron-doped ferroelectric (n-FE) which are separated by a Schottky barrier at the interface. The overall potential profile

---

[*] In the low doping limit these values may be different. For n = 0.06 e/u.c. the polarization is only ~10% lower than that of un-doped $BaTiO_3$ and therefore we expect that the larger ferroelectric polarization in the low doping limit will enhance the modulation of the Schottky barrier height about the average value and make the change of sign of the spin polarization more robust.

seen by transport electrons is a superposition of the step-wise potential originating from the offset of the conduction band minima in the FM and n-FE and the electrostatic potential resulting from the screening charge forming the Schottky barrier (Figure 5.9). The Schottky barrier height is dependent on ferroelectric polarization orientation. The FM metal is described by the spin-dependent potential (shown by solid and dashed lines in Figure 5.9) resulting in the spin-dependent Fermi wave vectors, $k_z^{\uparrow}$ and $k_z^{\downarrow}$, corresponding to up- and down-spin respectively.

The potential in the n-FE layer ($z > 0$) has the form of $E_c + U e^{-z/\lambda}$, where E_c is bottom of the conduction band, U is the Schottky barrier height, and λ is the screening length. This shape of the Schottky barrier is consistent with our first-principles calculations from which we find $\lambda \approx 11$ Å, and $U = 0.13$ eV and $U = 0.73$ eV for the two ferroelectric polarization orientations in the SrRuO$_3$/n-BaTiO$_3$ junction with $n = 0.06e$ per unit cell. The Schrödinger equation in the ferroelectric layer ($z > 0$) can be written as follows:

$$-\psi''(z) - q_f^2 \psi(z) + \kappa^2 e^{-z/\lambda} \psi(z) = 0,\qquad(9)$$

where $q_f^2 = \dfrac{2m_z}{\hbar^2}(E_F - E_c)$ is the wave vector in n-FE layer and $\kappa^2 = \dfrac{2m_z}{\hbar^2}U$. It has two linear independent solutions. The solution corresponding to the transmitted wave ψ_t which has at large z an asymptotic behavior representing an outgoing plane wave $e^{iq_f z}$ is given by:

$$\psi_t(z) = C e^{-\pi q_f \lambda} J_{-\nu}\left(2i\kappa\lambda e^{-z/2\lambda}\right),\qquad(10)$$

where $v = 2iq_f\lambda$, $J_\eta(\xi)$ is a Bessel function of the first kind, and C is a constant.

Solution of the Schrödinger equation in the ferromagnetic layer for each spin projection can be taken as a linear combination of the incident ψ_i and reflected ψ_r plane waves:

$$\psi = \psi_i + \psi_r = e^{ik_z z} + B e^{-ik_z z},$$
(11)

where for simplicity we omit the spin index for the Fermi wave vector k_z in the FM metal layer. The coefficients C for the transmitted wave and B for the reflected wave are found from the continuity conditions for the wave function and the current density at the interface ($z = 0$):

$$C = \frac{2\gamma k_z e^{\pi q_f \lambda}}{\left[\gamma k_z J_{-v}(2i\kappa\lambda) - \kappa J'_{-v}(2i\kappa\lambda)\right]},$$
(12)

where $\gamma = m_z / m$ and m is the free electron mass.

In order to obtain transmission we need to find the coefficient A of the outgoing plane wave $A e^{iq_f z}$ at large z. Taking the limit of $z \to +\infty$ in Eq. (10) we arrive at

$$\lim_{z \to +\infty} \psi_t(z) = \frac{Ce^{-\pi q_f \lambda}}{\Gamma(1-v)}\left(i\kappa\lambda e^{-z/2\lambda}\right)^{-v} == \frac{Ce^{-\pi q_f \lambda}}{\Gamma(1-v)}\left(i\kappa\lambda\right)^{-2iq_f\lambda} e^{iq_f z},$$
(13)

so that

$$A = \frac{1}{\Gamma(1-v)}\frac{2\gamma k_z}{\left[\gamma k_z J_{-v}(2i\kappa\lambda) - \kappa J'_{-v}(2i\kappa\lambda)\right]}\left(i\kappa\lambda\right)^{-2iq_f\lambda},$$
(14)

where $\Gamma(\xi)$ is the gamma function. The transmission coefficient is then given by

$$T = \frac{q_f}{\gamma k_z}|A|^2 = \frac{1}{|\Gamma(1-v)|^2}\frac{4\gamma k_z q_f e^{2\pi q_f \lambda}}{\left|\gamma k_z J_{-v}(2i\kappa\lambda) - \kappa J'_{-v}(2i\kappa\lambda)\right|^2}.$$
(15)

Expression (15) can be simplified in the limit of low doping, when q_f is small. In this limit λ and hence $\kappa\lambda$ become large, however, the product $q_f\lambda$ and hence ν remain small. In this limit, we can use an asymptotic expression for the Bessel function

$$J_\eta(\xi) \approx \frac{1}{2}\sqrt{\frac{2}{\pi\xi}} e^{-i\left(\xi - \frac{\eta\pi}{2} - \frac{\pi}{4}\right)} .$$

(16)

Substituting Eq. (16) into Eq. (15) we find for the transmission coefficient:

$$T \approx \frac{16\pi\gamma k_z q_f \kappa\lambda}{\left(\gamma^2 k_z^2 + \kappa^2\right)} e^{-4\kappa\lambda} .$$

(17)

Spin dependence in Eq. (17) enters through k_z which have different values for up- ($k_z^\uparrow$), and down- ($k_z^\downarrow$) spin electrons. The spin polarization is defined as follows:

$$P_s = \frac{T^\uparrow - T^\downarrow}{T^\uparrow + T^\downarrow} ,$$

(18)

where $T^\uparrow$ and $T^\downarrow$ are transmissions for up- and down-spin electrons respectively. From Eq. (18) we finally obtain Eq. (8) as is shown in Section 5.3.2,

$$P_s = \frac{k_z^\uparrow - k_z^\downarrow}{k_z^\uparrow + k_z^\downarrow} \frac{\kappa^2 - \gamma^2 k_z^\uparrow k_z^\downarrow}{\kappa^2 + \gamma^2 k_z^\uparrow k_z^\downarrow} .$$

5.5   Conclusions

In summary, we have shown that a ferromagnet/n-doped ferroelectric junction can be used to control the spin-polarization of injected carries. For the prototypical SrRuO$_3$/n-BaTiO$_3$ junction, we predicted that reversal of ferroelectric polarization of n-BaTiO$_3$ changes the spin-polarization of transmission from -65% to -98%. This sizable change occurs due to the effect of ferroelectric polarization on the effective contact barrier height,

selecting preferentially electrons with a certain spin orientation as a result of the spin-dependent Fermi surface of $SrRuO_3$. We also showed a possibility to change the sign of the spin-polarization in this system at low electron doping. The proposed ferroelectrically-tunable spin-polarization offers an exciting prospect to extend the functionalities of semiconductor-based spintronic devices.

Reference

[1] C. H. Ahn, K. M. Rabe, and J.-M. Triscone, Science 303, 488 (2004)

[2] R. Resta and D. Vanderbilt, in *Physics of Ferroelectrics: a Modern Perspective*, edited by K. M. Rabe, C. H. Ahn, and J.-M. Triscone (Springer-Verlag, Berlin, 2007), pp. 31–68.

[3] J. M. Rondinelli, S. J. May, and J. W. Freeland, MRS Bull. 37, 261 (2012).

[4] C. Ederer and N. A. Spaldin, Phys. Rev. B 71, 060401 (2005).

[5] A. Ohtomo and H. Y. Hwang, Nature London 427, 423 (2004).

[6] N. Reyren, S. Thiel, A. D. Caviglia, L. F. Kourkoutis, G. Hammerl, C. Richter, C. W. Schneider, T. Kopp, A. S. Ruetschi, D. Jaccard, M. Gabay, D. A. Muller, J. M. Triscone, and J. Mannhart, Science 317, 1196 (2007).

[7] N. Benedek and C. Fennie, J. Phys. Chem. C 117, 13339 (2013).

[8] V. M. Goldschmidt, Naturwiss.14, 477 (1926).

[9] J. H. Haeni, P. Irvin, W. Chang, R. Uecker, P. Reiche, Y. L. Li, S. Choudhury, W. Tian, M. E. Hawley, B. Craigo, A. K. Tagantsev, X. Q. Pan, S. K. Streiffer, L. Q. Chen, S. W. Kirchoefer, J. Levy and D. G. Schlom, Nature 430, 758 (2004)

[10] M. Dawber, K. M. Rabe, and J. F. Scott, Rev. Mod. Phys. 77, 1083 (2005).

[11] J. F. Scott, Science 315, 954 (2007).

[12] Y. M. Jin, Y. U. Wang, A. G. Khachaturyan, J. F. Li, and D. Viehland., Phys. Rev. Lett. 91, 197601 (2003).

[13] R. M. Martin, Phys. Rev. B 9, 1998 (1974).

[14] R. D. King-Smith and D. Vanderbilt, Phys. Rev. B 47, 1651 (1993).

[15] D. Vanderbilt and M. H. Cohen, Phys. Rev. B 63, 094108 (2001)

[16] M. Dawber, P. Chandra, P. B. Littlewood, and J. F. Scott, J. Phys.: Condens. Matter 15, L393 (2003).

[17] A. V. Bune, V. M. Fridkin, S. Ducharme, L. M. Blinov, S. P. Palto, A. V. Sorokin, S. G. Yudin, and A. Zlatkin, Nature 391, 874 (1998).

[18] J. Junquera and P. Ghosez, Nature 422, 506 (2003).

[19] D. D. Fong, G. B. Stephenson, S. K. Streiffer, J. A. Eastman, O. Auciello, P. H. Fuoss, and C. Thompson, Science 304, 1650 (2004).

[20] G. Gerra, A. K. Tagantsev, N. Setter, and K. Parlinski, Phys. Rev. Lett. 96, 107603 (2006).

[21] A. K. Tagantsev, G. Gerra, and N. Setter, Phys. Rev. B 77, 174111 (2008).

[22] H. N. Lee, H. M. Christen, M. F. Chisholm, C. M. Rouleau, and D. H. Lowndes, Nature 433, 395 (2005).

[23] S. M. Nakhmanson, K. M. Rabe, and D. Vanderbilt, Phys. Rev. B 73, 060101(2006).

[24] C. A. F. Vaz, J. Hoffman, C. H. Ahn, and R. Ramesh, Adv. Mater. 22, 2900 (2010).

[25] M. K. Niranjan, J. D. Burton, J. P. Velev, S. S. Jaswal, and E. Y. Tsymbal, Appl. Phys. Lett. 95, 052501 (2009).

[26] M. K. Niranjan, Y. Wang, S. S. Jaswal, and E. Y. Tsymbal, Phys. Rev. Lett. 103, 016804 (2009).

[27] Y. Wang, M. K. Niranjan, S. S. Jaswal, and E. Y. Tsymbal, Phys. Rev. B 80, 165130 (2009)

[28] P. W. M. Blom, R. M. Wolf, J. F. M. Cillessen, and M. P. C. M. Krijn, Phys. Rev. Lett. 73, 2107 (1994).

[29] E. Y. Tsymbal and H. Kohlstedt, Science 313, 181 (2006)

[30] E. Y. Tsymbal, A. Gruverman, V. Garcia, M. Bibes, and A. Barthélémy, MRS Bulletin 37, 138 – 143 (2012).

[31] J. Rodríguez Contreras, H. Kohlstedt, U. Poppe, R. Waser, C. Buchal, and N. A. Pertsev, Appl. Phys. Lett. 83, 4595 (2003).

[32] V. Garcia, S. Fusil , K. Bouzehouane, S. Enouz-Vedrenne, N.D. Mathur, A. Barthélémy, and M. Bibes, Nature 460 , 81 (2009).

[33] A. Gruverman, D. Wu, H. Lu, Y. Wang, H. W. Jang, C.M. Folkman, M. Ye. Zhuravlev, D. Felker, M. Rzchowski, C.-B. Eom and E. Y. Tsymbal, Nano Letters 9, 3539 (2009).

[34] M. Y. Zhuravlev, R. F. Sabirianov, S. S. Jaswal, and E. Y. Tsymbal, Phys. Rev. Lett. 94, 246802 (2005).

[35] Z. Wen, C. Li, D. Wu, A. Li, and N. Ming, Nat. Mater. 12, 617 (2013)

[36] M. Y. Zhuravlev, R. F. Sabirianov, S. S. Jaswal, and E. Y. Tsymbal, Appl. Phys. Lett. 87, 222114 (2005).

[37] J. P. Velev, C.-G. Duan, J. D. Burton, A. Smogunov, M. K. Niranjan, E. Tosatti, S. S. Jaswal, and E. Y. Tsymbal, Nano Lett. 9, 427 (2009).

[38] T. Kolodiazhnyi, M. Tachibana, H. Kawaji, J. Hwang, and E. Takayama-Muromachi, Phys. Rev. Lett. 104, 147602 (2010).

[39] T. Choi, S. Lee, Y. J. Choi, V. Kiyuknin, and S.-W. Cheong, Science 324, 63 (2009).

[40] W. Ji, K. Yao, and Y. C. Liang, Adv. Mater. 22, 1763 (2010).

[41] H. T. Yi, T. Choi, S. G. Choi, Y. S. Oh, and S.-W. Cheong, Adv. Mater. 23, 3403 (2011).

[42] X. Liu, Y. Wang, P. V. Lukashev, J. D. Burton, and E. Y. Tsymbal, Phys. Rev. B 85, 125407 (2012).

[43] H. Lu, X. Liu, J. D. Burton, C.-W. Bark, Y. Wang, Y. Zhang, D. J. Kim, A. Stamm, P. Lukashev, D. A. Felker, C. M. Folkman, P. Gao, M. S. Rzchowski, X. Q. Pan, C.-B. Eom, E. Y. Tsymbal, and A. Gruverman, Adv. Mater. 24, 1209 (2012).

[44] C. Lichtensteiger, J.-M. Triscone, J. Junquera, and P. Ghosez, Phys. Rev. Lett. 94, 047603 (2005).

[45] D. D. Fong, A. M. Kolpak, J. A. Eastman, S. K. Streiffer, P. H. Fuoss, G. B. Stephenson, C. Thompson, D. M. Kim, K. J. Choi, C. B. Eom, I. Grinberg, and A. M. Rappe, Phys. Rev. Lett. 96, 127601 (2006).

[46] S. K. Streiffer, J. A. Eastman, D. D. Fong, C. Thompson, A. Munkholm, M. V. Ramana Murty, O. Auciello, G. R. Bai, and G. B. Stephenson, Phys. Rev. Lett. 89, 067601 (2002).

[47] I. Kornev, H. Fu, and L. Bellaiche, Phys. Rev. Lett. 93, 196104 (2004).

[48] B.-K. Lai, I. Ponomareva, I. I. Naumov, I. Kornev, H. Fu, L. Bellaiche, and G. J. Salamo, Phys. Rev. Lett. 96, 137602 (2006).

[49] N. A. Pertsev and H. Kohlstedt, Phys. Rev. Lett. 98, 257603 (2007).

[50] P. Aguado-Puente and J. Junquera, Phys. Rev. Lett. 100, 177601 (2008).

[51] V. Nagarajan, J. Junquera, J. Q. He, C. L. Jia, R. Waser, K. Lee, Y. K. Kim, S. Baik, T. Zhao, R. Ramesh, Ph. Ghosez, and K. M. Rabe, J. Appl. Phys. 100, 051609 (2006).

[52] D. J. Kim, J. Y. Jo, Y. S. Kim, Y. J. Chang, J. S. Lee, J.-G. Yoon, T. K. Song, and T. W. Noh, Phys. Rev. Lett. 95, 237602 (2005).

[53] A. K. Tagantsev and G. Gerra, J. Appl. Phys. 100, 051607 (2006).

[54] Y. Umeno, J. M. Albina, B. Meyer, and C. Elsässer, Phys. Rev. B 80, 205122 (2009).

[55] Y. Liu, X. Lou, M.Bibes, and B. Dkhil, Phys. Rev. B 88, 024106 (2013).

[56] C.-G. Duan, R. F. Sabirianov, W.-N. Mei, S. S. Jaswal, and E. Y. Tsymbal, Nano Lett. 6, 483 (2006).

[57] M. Stengel, D. Vanderbilt, and N. A. Spaldin, Nat. Mater. 8, 392 (2009).

[58] G. Kresse and J. Furthmüller, Comp. Mater. Sci. 6, 15 (1996).

[59] S. J. May, J. W. Kim, J. M. Rondinelli, E. Karapetrova, N. A. Spaldin, A. Bhattacharya, and P. J. Ryan, Phys. Rev. B 82, 014110 (2010).

[60] G. Gerra, A. K. Tagantsev, and N. Setter, Phys. Rev. Lett. 98, 207601 (2007).

[61] J. M. Rondinelli, M. Stengel, and N. A. Spaldin, Nature Nano. 3, 46 (2008).

[62] J. D. Burton and E. Y. Tsymbal, Phys. Rev. B 82, 161407 (2010).

[63] H. J. Chang, S. V. Kalinin, A. N. Morozovska, M. Huijben, Y.-H. Chu, P. Yu, R. Ramesh, E. A. Eliseev, G. S. Svechnikov, S. J. Pennycook, and A. Y. Borisevich, Advanced Materials 23, 2474 (2011).

[64] C.-Q. Jin, J.-S. Zhou, J. B. Goodenough, Q. Q. Liu, J. G. Zhao, L. X. Yang, Y. Yu, R. C. Yu, T. Katsura, A. Shatskiy, and E. Ito, Proc. Natl. Acad. Sci. 105, 7115 (2008).

[65] Y. Wang, M. K. Niranjan, K. Janicka, J. P. Velev, M. Ye. Zhuravlev, S. S. Jaswal, and E. Y. Tsymbal, Phys. Rev. B 82, 094114 (2010).

[66] R. M. Pick, M. H. Cohen, and R. M. Martin, Phys. Rev. B 1, 910 (1970).

[67] R. Kretschmer and K. Binder, Phys. Rev. B 20, 1065 (1979).

[68] M. D. Glinchuk and A. N. Morozovska, J. Phys. Condens. Matter 16, 3517 (2004).

[69] A. M. Bratkovsky and A. P. Levanyuk, Phys. Rev. Lett. 94, 107601 (2005).

[70] N. A. Pertsev, A. G. Zembilgotov, and A. K. Tagantsev, Phys. Rev. Lett. 80, 1988 (1998).

[71] K. J. Choi, M. Biegalski, Y. L. Li, A. Sharan, J. Schubert, R. Uecker, P. Reiche, Y. B. Chen, X. Q. Pan, V. Gopalan, L. Q. Chen, D. G. Schlom, and C. B. Eom, Science 306, 1005 (2004).

[72] C. B. Eom, R. J. Cava, R. M. Fleming, J. M. Phillips, R. B. van Dover, J. H. Marshall, J. W. P. Hsu, J. J. Krajewski, W. F. Peck Jr., Science 258, 1766 (1992).

[73] W. Zhong, R. D. King-Smith, and D. Vanderbilt, Phys. Rev. Lett. 72, 3618 (1994).

[74] R. E. Cohen, Nature 358, 136 (1992).

[75] N. A. Hill, J. Phys. Chem. B 104, 6694 (2000).

[76] P. Ghosez, J.-P. Michenaud, and X. Gonze, Phys. Rev. B 58, 6224 (1998).

[77] J. F. Scott, Rev. Mod. Phys. 46, 83 (1974).

[78] V. Fridkin, *Ferroelectric Semiconductors* (Consultants Bureau, New York, 1980), p. 318.

[79] J. Hwang, T. Kolodiazhnyi, J. Yang, and M. Couillard, Phys. Rev. B 82, 214109 (2010).

[80] I. K. Jeong, S. Lee, Se-Young Jeong, C. J. Won, N. Hur, and A. Llobet, Phys. Rev. B 84, 064125 (2011).

[81] P. W. Anderson and E. I. Blount, Phys. Rev. Lett. 14, 217 (1965).

[82] I. A. Sergienko, V. Keppens, M. McGuire, R. Jin, J. He, S. H. Curnoe, B. C. Sales, P. Blaha, D. J. Singh, K. Schwarz, and D. Mandrus, Phys. Rev. Lett. 92, 065501 (2004).

[83] M. Tachibana, N. Taira, H. Kawaji, and E. Takayama-Muromachi, Phys. Rev B 82, 054108 (2010).

[84] Y. Ishibashi and M. Iwata, J. Phys. Soc. Jpn. 79, 044604 (2010).

[85] Y. Shi, Y. Guo, X. Wang, A. J. Princep, D. Khalyavin, P. Manuel, Y. Michiue, A. Sato, K. Tsuda, S. Yu, M. Arai, Y. Shirako, M. Akaogi, N. Wang, K. Yamaura and A. T. Boothroyd, Nature Mater. 12, 1024 (2013).

[86] V. Keppens, Nature Mater. 12, 952 (2013).

[87] H. J. Xiang, Phys. Rev. B 90, 094108 (2014).

[88] H. Sim, and B. G. Kim, Phys. Rev. B 89, 201107(R) (2014).

[89] G. Giovannetti and M. Capone, arxiv 1404.7705 (2014).

[90] H. M. Liu, Y. P. Du, Y. L. Xie, J. -M. Liu, C.-G. Duan, X. Wan, arXiv 1409.4953 (2014)

[91] P. Giannozzi et al., J. Phys.: Cond. Matter 21, 395502 (2009).

[92] G. Rupprecht and B.O. Bell, Phys. Rev. A 135, 748 (1964).

[93] D. Ricinschi and M. Okuyama, Ferroelectrics 355, 101 (2007).

[94] C. L. Freeman, J. A. Dawson, H.-R. Chen, J. H. Harding, L.-B. Ben, and D. C. Sinclair, J. Mater. Chem. 21, 4861 (2011).

[95] A. Gruverman, D. Wu, H. Lu, Y. Wang, H. W. Jang, C.M. Folkman, M. Ye. Zhuravlev, D. Felker, M. Rzchowski, C.-B. Eom and E. Y. Tsymbal, Nano Letters 9, 3539 (2009).

[96] A. Q. Jiang, C. Wang, K. J. Jin, X. B. Liu, J. F. Scott, C. S. Hwang, T. A. Tang, H. B. Lu, and G. Z. Yang, Adv. Mater. 23, 1277 (2011).

[97] H. Lu, C.-W. Bark, D. Esque de los Ojos, J. Alcala, C. B. Eom, G. Catalan, and A. Gruverman, Science 336, 59 (2012).

[98] J. P. Velev, S. S. Jaswal, and E.Y. Tsymbal, Phil. Trans. R.Soc. A 369, 3069 (2011).

[99] J. D. Burton and E. Y. Tsymbal, Phys. Rev. Lett. 106, 157203(2011).

[100] Y. W. Yin, J. D. Burton, Y.-M. Kim, A. Y. Borisevich, S. J. Pennycook, S. M. Yang, T. W. Noh, A. Gruverman, X. G. Li, E. Y. Tsymbal, and Q. Li, Nat. Mater. 12, 397 (2013).

[101] L. Jiang, W. Jiang, H. Choi, S. Jeen, Y. Dong, M.-G. Kim, Y. Han, S. Zhu, E. Kalinin, T. Dagotto, H. Egami, and Lee, Nano Lett. 13, 5837 (2013).

[102] D. Lee, S. H. Baek, T. H. Kim, J.-G. Yoon, C. M. Folkman, C. B. Eom, and T. W. Noh, Phys. Rev. B 84, 125305 (2011).

[103] F. Chen and A. Klein, Phys. Rev. B 86, 094105 (2012).

[104] L. Nordheim, Ann. Phys. 401, 607 (1931).

[105] K. M. Schep, J. B. A. N. van Hoof, P. J. Kelly, G. E. W. Bauer, and J. E. Inglesfield, Phys. Rev. B 56, 10805 (1997).

[106] E. Y. Tsymbal and I. Žutić, Eds., *Handbook of Spin Transport and Magnetism* (CRC press, Boca Raton, FL, 2011), 808 pp.

[107] Y. Ohno, D. K. Young, B. Beschoten, F. Matsukura, H. Ohno, and D. D. Awschalom, Nature 402, 790 (1999).

[108] X. Jiang, R. Wang, R. M. Shelby, R. M. Macfarlane, S. R. Bank, J. S. Harris, and S. S. P. Parkin, Phys. Rev. Lett. 94, 056601 (2005).

[109] I. Zutic, J. Fabian, and S. C. Erwin, Phys. Rev. Lett. 97, 026602 (2006).

[110] I. Appelbaum, B. Huang, and D. J. Monsma, Nature 447, 295 (2007).

[111] B. T. Jonker, G. Kioseoglou, A. T. Hanbicki, C. H. Li, and P. E. Thompson, Nat. Phys. 3, 542 (2007).

[112] S. P. Dash, S. Sharma, R. S. Patel, M. P. de Jong, and R. Jansen, Nature 462, 491 (2009).

[113] W. Han, X. Jiang, A. Kajdos, S.-H. Yang, S. Stemmer, and S. S. P. Parkin, Nat. Comm. 4, 2134 (2013).

[114] T. Wakamura, N. Hasegawa, K. Ohnishi, Y. Niimi, and Y. Otani, Phys. Rev. Lett. 112, 036602 (2014).

[115] R. Meservey, P. M. Tedrow, and P. Fulde, Phys. Rev. Lett. 25, 1270 (1970).

[116] P. M. Tedrow and R. Meservey, Phys. Rev. Lett. 26, 192 (1971).

[117] E. Y. Tsymbal, O. N. Mryasov, and P. R. LeClair, J. Phys. Condens. Matter 15, R109 (2003).

[118] M. B. Stearns, J. Magn. Magn. Mater. 5, 1062 (1977).

[119] J. C. Slonczewski, Phys. Rev. B 39, 6995 (1989).

[120] I. Zutic, J. Fabian, and S. Das Sarma, Rev. Mod. Phys. 76, 323 (2004).

[121] P. C. van Son, H. van Kempen, and P. Wyder, Phys. Rev. Lett. 58, 2271 (1987).

[122] G. Schmidt, D. Ferrand, L. W. Molenkamp, A. T. Filip, and B. J. Van Wees, Phys. Rev. B 62, R4790 (2000).

[123] R. H. Silsbee, Bull. Magn. Reson. 2, 284 (1980).

[124] M. Johnson, and R. H. Silsbee, Phys. Rev. Lett. 55, 1790 (1985).

[125] M. Johnson, and R. H. Silsbee, Phys. Rev. B 37, 5326 (1988).

[126] E. Rashba, Phys. Rev. B 62, R16267 (2000).

[127] E. I. Rashba, Appl. Phys. Lett. 80, 2329 (2002).

[128] H.J. Zhu, M. Ramsteiner, H. Kostial, M. Wassermeier, H.-P. Schonherr, and K.H. Ploog, Phys. Rev. Lett. 87, 016601 (2001).

[129] J. Mannhart and D. G. Schlom, Science 327, 1607 (2010).

[130] E. Y. Tsymbal, A. Gruverman, V. Garcia, M. Bibes, and A. Barthélémy, MRS Bull. 37, 138 (2012).

[131] M. Y. Zhuravlev, S. S. Jaswal, E. Y. Tsymbal, and R. F. Sabirianov, Appl. Phys. Lett. 87, 222114 (2005).

[132] M. Y. Zhuravlev, S. Maekawa, and E. Y. Tsymbal, Phis. Rev. B 81, 104419 (2010).

[133] V. Garcia, M. Bibes, L. Bocher, S. Valencia, F. Kronast, A. Crassous, X. Moya, S. Enouz-Vedrenne, A. Gloter, D. Imhoff, C. Deranlot, N. D. Mathur, S. Fusil, K. Bouzehouane, and A. Barthelemy, Science 327, 1106 (2010).

[134] M. Hambe, A. Petraru, N. A. Pertsev, P. Munroe, V. Nagarajan, and H. Kohlstedt, Adv. Func. Mater. 20, 2436 (2010).

[135] D. Pantel, S. Goetze, D. Hesse, and M. Alexe, Nat. Mater. 11, 289 (2012).

[136] Y. W. Yin, J. D. Burton, Y.-M. Kim, A. Y. Borisevich, S. J. Pennycook, S. M. Yang, T. W. Noh, A. Gruverman, X. G. Li, E. Y. Tsymbal, and Q. Li, Nat. Mater. 12, 397 (2013).

[137] Y. Wang, X. Liu, J. D. Burton, S. S. Jaswal, and E. Y. Tsymbal, Phys. Rev. Lett. 109, 247601 (2012).

[138] Y. Iwazaki, T. Suzuki, Y. Mizuno, and S. Tsuneyuki, Phys. Rev. B 86, 214103 (2012).

[139] G. Koster, L. Klein, W. Siemons, G. Rijnders, J. S. Dodge, C.-B. Eom, D. H. A. Blank, and M. R. Beasley, Rev. Mod. Phys. 84, 253 (2012).

[140] Y. Hikita, M. Nishikawa, T. Yajima, and H. Y. Hwang, Phys. Rev. B 79, 073101 (2009).

Publications

1. "Electric control of spin injection into a ferroelectric semiconductor"

   X. Liu, J. D. Burton, M. Ye. Zhuravlev and E. Y. Tsymbal, submitted to Phys. Rev. Lett. (2014).

2. "Polarization-controlled Ohmic to Schottky transition at a metal/ferroelectric interface"

   X. Liu, Y. Wang, J. D. Burton, and E. Y. Tsymbal, Phys. Rev. B 88, 165139 (2013).

3. "Ferroelectric Instability Under Screened Coulomb Interactions"

   Y. Wang, **X. Liu**, J. D. Burton, S. S. Jaswal, and E. Y. Tsymbal, Phys. Rev. Lett. 109, 247601 (2012).

4. "Enhancement of ferroelectric polarization stability by interface engineering"

   H. Lu, **X. Liu**, C.-W. Bark, J. D. Burton, Y. Wang, Y. Zhang, D. J. Kim, A. Stamm, P. Lukashev, D. A. Felker, C. M. Folkman, P. Gao, X. Q. Pan, M. S. Rzchowski, C.-B. Eom, E. Y. Tsymbal, and A. Gruverman, Adv. Mater. 24, 1209 (2012).

5. "Interface dipole effect on thin film ferroelectric stability: First-principlesand phenomenological modeling"

   X. Liu, Y. Wang, P. V. Lukashev, J. D. Burton, and E. Y. Tsymbal, Phys. Rev. B 85, 125407 (2012).

Presentations

1. **"Ferroelectric control of spin injection across the ferromagnet/ferroelectric interface"**

   American Physical Society (APS) March Meeting, Denver, Colorado, March 2014.

2. **"Polarization control of the Schottky barrier at a metal/n-type-ferroelectric interface"** MRS Fall Meeting, Boston, Massachusetts, December 2013.

3. **"Polarization controlled Ohmic to Schottky transition at a metallic oxide-doped ferroelectric interface"**

   American Physical Society (APS) March Meeting, Baltimore, Maryland, March 2013.

4. **"Polarization controlled Ohmic to Schottky transition at a metallic oxide-doped ferroelectric interface"**

   Fundamental Physics of Ferroelectrics and Related Materials workshop, Ames, Iowa, January 2013.

5. **"Exploring and alleviating detrimental interface dipole effects in ultra-thin all-oxide metal-ferroelectric-metal heterostructures"**

   American Physical Society (APS) March Meeting, Boston, *Massachusetts*, March 2012.

6. **"Stabilizing ferroelectric polarization of ultrathin $BaTiO_3$ films through interface engineering"**

   American Physical Society (APS) March Meeting, Dallas, Texas, March 2011

7. **"Stabilizing ferroelectric polarization of ultrathin $BaTiO_3$ films through interface engineering"**

Graduate Student Poster Session, Nebraska Research Fair, Lincoln, Nebraska, April, 2011;

Nebraska Research & Innovation Conference, Nebraska, Omaha, 27 September, 2011;

Pan-American Advanced Study Institute (PASI) Workshop, Santiago, Chile, January, 2012.